1966

A study of the surface reactions of hydrocarbons on tungsten by field electron emission microscopy

Nelson Craig Gardner
Iowa State University

A STUDY OF THE SURFACE REACTIONS OF HYDROCARBONS ON TUNGSTEN BY FIELD ELECTRON EMISSION MICROSCOPY

by

Nelson Craig Gardner

A Dissertation Submitted to the

Graduate Faculty in Partial Fulfillment of

The Requirements for the Degree of

DOCTOR OF PHILOSOPHY

Major Subject: Physical Chemistry

Approved:

Signature was redacted for privacy.

In Charge of Major Work

Signature was redacted for privacy.

Head of Major Department

Signature was redacted for privacy.

Dean of Graduate College

Iowa State University
Of Science and Technology
Ames, Iowa

1966

TABLE OF CONTENTS

INTRODUCTION

It has become increasingly clear in the last few years that heterogeneous catalysis studies have been hampered by poorly characterized surfaces and by an incomplete understanding of the nature of the adsorbed species. In an attempt to rectify this situation, a number of new experimental techniques have been developed permitting the study of surface reactions under highly idealized conditions. These include contact potential difference measurements, flash filament desorption spectroscopy, low energy electron diffraction, and field electron and ion emission microscopy. All of these techniques, except for flash filament spectroscopy, differ from those previously employed in that, during the course of a reaction, the behavior of the adsorbed layer is studied directly rather than inferred from the appearance of species in the gas phase.

Although it may not be possible to study surface reactions under conditions that prevail during catalytic processes, it is important at this time to develop an understanding of reactions of simple reactants on well defined surfaces. The techniques listed above are sufficiently new that, with very few exceptions, they have not been applied to any of the classical problems in surface chemistry such as the ammonia synthesis, the catalytic hydrogenation of unsaturated hydrocarbons,

the Fischer-Tropsch synthesis, or catalytic oxidation reactions.

"No problems in surface chemistry have been more hotly debated than the adsorption and hydrogenation mechanisms for ethylene; and few debates have resulted in such meager conclusions." This view was held by Selwood in 1962 (1) and restated in the last major review of the subject by Bond and Wells in 1964 (2). It is hoped that the use of modern techniques will bring a measure of order to the field.

A recent field electron emission study in this laboratory (3) of the decomposition of acetylene and ethylene on a face-centered cubic metal, iridium, has provided new insights into the decomposition reactions of simple hydrocarbons. It has long been recognized that, in general, face-centered cubic metals are orders of magnitude more active in hydrocarbon decomposition and hydrogenation reactions than body-centered cubic metals. As a result, the bulk of research activity in this area has been concerned with the former type of metals. However, it is of considerable interest to determine how the surface reactions on the two types of metals differ, and, if possible, to clarify which properties of metals are important in catalytic activity. This investigation has been undertaken to establish the nature of the chemisorbed species and surface reactions of acetylene and ethylene on tungsten.

LITERATURE REVIEW

The field electron emission microscope has seen its greatest use in studies of the chemisorption of alkali metals and diatomic gases. The technique has only rarely been applied to more complicated systems.

Arthur and Hansen studied the decomposition of simple hydrocarbons on iridium (4) (5). They reported that ethane was only weakly chemisorbed with desorption occurring near 100°K. Ethylene chemisorbed on iridium with dissociation above 100°K. The desorption of hydrogen from the ethylene covered surface occurred in two equal steps. The rate of the first was determined by the rate of hydrogen desorption from the metal, the rate of the second being determined by the rate of dissociation of the acetylenic residue that remained. Acetylene was strongly chemisorbed and appeared similar in its dissociation to the acetylenic residue left from the dissociation of ethylene.

Azuma recorded photographs of the field emission patterns resulting from the reactions of ethylene with tungsten (6). From these he concluded that the decomposition of ethylene took place at temperatures in the order of 1950°K and above.

The chemisorption of ethylene on evaporated tungsten films has been studied volumetrically by Beeck (7) and Trapnell (8). From the volume ratio of adsorbed hydrogen to adsorbed ethylene of 2:1, it was

concluded that ethylene adsorption required four sites. Since the decomposition of ethylene was observed, ethylene adsorption was represented as requiring two sites for an adsorbed acetylenic species and two sites for the two hydrogen atoms resulting from the decomposition. In addition, self-hydrogenation was observed. The general features of the reaction are illustrated in Figure 1. The initial addition of ethylene to the film resulted in adsorption of ethylene until 82% of the surface was covered. As more ethylene was added, point A, ethane appeared in the gas phase. The total over-all reaction was represented by

$$2W + 2C_2H_4 \rightarrow W_2C_2H_2 + C_2H_6 \qquad (1)$$

At point B, the production of ethane was complete and ethylene appeared in the gas phase. The number of ethane molecules produced equaled the number of ethylene molecules adsorbed. The ethylene adsorption reached a limit at point C.

The interpretation of these findings was as follows: The ethylene initially chemisorbed dissociatively, freeing hydrogen which remained adsorbed. This process was formulated as

$$4* + C_2H_4(g) \rightarrow \underset{*}{C_2H_2}\underset{*}{} + \underset{*}{2H} \qquad (2)$$

Beyond point A, the self-hydrogenation reaction occurred, the formulation which was presented as

$$C_2H_4(g) + \underset{*}{2H} \rightarrow C_2H_6(g) + 2* \qquad (3)$$

of, if the complex reacted

$$\underset{*}{C_2H_2}\underset{*}{} + \underset{*}{4H} \rightarrow C_2H_6(g) + 6* \qquad (4)$$

The self-hydrogenation reaction continued until the surface was covered with acetylenic residues.

Acetylene was not observed to undergo self-hydrogenation reactions on tungsten, nor could adsorbed acetylene be hydrogenated with gaseous hydrogen (7).

The work on tungsten evaporated films is subject to a number of criticisms. The films were deposited in vacuum conditions no better than 10^{-6} torr. At this pressure, the rate of arrival of gas molecules of unknown composition to the surface is sufficient to cover the surface with a monolayer per second if the sticking probablity is one. In addition, the number of sites not occupied by ethylene was determined by admitting hydrogen gas to the film and assuming the amount of hydrogen adsorbed was proportional to the number of unoccupied sites. Hydrogen is notable for its variability of extent of adsorption on evaporated films. In addition, no account was taken of the self-hydrogenation reaction which could create more sites for ethylene adsorption; therefore, conclusions as to the extent of ethylene adsorption based on the hydrogen:ethylene ratio are subject to some doubt.

Nothing is known about the dependence of hydrocarbon chemisorption on various crystallographic planes. Beeck has found that 110 oriented nickel films are 5 to 7 times more active than non-oriented films for

ethylene self-hydrogenation; however, the reason for this enhanced activity is not understood (9).

It has been assumed that chemisorbed ethylene and acetylene are immobile since the heat of adsorption of the two gases is high (in the order of 100 kcal/mole (7)). However, the ratio of energy of diffusion to energy of desorption varies from 0.1 to 0.7 depending on the gas. It would not be surprising if ethylene and acetylene were found to be mobile at room temperature, but so far, no investigations of mobility have been reported.

One has to conclude that there remains much to be learned about the chemisorption and surface reactions of acetylene and ethylene, and in particular about the state of the adsorbed species.

FIELD ELECTRON EMISSION MICROSCOPY

In field emission microscopy, a cathode consisting of a very sharp metal tip (radius of the curvature commonly 1000-3000Å) is caused to emit electrons by applying a high voltage between the tip and the anode. The emission current depends on the applied voltage, but it also depends on the work function of the emitter, which in turn is sensitive to the number and type of molecules adsorbed on the emitter surface. It is therefore possible to monitor the course of surface reactions by measurement of the changes in work function accompanying them.

The field emission tubes used for modern studies are, in principle, descendents of a microscope developed in 1937 by E. W. Müller (10). Figure 2 shows the basic features of a microscope tube. A portion of the inside of the tube is coated with a phosphor so that it becomes functionally a small television screen. The electrons striking the screen cause it to phosphoresce producing an image of the tip which reflects the variation of work function over the tip surface. The tip is sufficiently small that its normal preparation leads to a single crystal emitter.

Since the electrons emerging from the tip (assumed spherical over the emitting portion) follow the lines of force radially from the tip to the screen, it is readily seen, Figure 3, that the image is magnified by the

ratio R/r where R is the tip to screen distance and r the tip radius. With tip to screen distances of 2-5 cm and tip radii of 1000Å (10^{-5} cm), the magnifications are in order of 10^5 to 10^6. The resolution is in the order of 20Å.

Figure 4 shows the pattern of clean tungsten photographed in the field electron emission microscope. This picture corresponds to the orthographic projection of a hemispherical cubic crystal with [110] in the axis, Figure 5. The bright areas correspond to regions of low work function and consist of high index planes. Conversely, the dark areas locate the planes of high work function which consist of closely packed low index planes.

Theory of Field Electron Emission

The potential energy diagram for electrons in a potential well representing the metal is shown in Figure 6. The potential inside the metal is assumed to be everywhere constant such that the electrons can be described by the particle in a box model. They are accommodated in pairs, as a consequence of the Pauli exclusion principle, in the energy levels that result from confinement in a finite volume until the supply of electrons is exhausted. The energy of the highest occupied level at $0^{\circ}K$ is the Fermi energy μ, and the energy difference between the Fermi level and the top of the barrier is the work function Φ of the metal.

An external field F(volts/cm) superposes an additional potential

$-eFx$; the total potential energy curve including the field contribution is also shown in Figure 6. There is in addition an image potential $-\frac{e^2}{4x}$ resulting from the electrostatic attraction of the electron and its image in the metal; this is omitted for simplicity in Figure 6 and in the direct presentation of the theory which follows although modifications to account for it will be mentioned.

Electron emission occurs when electrons leave the potential well. Classically, this is only possible if energy is provided sufficient to promote the electrons over the top of the barrier. The density of energy levels in the metal is such that most of the electrons have an energy near the Fermi energy, so an energy Φ must be supplied to promote them over the barrier. This energy is conveniently supplied thermally, the resulting phenomenon is called thermionic emission, and the emission current is approximately proportional to $\exp \frac{-e\Phi}{RT}$

Because of the wave properties of electrons, it is possible for electrons, in the presence of an applied field, to escape the potential well without surmounting the barrier. Electrons incident on the barrier are not totally reflected; some are refracted, attenuated, and, if the barrier is of finite thickness, pass through the barrier. In field emission the barrier is reduced to finite thickness, and its thickness is controlled by the applied field (as is evident from Figure 6, the stronger the field, the thinner the barrier). Since the distribution of electrons over the

energy levels of the metal is only weakly temperature-dependent, the field emission current density is also only weakly temperature-dependent, but it is strongly field-dependent. For any energy, the rate of impact of electrons on the barrier can be calculated by kinetic theory and the transmission probability can be calculated by quantum mechanics. The product is the contribution to the current density due to electrons of that energy. When this is integrated over the electron energy distribution the total current density is obtained. The result is the Fowler-Nordheim (F-N) equation which can be considered the basic equation of field emission.

$$J = 6.2 \times 10^{6} \frac{(\mu/\bar{\Phi})^{1/2}}{(\mu+\bar{\Phi})} F^{2} \exp(-6.80 \times 10^{7}\ \bar{\Phi}^{3/2}/F) \qquad (5)$$

The current density is given by J in amps/cm^2 if F is the field in volts/cm. This equation is generally adequate for interpretations needed for studies in catalysis. For a quantitative evaluation of absolute work function, the Fowler-Nordheim equation must be modified to account for the image potential. The resultant equation is

$$J = 1.54 \times 10^{-6} \frac{F^{2}}{\bar{\Phi}} \exp(-6.80 \times 10^{7}\ \bar{\Phi}^{3/2}\ v(y)/F) \qquad (6)$$

The function v(y) is an elliptical integral of the variable $y = 3.79 \times 10^{-4} \frac{F}{\bar{\Phi}}$ and for most common experimental conditions is in the range $0.8 < v(y) < 1.0$.

The field is related to the applied voltage by $F = \frac{V}{kr}$ $(k \sim 5)$ and the current density to the current by $I = JA$ where I is the current in amperes and A is the emitting area. The abbreviated form of the F-N equation is then

$$I = a\ V^{2} \exp(-b\ \bar{\Phi}^{3/2}\ v(y)/V) \qquad (7)$$

A review article by Good and Müller (11) contains a thorough account of the derivation of the F-N equation. Dyke and Dolan (12) reviewed the quantitative investigations of field emission phenomena. An extensive discussion of the theory and practice of field emission microscopy is presented in a book by Gomer (13) which is the most complete single source of information on the subject.

Work Function Change by Chemisorption

The adsorption of gas on metal surface modifies the potential barrier at the surface. While the details of the modification are not well understood, experimental evidence has suggested a classical model which has wide applicability.

For example, Gomer and Schmidt (14) have measured the work function change upon adsorption of potassium on tungsten by field emission techniques. The result is presented in Figure 7.

The salient feature of the curve is its linearity for surface coverages up to nearly a monolayer. Since the potential difference between two parallel plates of uniform charge density is proportional to the product of the charge density and the distance between the plates, the surface potential can be understood as arising from the formation of a dipole layer which results in a charge density of $N_s \theta q$, where N_s is the total number of sites per unit area, θ the fraction of filled sites, and q is the charge. If d is the distance from center of the adatom to the surface,

the surface potential would then be

$$\Delta\Phi = 4\pi N_s \theta qd = 4\pi N_s \theta M = 3.76 \times 10^{-15} N_s \theta M \qquad (8)$$

where M is the dipole moment in debyes per adatom and is assumed to be independent of coverage. The adsorption of .01 monolayers of an adsorbate (with a dipole moment of only 0.5 debyes) results in a 0.02 ev change at the surface. This can be resolved by field emission techniques.

Determination of Work Function

Since term b of equation 7 is insensitive to the applied voltage the work function can be evaluated from the slope of the F-N plot of $\ln I/V^2$ vs $1/V$. The slope is

$$\frac{d(\ln I/V^2)}{d(1/V)} = -b\Phi^{3/2}s(y) = S \qquad (9)$$

where s(y) varies only slowly with voltage (11); therefore, it is assumed to be constant for work function determinations. Let S_o and S_{ad} be the slopes obtained for clean and partially dosed surfaces. Following adsorption, Φ_{ad} can be calculated from

$$\Phi_{ad} = \left(\frac{S_{ad}}{S_o}\right)^{2/3} \left(\frac{b_o}{b_{ad}}\right)^{2/3} \Phi_o \qquad (10)$$

For most chemisorption studies, the ratio (b_o/b_{ad}) may be assumed unity.

A tempting alternate method of determining the work function change is to relate the work function to the voltage required to give a constant emission current. Equating the right sides of equation 7, it is easily

shown that

$$V_{ad}/V_o = \left(\frac{\bar{\varphi}_{ad}}{\bar{\varphi}_o}\right)^{3/2} + \frac{V_{ad}}{b\bar{\varphi}_o^{3/2}} \ln \frac{a_o V_o^2}{a_{ad} V_{ad}^2} \qquad (11)$$

For many systems of interest, the second term on the right (equation 11) is small compared to the first, so that to a good approximation

$$\bar{\varphi}_{ad} = \left(\frac{V_{ad}}{V_o}\right)^{2/3} \bar{\varphi}_o \qquad (12)$$

Furthermore, if $\Delta\bar{\varphi}/\bar{\varphi}_o$ is much less than one equation 12 can be expanded to give

$$\Delta\bar{\varphi} = \frac{2}{3}\left(\frac{\Delta V}{V_o}\right)\bar{\varphi}_o \qquad (13)$$

Both equations should be verified experimentally for each system studied before they are used to determine work function changes.

In the case of an actual field emitter tip, where the surface consists of regions of different work function, the measured current I is the sum of the individual patch currents such that

$$\frac{I}{V^2} = \sum_k \frac{i_k}{V^2} = \sum_k a_k \exp\left(-b_k \bar{\varphi}_k^{3/2}/V\right) \qquad (14)$$

Defining an average work function $\bar{\varphi}$ as

$$\frac{I}{V^2} = \bar{a} \exp\left(-\bar{b}\,\bar{\varphi}^{3/2}/V\right) \qquad (15)$$

it can easily be shown that

$$\bar{\varphi}^{3/2} = \sum_k \frac{i_k}{I} \frac{b_k}{\bar{b}} \bar{\varphi}_k^{3/2} \qquad (16)$$

The quantity i_k/I is functionally a weighting factor in averaging the work functions of the different crystal faces. Since the low work function

faces emit most strongly they are most strongly reflected in the average, which therefore tends to approximate the lowest work function represented. For example, if only two faces of equal area and work functions 4.5 and 5.0 contribute to the current the average work function obtained from the F-N plot will be 4.53 volts. It is apparent that caution must be exercised in the interpretation of average work function changes as related to surface events in that, for many systems of catalytic interest, the emission anisotropy changes as the reaction occurs.

Effect of Barrier Shape

Since field emission is a quantum mechanical phenomenon, involving the tunneling of electrons through a potential barrier, the work function, as measured by field emission techniques, depends on barrier shape as well as height. Thus, field emission measurements of work function may differ in a significant way from measurements obtained by contact potential or thermionic methods which do not depend similarly on barrier shape.

For a qualitative evaluation of the effect of barrier shape, it is instructive to consider a simple rationale of the exponential of the Fowler-Nordheim equation (13). The probability of transmission, D, of an electron through the barrier is, according to the Wentzel-Kramers-Brillouin method

$$D(V,E) \approx \exp\left(-\sqrt{\frac{8m}{\hbar^2}} \int_0^{x_o} (V(x) - E)^{1/2} dx \right) \qquad (17)$$

For the clean surface of Figure 8a, $V(x) = \mu + \bar{\Phi} - eFx$, therefore

$$D(V,E) \approx \exp\left(-\sqrt{\frac{8m}{\hbar^2}} \int_o^{x_o} (\mu + \bar{\Phi} - eFx - E)^{1/2}\, dx\right) \qquad (18)$$

Now the number of electrons with energy between E and $E + \Delta E$ increases sharply with E as long as $E < \mu$, but no electrons (at least at $0^{\circ}K$) have energies greater than μ. Because of this and the form of the exponential, we may expect that almost all of the emission will be due to electrons for which $E \approx \mu$. We shall therefore be principally concerned with the transmission probability

$$D(V) \approx \exp\left(-\sqrt{\frac{8m}{\hbar^2}} \int_o^{x_o} (\bar{\Phi} - eFx)^{1/2}\, dx\right) \qquad (19)$$

and the integral simplifies to

$$\int_o^{\bar{\Phi}/eF} (\bar{\Phi} - eFx)^{1/2}\, dx = \frac{2}{3eF}\bar{\Phi}^{3/2} \qquad (20)$$

The transmission probability is then

$$D = \exp\left(-\frac{2}{3}\sqrt{\frac{8m}{\hbar^2}}\,\frac{\bar{\Phi}^{3/2}}{eF}\right) \qquad (21)$$

which is identical to the exponential of the Fowler-Nordheim equation.

Using this approach, it is relatively simple to investigate the effect of barrier shape on the work function measurement. Three pertinent barrier shapes are shown in Figures 8b, 8c, and 8d.

For Figure 8b, the addition to the surface of a uniform dipole layer of thickness d has increased the work function by an amount $\Delta\bar{\Phi}$. The transmission coefficient becomes

$$D(V) = \exp\left(-\sqrt{\frac{8m}{\hbar^2}}\left[\int_o^{d} \left(\bar{\Phi} + \frac{\Delta\bar{\Phi}\,X}{d} - eFx\right)^{1/2} dx + \int_o^{x_o} \left(\bar{\Phi} + \Delta\bar{\Phi} - eFd - eF(x-d)\right)^{1/2} dx\right]\right) \qquad (22)$$

Evaluating the integral on the left, equation 22,

$$\int_o^d \left[\bar{\Phi} - x\left(eF - \frac{\Delta\bar{\Phi}}{d}\right)\right]^{1/2} dx = -\frac{2\bar{\Phi}^{3/2}}{3\left(eF - \frac{\Delta\bar{\Phi}}{d}\right)}\left(\left[1 - \frac{(eF - \Delta\bar{\Phi}/d)d}{\bar{\Phi}}\right] - 1\right) \quad (23)$$

Now since $(eF - \Delta\bar{\Phi}/d)/\bar{\Phi} \ll 1$,

$$\left[1 - \frac{(eF - \Delta\bar{\Phi}/d)d}{\bar{\Phi}}\right]^{3/2} \approx 1 - 3/2\left(eF - \frac{\Delta\bar{\Phi}}{d}\right)\frac{d}{\bar{\Phi}} \quad (24)$$

by the binomial theorem, and the integral reduces to $\bar{\Phi}^{1/2}d$.

If the integral on the right is similarly evaluated, to a first order approximation the transmission coefficient is found to be

$$D = \exp\left(-\frac{2}{3}\sqrt{\frac{8m}{\hbar^2}}\frac{(\bar{\Phi} + \Delta\bar{\Phi})^{3/2}}{eF}\right)\exp\left(+\frac{\Delta\bar{\Phi}\, d}{2\bar{\Phi}^{1/2}}\sqrt{\frac{8m}{\hbar^2}}\right) \quad (25)$$

Only the first exponential term of the above expression is field dependent, so that the Fowler-Nordheim plot gives a correct evaluation of the work function change. It is interesting to note that the field independent exponential is greater than one (tends to increase the field emission current) if $\Delta\bar{\Phi}$ is positive; the field dependent exponential is of course decreased if $\Delta\bar{\Phi}$ is positive.

If the adsorbate were to act as a dielectric layer of dielectric coefficient K, the potential barrier would be modified as shown in Figure 8c. The evaluation of this effect proceeds by similar arguments and leads to a transmission probability of

$$D = \exp\left(-\frac{2}{3}\sqrt{\frac{8m}{\hbar^2}}\frac{\bar{\Phi}}{eF}^{3/2}\right)\exp\left(\sqrt{\frac{8m}{\hbar^2}}\, d\bar{\Phi}^{1/2}\left(\frac{1}{K} - 1\right)\right) \quad (26)$$

in the first order approximation. Therefore, it is apparent that the effect of adsorption of a dielectric layer is to change the intercept of a Fowler-Nordheim plot although the slope (from which the work function is calculated) remains unchanged.

For the adsorption of a polarizable surface species of polarizability α_p, an additional field dependent work function of

$$\Delta\bar{\Phi}_p = 4\pi N_s \theta \alpha_p eF \tag{27}$$

would have to be added to the barrier potential. An analysis of this effect, however, shows that the transmission probability is

$$D = \exp\left(-\frac{2}{3}\sqrt{\frac{8m}{\hbar^2}}\frac{\bar{\Phi}^{3/2}}{eF}\right)\exp\left(\sqrt{\frac{8m}{\hbar^2}}\bar{\Phi}^{1/2}\,4\pi N_s \theta \alpha_p\right) \tag{28}$$

Again, the slope of a Fowler-Nordheim plot is independent of any polarizability terms. Such terms affect only the intercept.

There are conceivable adsorption models for which F-N plots conventionally interpreted would lead to erroneous work functions. Consider an adsorbate whose presence adds a deeply attractive potential well of radius r_o to the barrier (Figure 8d). The transmission probability is readily found to be

$$D = \exp\left(2r_o\bar{\Phi}^{1/2}\sqrt{\frac{8m}{\hbar^2}}\right)\exp\left[-\sqrt{\frac{8m}{\hbar^2}}\left(\frac{2\bar{\Phi}^{3/2}}{3\,eF}+\frac{r_o eFd}{\bar{\Phi}^{1/2}}\right)\right] \tag{29}$$

Therefore, the slope of the Fowler-Nordheim plot is

$$\frac{d(\ln J/F^2)}{d(1/F)} = -\sqrt{\frac{8m}{\hbar^2}}\left(\frac{2\bar{\Phi}^{3/2}}{3\,e}+\frac{r_o e F^2 d}{\bar{\Phi}^{1/2}}\right) \tag{30}$$

so that the work function is not evaluated correctly by the Fowler-Nordheim plot. For this model the F-N plot should show curvature at high fields.

For a more quantitative evaluation of the effect of barrier shape, one should include the image potential term.

APPARATUS AND EXPERIMENTAL PROCEDURES

Design and Construction of Field Emission Microscopes

The field electron emission microscope must satisfy two requirements. First, it must be an ultra-high vacuum device operating at pressures no greater than 2×10^{-10} torr in order to maintain surface cleanliness for the duration of the experiment. In addition, provision must be made for introduction of gas into the microscope in such a way that molecules which do not adsorb on the tip are pumped away immediately. This is particularly important in surface diffusion studies where the tip is initially shadowed with a directed gas source.

There are two basic tube designs suitable for chemisorption studies. The first is a tube designed for total immersion in liquid helium or hydrogen; such a design has been used by Gomer (13) and Arthur (3). The second is a continuously pumped tube designed by Müller for field ion emission studies and later adapted for field electron emission investigation of chemisorption by Ehrlich (15). The total immersion microscope is the less versatile, but is outstanding in the ease with which ultra-high vacuum conditions are obtained, and for this reason was used exclusively in this work. A typical total immersion tube is shown in Figure 9.

While Gomer (13) has discussed generally the construction of total immersion field emission microscopes, the author has found a number of

techniques, not well described in the literature, to be particularly convenient in preparing satisfactory instruments. These techniques are illustrated by the following preparations:

Tungsten to glass seals

Because the field emission tubes require electrical feed-throughs, glass to metal seals are an integral part of the microscope. These seals must be absolutely reliable since even small leaks would prevent the realization of ultra-high vacuum conditions in the microscope.

The tungsten to glass seals were made from .050 in sealing grade tungsten wire and Corning 7750 Nonex glass. The tungsten was cut to length on a carborundum cut-off wheel, outgassed with a torch, and cleaned by etching at 10 volts ac in a 1N sodium hydroxide solution. The ends of the rod were polished at 30 volts to avoid spurious emission and washed carefully to remove all traces of sodium hydroxide. The tungsten rod was then oxidized in a bushy, fuel-rich flame by holding the wire in the flame until it barely began to glow, after which it was removed quickly. The color should vary from a deep purple to dull blue. Unlike uranium glass seals the degree of oxidation is not particularly critical. A Nonex sleeve was sealed on using an oxygen rich flame. The beaded sleeve was cleaned in concentrated hydrochloric acid to remove the lead and then thoroughly washed. The remainder of the seal was constructed in the normal manner (3). Press seals of Nonex up to 25 mm in diameter

can be sealed directly to Pyrex glass.

Conductive coating

The best anode arrangement is a conductive, transparent film of tin oxide beneath the phosphor screen.

The conductive coating, D of Figure 9, was applied by blowing, with nitrogen gas, fumes of anhydrous stannic chloride into the tube which was held at temperatures between 500°C and 550°C in an oven. Very clear and conductive films resulted if a gentle stream of air was blown into the tube simultaneously with the stannic chloride. It was necessary to cover with platinum paint all portions of the tube which were not to be coated. After deposition of the film, the platinum paint was removed by hydrofluoric acid or an ammonium bifluoride solution. Unwanted coating can also be removed by covering that portion of the coating with zinc dust and adding dilute hydrochloric acid, or by dipping the coated glass in hydrofluoric acid.

Connection to the conductive coating was made by a tungsten hairspring contact, Figure 10. The hairspring contact was constructed from a tungsten single lead press seal using a nickel rod between the hairspring and tungsten rod. This contact was satisfactory for most applications, its only disadvantage being that it was not completely reliable. Apparently after three or four bakeouts, the tungsten spring annealed and had a tendency to draw away from the conductive coating.

Screen

The screen, I, was applied by the puffer technique (13) using Sylvania type CR202 aluminizing phosphor. Eight to ten drops of concentrated phosphoric acid were dissolved in one ml acetone. Four drops of this solution were added to the tube and spread using a few glass beads. After evaporation of the acetone, the phosphor was blown on using a puffer, Figure 11, until an opaque screen of uniform density was obtained. After the excess phosphor was removed and the tube cleaned the screen was baked at 500°C for two hours.

Tip assembly

The tip support assembly is shown in Figure 9. The filament was 0.010 in tungsten wire, 7 cm in length. The potential sensing leads used for temperature control were 0.003 in tungsten wire.

Tip temperatures were obtained by using the filament as a resistance thermometer, the resistance being determined by measuring the current and the voltage across the filament. Since the ends of the filament were always at the temperature of the refrigerant, the filament temperature at steady state conditions was not uniform, but very nearly parabolic. Therefore, the potential leads were placed sufficiently close to the center of the filament, 0.5 to 0.7 cm, that the average temperature measured did not differ more than 1% from the temperature at the tip.

For adequate temperature control, it was necessary to insert an

alloy as a thermal barrier between the filament and refrigerant. This was necessary since, for pure metals, not only thermal and electrical conductivities but also their rates of change with temperature become so great at low temperatures that sudden large temperature changes can occur for small current changes. A 1 cm length of 18 gauge nichrome wire was used for the filament support with 2 cm lengths of 28 gauge nichrome wire used for support of the potential sensing leads.

Tip preparation

The preparation of tips, free of contaminants, with sufficiently small radii is one of the more difficult techniques in field emission microscopy. Tips are normally formed by electrochemical etching, the specific technique depending on the metal, the degree of recrystallization, and the presence of contaminants in the metal. There are three characteristics that all tips should have if possible. (1) They should be sharp with radii of 1000-5000Å. If it is difficult to resolve the end of the tip at 400-500 x magnification, this requirement is generally satisfied. (2) The tip should have a long slender smooth taper. Tips with high tapers tend to blunt excessively on heating. (3) Since it is necessary that the tip assumes the same temperature as the filament, the total length of the tip should be as short as possible.

A technique that generally produced good tungsten tips is illustrated in Figure 12. A .005 in or .010 in wire approximately 2 in

long was nearly completely immersed in the etching solution, 1N NaOH, and etched at 4 volts ac until it was sharply pointed, Figure 12b. The tapers shown are exaggerated for clarity. The wire was then cut off a short distance from the sharpened end and the thin end was spot-welded onto the filament. At this stage, the entire tip assembly was immersed into the solution and briefly etched at 4 volts so as to avoid spurious emission. The wire was then inserted as nearly vertically as possible into the etchant to a depth where the etchant nearly touched the filament, Figure 12c. The wire was etched at 1 V until it broke off (the break occurred near the filament) and the etching process was terminated immediately. At this stage the tip had the general shape shown in Figure 12d. A final brief etch at reduced voltage was sometimes necessary for the sharpest tips.

Vacuum System and Gas Handling

For chemisorption studies, the microscope tube has to be processed by normal ultra-high vacuum techniques before it is loaded with the gas under investigation. The reasons for this are two-fold. First, before the tube is loaded, the tip should be cleaned and inspected for spurious emission. Pressures less than 1×10^{-7} torr are required since, at higher pressures, the tip is bombarded by ions formed in the field near the tip and the tip is destroyed. Second, the phosphor screens contain appreciable quantities of adsorbed and occluded gas which is liberated

when the electron beam from the tip impinges on the screen. As a result the work function of the emitter changes during the time interval required for measurement. Baking the microscope at 450°K under ultra-high vacuum conditions greatly reduces the degassing of the screen.

The vacuum system used for this work is shown schematically in Figure 13. The components enclosed in the dotted line were mounted on a vertical transite board. This area was bakeable by a portable oven. The glass between the diffusion pump and the cold trap and between V_1 and V_2 could be baked by heating tapes. Valves V_1 and V_2 are Granville-Phillips Type C ultra-high vacuum valves. Valve V_3 is a Granville-Phillips Type C high pressure valve which received the gas bottle on the high pressure side. Valve V_4 is a stopcock to an independent pump for the gas handling portion of the system.

The ethylene gas used was Phillip Research Grade with a specified purity of 99.98 mole percent. It was used without further purification.

The acetylene used was from Matheson Company with impurities of 0.5% methane, 0.5% ethylene and ethane, and 0.5% nitrogen. There were trace impurities of oxygen, argon, and carbon monoxide. The acetylene was purified by repeated distillations from a cold finger cooled by a n-pentane slush (143°K).

Cryostat

The use of cryogenic techniques for field emission microscopy requires only minor modifications of standard cryogenic practices (13).

The cryostat must have unsilvered windows in both helium and nitrogen dewars for photographic purposes. In addition, provision must be made to stop the nitrogen bubbling while photographing the image. This is easily accomplished by pressurizing the nitrogen. The cryostat used for these studies is shown in Figure 14. A is the transfer port; B is the high voltage feed through, consisting of a wire incased in an evacuated glass tube, needed to prevent a high voltage discharge in the gaseous helium; C is a port leading to a pop-off valve and a vacuum pump; D a stopcock leading from a pump to the inner dewar jacket; E is a press seal providing electrical connection to the silvering in the inner dewar serving to shield electrical noise; F are rubber tubes; G are the unsilvered portions of the dewar; H is a vent for the liquid nitrogen jacket; I is the electrical feed through for the microscope; J is a pipe flange supporting the inner dewar; and K is an O-ring for the flange assembly.

Electrical Equipment

The principal electrical requirements for field emission microscopy are a high voltage (1-30 kv range) power supply, an electrometer for the measurement of current in the range 10^{-14} to 10^{-5} amperes, a voltage divider for voltage measurements, and a tip temperature controller, Figure 15. For reliable data in catalysis studies, the work function changes need to be determined within .02 ev. In practice, this requires that voltages of several thousand volts be determined to within 0.1%,

and currents of 10^{-10} to 10^{-6} amperes to within 1 to 3%.

The power supply is a Sorenson Model 5030-4, with an output of 5 to 30 kilovolts. The regulation of the power supply is 0.05% with ripple less than 0.02%RMS. The ammeter is a Cary Model 31 vibrating reed electrometer.

The voltage divider is shown in detail in Figure 16. Four Shallcross Model 505-5 meg ohm high voltage resistors were connected in series to provide a 20 meg ohm total resistance. R_1 is a 1 K ohm resistor used for calibration of the divider. R_2 is a 10 K ohm helipot that is adjusted such that the voltage drop across it is 1/1000 of the voltage appearing at the output cables of the divider. R_3 and R_4 are 1 K ohm helipots. The divider was calibrated by applying a known voltage across the whole divider and measuring the voltage drop across cable II and R_1. Thereafter, R_2 was adjusted so that the digital voltmeter, Fairchild Model 7100, read to within 0.1%, 1/1000 of the voltage drop across cable II.

The current-voltage data for the Fowler-Nordheim plots were recorded on an X-Y recorder with the voltage plotted on the X axis and current, obtained from the output of the electrometer, plotted on the Y axis. The 1.3 V mercury battery and R_4 serve as a zero suppressor. R_3 and R_4 are adjusted so that the recorder voltage scale is in the order of 25 to 50 volts per inch on the X axis.

The analysis of the kinetic data is simplified if the reactions are

carried out isothermally. The tip, initially in thermal equilibrium with the liquid helium, must be heated rapidly to the desired temperature (between 50° - 2000°K) and held at temperature with no overshoot. The control was achieved employing a Kelvin double bridge circuit (16). The circuit is shown in block diagram in Figure 17. The differential dc amplifier senses the error signal from the bridge and rapidly adjusts the heating current from the power supply until the standard and loop resistances are equal.

Only a minor modification of a normal power supply is necessary. Since a no-current condition is also a null, this null has to be eliminated by passing a small constant current through the bridge. The small current (100 ma) can be most easily obtained from the pre-regulated output of the power supply. Depending on the voltage at the tap-off point, the resistance R is selected to achieve the current level.

The bridge is shown in greater detail in Figure 18. Included is a switching circuit so that the filament may be operated in different modes. The four switch positions are: Position 1, an outgas mode which supplies approximately 5-7 amps from a 20 volt power supply for outgassing the filament and tip; Position 2, a heat mode which connects the double bridge to the filament and connects the recorder to the filament such that a voltage drop proportional to the heating current through the filament appears on the X axis, and the voltage drop across the sensing leads of

the filament appears across the Y axis; Position 3, a monitor mode for filament temperature where a 0 to 100 ma current passes through the filament so that the resistance (temperature) of the filament may be determined for calibration purposes or to check filament temperature after a flash; and Position 4, a Fowler-Nordheim mode which connects the recorder to the voltage divider and the output of the electrometer.

The differential dc amplifier is a Sanborn Model 860-4300 with a gain of 500 and a very low zero drift, $\pm$ .1 mv referred to the output, for 40 hours. In practice, this meant that the resistance calibration versus dial setting on the double bridge changes less than 1% per month and was independent of the of the filament in use.

The power supply for the controller had a maximum output current of 3.5 amps. As a result, it was the limiting factor in the time required for the filament to reach temperature. The performance of the bridge is illustrated in Figure 19. The dotted line is the line of constant resistance. The time interval between B and C was .25 sec., between C and D, 0.1 sec., and between D and E 0.05 sec. The small overshoot between C and D is due to the mechanical inertia of the recorder pen. The time interval between A and B was 5 sec.

RESULTS

Surface Diffusion

The field emission microscope lends itself nicely to surface diffusion studies, providing visual evidence of the variation in surface forces acting on migrating adatoms. By suitable arrangement of the tip and gas source, only a portion of the emitting area is covered with adsorbate if the initial temperature of the tip is sufficiently low. Subsequent heating results in surface diffusion which can be photographed.

There have been three general types of diffusion observed (13), the type of diffusion being markedly dependent on surface coverage and temperature.

Type I diffusion: Characterized by a sharp boundary which moves nearly uniformly over the tip.

Type II diffusion: Characterized by a sharp boundary which moves non-uniformly over the tip.

Type III diffusion: Characterized by non-uniform diffusion with lack of a boundary.

The observation of sharp boundary is, in itself, interesting because it implies diffusion with rapid precipitation on a restricted number of sites. The density of sites must be such that the average site to site distance is less than the resolution of the microscope. The diffusion

can be considered most simply as a random walk process where the distance traversed by the boundary in time t is

$$X = \sqrt{2Dt} \tag{31}$$

where D is the diffusion coefficient. The diffusion coefficient is given by

$$D = l^2 \nu_d \exp(-E_d/RT) \tag{32}$$

Here l is the average jump distance, ν_d is the frequency factor (on the order of kT/h) and E_d the activation energy for diffusion.

Type I diffusion occurs between upper and lower temperature limits at high initial surface coverages with activation energies of diffusion of 0.5-3 kcal. The mechanism appears to be the migration of physically adsorbed gas on top of an immobile chemisorbed layer with precipitation at the edge of the chemisorbed layer (17).

Type II diffusion has been shown to be the migration of the chemisorbed layer (17). The diffusion occurs at higher temperatures and lower coverages than Type I diffusion, with corresponding higher energies. The rate of diffusion is strongly dependent on crystallographic direction and is generally greatest along the 110-112 zones which consist essentially of 110 terraces and are closely packed. Type II diffusion has been ascribed to the migration of the chemisorbed layer across diffusion sites with precipitation in trap sites, the density of the trap sites being sufficiently large that the average distance between trap sites is less than the resolution of the microscope (17).

Type III diffusion, which occurs at low surface coverages, differs from Type II in that a sharp boundary is not observed and the activation energies for diffusion are normally higher (13). Here again, the diffusion has been ascribed to migration of the chemisorbed layer with precipitation, except that for Type III diffusion, the average distance between trap sites exceeds the resolution of the microscope.

For partially dosed emitters, moving boundaries are observed for both acetylene and ethylene over the temperature range 70°K to 100°K. The diffusion is clearly a Type I process since it occurs at such low temperatures and has both upper and lower temperature limits. However, the boundary does not move uniformly across the tip, in contrast to all other gases studied (which have been exclusively mono-atomic and di-atomic gases).

Diffusion of acetylene

Figure 20 shows the diffusion sequence for acetylene. Figure 20a is a clean tungsten pattern. In 20b the emitter, held at approximately 50°K, has received a dose on the upper half of the tip. The boundary has moved nearly uniformly until the central 110 plane is encountered. By Figure 20d, the 110 plane has been encircled by the layer surrounding the plane and filling in from the back side; there is no evidence of migration across the 110 plane. At this point, the diffusion stopped, apparently because the supply of physically adsorbed gas was depleted. Figure 20e

and 20f show the pattern changes as the emitter was heated for 20 seconds at the temperatures indicated. By 450°K, surface reactions have occurred as evidenced by the pattern changes, but the boundary has not moved. Therefore, acetylene does not exhibit Type II diffusion, i.e., chemisorbed acetylene is immobile.

The apparent motion of the boundary around the 110 plane might be due to an inability of this plane to adsorb acetylene at all, so that acetylene is effectively repelled from the plane. This explanation is untenable, for at 50°K the order of magnitude of van der Waals interaction energy is sufficient to insure strong physical adsorption of any gas whose normal boiling point is as high as that of acetylene (189°K). We must suppose, therefore, that acetylene in fact moves onto this plane. To account for the boundary behavior then, we must suppose that the density of sites for acetylene chemisorption on the 110 plane, far from being zero, is <u>much greater</u> than on the surrounding faces, so that the 110 plane acts as an acetylene sink, depleting acetylene from immediately adjoining regions. This explanation is tenable, and in fact accords well with the known spatial arrangement of tungsten atoms on this plane and the expected geometry of acetylene chemisorbed on tungsten. Chemisorption studies (18) have suggested that acetylene is chemisorbed by forming two σ -bonds with the surface metal atoms to give an ethylene-like structure. Assuming that bond lengths are given by the sum of the covalent radii,

the optimum tungsten-tungsten can be calculated, Figure 21. The following values for bond lengths are used:

(a) d_{w-w} 2.74Å

(b) d_{w-c} 2.04Å

(c) $d_{c=c}$ 1.35Å

The optimum d_{w-w} distance can then be calculated from

$$\cos\theta = \frac{d_{w-w} - d_{c=c}}{2(r_c + r_w)} \tag{33}$$

assuming α to be 120°. The optimum tungsten-tungsten distance can be found to be 3.39Å.

The 110 plane is shown in Figure 22. In the direction O-A the tungsten-tungsten distance is 3.16Å, and, in the O-B direction, 2.74Å. The 2.74Å distance is clearly too short. If acetylene were to adsorb on the 3.16Å spacing, the W-C-C angle would be about 117° instead of the normal 120°. The strain on this bond is therefore relatively small. From an examination of Figure 22, which shows the packing of a number planes of interest, and Table 1, which gives the density of types of sites available on a given plane, it is evident that the 110 plane has the greatest density of 3.16Å spacings, followed by the 100 plane. An examination of motion picture films of the diffusion process revealed that the 100 plane behaved in a very similar manner to the 110 plane. Since the 100 is completely lacking in 2.74Å spacings, this observation tends to confirm that the 3.16Å spacings are the pairs of sites involved

in acetylene chemisorption.

The boundary was also deflected slightly in the area of the 112 plane. From Figure 22, it can be seen that the 3.16Å spacing involves one tungsten atom which is in a trough. While there are no steric factors to prohibit acetylene chemisorption utilizing this site, it would nevertheless seem to be unlikely since the tungsten atom in the trough is nearly completely coordinated (it has a coordination number of seven). This would suggest however that the 2.74Å spacings along the rows are more likely sites for chemisorption. It may be that both 2.74Å and 3.16Å spacing can chemisorb acetylene; however, this can not be resolved by field electron emission microscopy.

Diffusion of ethylene

The Type I diffusion of ethylene is shown in Figure 23. In Figure 23a, the upper half of the emitter has received a dose. In Figure 23d, it is apparent that the 110 plane does not behave as a sink for ethylene chemisorption. Now the 112 plane appears to be retarding the boundary. From Figure 23e, it is also apparent that the 111 plane also represents an area of high site density since the 112 plane above it has not been encircled by the migrating layer. The diffusion ended, Figure 23f, when the physically adsorbed ethylene was depleted. The boundary shown in Figure 23f remained immobile at all temperatures where the ethylenic species exists on the surface, i.e. Type II diffusion was not observed

for ethylene.

The reversal of the roles of the 112 and 110 planes for ethylene diffusion compared to acetylene diffusion is extremely interesting and provides insight into the chemisorption of ethylene that, hitherto, has been overlooked in the literature.

By analogy with acetylene, the associative chemisorption of ethylene is generally shown as

$$H_2C - CH_2$$
$$\quad / \quad \backslash$$
$$\quad * \quad\quad *$$

where the bond lengths and angles are assumed the same as ethane ($d_{C-C} = 1.54\text{Å}, \alpha = 109^\circ$). The optimum tungsten-tungsten distance is found to be 2.94Å. The 2.74Å and 3.16Å spacings available on the 110 plane would distort the W-C-Cangle only 3° ($\alpha = 112^\circ$ for the 2.74Å spacing and 106° for the 3.16Å spacing). Nevertheless, the density of sites on the 110 plane appears to be small for ethylene chemisorption.

The 112 plane, which behaves as a sink for ethylene, has, in addition to the 2.74 and 3.16Å spacings, an abundance of 4.47Å spacings across the trough. Since it has already been established that the shorter spacings are not important for ethylene chemisorption, the 4.47Å sites must be responsible for high activity of the 112 plane.

From Table 1 and Figure 22 the 111 has the next highest abundance of 4.47Å spacings. The behavior of the 111 plane as an area of high site

density is in complete accord with the assignment of the 4.47Å spacings as those reponsible for ethylene chemisorption.

Since the optimum tungsten-tungsten distance for "cis" ethylene adsorption (the tungsten and carbon atoms in the same plane) is 2.94Å, it is evident that, to span the 4.47Å spacing, the chemisorption of ethylene must be "trans", Figure 24. If ethylene were fully extended such that the tungsten and carbon atoms were all in the same plane with the tungsten atoms in a "trans" position the tungsten-tungsten distance could be as much as 5Å; therefore, it is entirely reasonable that ethylene chemisorbed "trans" can span the 4.47Å spacing.

Twigg and Rideal (19) discussed the geometric properties of associatively chemisorbed acetylene and ethylene on nickel. Their results are shown in Table 2, (from Bond (20), using more recent covalent radii).

They assumed that the 3.50Å distance was too great for ethylene chemisorption, and that the adsorption took place on the 2.47Å spacing. Apparently the possibility of a "trans" adsorption was overlooked, a situation which persists in the present day literature (2, 20, 21, 22).

In recent years, olefins and acetylenes have been found to function as ligands towards transition metals (23). Such complex species have been described by π donor bonding with the transition metal. Bond and Wells (2), in a recent review of the hydrogenation of unsaturated olefins,

discuss the bonding of ethylene on a metal surface in similar terms. The carbon atoms are still sp^2 hybridized, and the carbon atoms and groups attached to the carbon atoms are coplaner in a plane parallel to the surface. Such species are written as

$$CH_2 = CH_2$$
$$\quad\;\; | \quad\;\; | \quad\;\; *$$

and only one metal atom in the surface is required for bonding although others may be obscured by the adsorbed molecule. The field emission evidence presented above, however, clearly rules out the π bonding concept as a mode of adsorption for ethylene since the 110 plane, which is the most closely packed plane in a body-centered cubic metal, does not behave as an area of high site density.

Surface Reactions

To interpret work function data in terms of surface reactions, it is necessary to examine the kinetics of surface reactions. The rate equation for a simple isothermal surface reaction is

$$-\frac{d\theta}{dt} = k\theta^n \tag{34}$$

which, when integrated gives

$$\begin{aligned} &-\ln \theta/\theta_o = k\Delta t && \text{first order } (n = 1) \\ &1/\theta_o - 1/\theta = k\Delta t && \text{second order } (n = 2) \end{aligned} \tag{35}$$

where

$$k = \nu_n \exp(-\Delta H/RT) \tag{36}$$

ν_n is the frequency factor and ΔH is the enthalpy of activation. It is possible in principle to determine the order and energetics of a surface

reaction by plotting kinetic data as suggested by equations 35 and 37. Normally, when kinetic data for surface reactions are analyzed in this manner, it is found that neither first nor second order plots yield straight lines. Arthur found this to be the case for the decomposition of acetylene and ethylene or iridium (3). In most cases of chemisorption it is experimentally found that the heat of chemisorption decreases seriously with increasing surface coverage. This phenomenum has been examined by deBoer (24) who reached the following conclusions.

1. The decrease of ΔH with increasing surface coverage is due mainly to the change in work function of the metal by the dipole layers formed by the chemisorbed atoms. This is termed a "work function effect" and leads to a linear decrease in ΔH with surface coverage.

$$\Delta H = \Delta H_o - \alpha\theta \tag{37}$$

Boudart, assuming that the electrical double layer could be approximated by a uniform dipole sheet (25), evaluated α to be

$$\alpha = 1/2\ \Delta\Phi = 2\pi\theta N_s M \tag{38}$$

the factor of 1/2 coming from the assumption that the electron is located halfway between the planes of the double layer, and, as a result, has to do work against only 1/2 of the potential difference. The assumption of a uniform dipole layer has been criticized by Gomer (26) who evaluated the potential due to a discrete dipole layer and argued that, at low θ values, the effect would be considerably smaller than that calculated by Boudart.

2. The mutual depolarization of the surface dipole, due to dipole-dipole interactions, may affect the linearity of equation 38 since the dipole moment per adatom is now a function of coverage. This effect can cause a maximum or minimum in the surface potential as a function of θ (24).

Nevertheless, there is much experimental evidence (24) that ΔH is nearly a linear function of θ, and for a first order approximation, ΔH will be assumed linear with θ for the remainder of this discussion. Combining equations 34, 36 and 37,

$$- d\theta/dt = \nu_n \theta^n \exp(-\Delta H_o/RT) \exp(\alpha\theta/RT) \tag{39}$$

At this point, it is interesting to examine to what extent n, ΔH_o and α can be uniquely determined from the rate equation. The problem can be simply stated by writing equation 39 in another differential form.

$$\begin{aligned} d(\ln\theta)/dt &= \nu_1 \exp(-\Delta H_o/RT) \exp(\alpha\theta/RT) \text{ for } n = 1 \\ &= \nu_2 \exp(-\Delta H_o/RT) \exp(\alpha\theta/RT)\,\theta \text{ for } n = 2 \end{aligned} \tag{40}$$

It is readily seen from equation 40 that, if $\frac{\alpha\theta}{RT}$ is approximately one or greater, it will be difficult to determine even the order of the reaction since the exponential dependence on θ will tend to mask any difference between the first and second order analysis. This is not a trivial problem, for values of α of 10-30 kcal/monolayer are quite common. Consider, for example, a reaction for which ΔH_o is 40 kcal/mole and

α is 20 kcal/monolayer mole. For the term $\alpha\theta/RT$ to be less than one requires that one limit the investigation to surface coverages of less than approximately 0.07 monolayers.

Assuming that data can be obtained where $\alpha\theta/RT$ is less than one, one can attempt an evaluation of ΔH_o and order of the reaction by collecting the data at low surface coverages and assuming that, for small coverage intervals, ΔH is nearly constant. Therefore, equation 34 can be utilized, the order of the reaction being determined by comparing linearity of plots of $\ln\theta$ vs t and of $1/\theta$ vs t. One should be aware, however, of possible errors in judgement in the degree of linearity of the two plots. If a reaction obeys first order kinetics and is analyzed by the above mentioned procedure, the following equations apply:

$$d(\ln\theta)/dt = \nu_1 \exp(-\Delta H_o/RT)\exp(\alpha\theta/Rt) \qquad \text{first order reaction (plotted first order)}$$

$$-d(1/\theta)/dt = \nu_1 \exp(-\Delta H_o/RT)\exp(\alpha\theta/RT)(1/\theta) \qquad \text{first order reaction (plotted second order)} \qquad (41)$$

The second order plot of a first order reaction yields a sigmoidal curve with a point of inflection at $1/\theta = \alpha/RT$ while the first order plot has no inflection point. If this inflection point is near the middle of the experimental range, the second order plot of a first order reaction may be more nearly linear than the first order plot, and the kinetic order may be incorrectly assigned.

This is illustrated in Figure 25. Surface coverage vs time curves

were generated for a first order reaction using equation 39 with ΔH_o equal to 30 kcal for two values of α, 20 kcal/monolayer mole and zero, Figure 25A. A comparison for first and second order plots of the α equal to zero curve shows the trite result that the reaction was indeed first order, Figure 25b. However, for α equal to 20 kcal/monolayer mole, the reaction may mistakenly be supposed to be second order since, in Figure 25c, the $1/\theta$ plot appears to be more linear than the $\ln \theta$ plot.

A similar analysis of a second order rate equation shows that identification of a second order reaction as first order is less likely.

The conclusion to be reached from this discussion is that, for many reactions in catalysis (adsorption, desorption, decomposition reactions, etc.,) α is normally greater than 10 kcal/monolayer mole; and, as a result, it is not possible to determine uniquely the order of the reaction n, ν_n, ΔH_o or α by field emission or any other technique now available.

Thus, it is necessary to reduce the rate equation to a three parameter problem by establishing one parameter independently. It is common to assume ν_n to be given by simple rate theory, i.e. ν_n equals (kT/h) for first order and $(\sigma \pi kT/m)^{1/2}$ for second order where σ is the hard sphere collision diameter.

Integrating equation 39

$$\nu_n \exp(-\Delta H_o/RT)t = E_1(X) - E_1(X_o) \quad n = 1$$

$$= \alpha/RT\left[\exp(-X)/X - \exp(-X_o)/X_o + E_1(X) - E_1(X_o)\right] n = 2 \qquad (42)$$

where

$$E_1(x)=\int_x^{\infty} \exp(-y)/y \, dy \qquad X = \frac{\alpha\theta\ (t)}{RT} \quad X_o = \frac{\alpha\theta\ o}{RT}$$

The values of $E_1(X)$, the exponential integral have been tabulated (27). Equation 42 can be vastly simplified if the following approximations are made.

(1) Since, for $0 < \theta < 0.8$

$$\int_{\frac{\alpha\theta}{RT}}^{\infty} \exp(-y)/y \, dy \geq 100 \int_{\frac{\alpha\theta_o}{RT}}^{\infty} \exp(-y)/y \, dy \tag{43}$$

$E_1(X_o)$ can be neglected compared to $E_1(X)$.

(2) In addition, $E_1(X)$ can be approximated by (28)

$$E_1(X) = f(X)/X \exp(-X) \tag{44}$$

where $.72 < f(x) \leq 1$ for $2 < X < \infty$ and, to a sufficient accuracy for the present purposes $f(X) = 1$.

Hence

$$E_1(X) \approx \frac{1}{X} \ e^{-X}$$

Equation (42) now simplifies to

$$\begin{aligned} t\,\nu_n \exp(-\Delta H_o/RT) &= RT/\alpha\,\theta \exp(-\alpha\,\theta/RT) \quad n = 1 \\ &= 2/\theta \exp(-\alpha\theta/RT) \quad n = 2 \end{aligned} \tag{45}$$

Taking ν_n from the simple rate theory expressions given, we have

$$\begin{aligned} T &\approx -\alpha\theta/69 + \Delta H_o/69 \qquad n = 1 \\ &\approx -\alpha\theta/65 + \Delta H_o/65 \qquad n = 2 \end{aligned} \tag{46}$$

which relates, at a constant time interval of 30 seconds, the coverage as a function of temperature.

Figure 26 illustrates generated data from equation 42 for a simple first order desorption reaction where ΔH_o = 45 kcal/mole, α = 20 kcal/monolayer mole and $\nu_1 = kT/h$. For a desorption time interval of 30 seconds, the surface coverage was plotted as a function of temperature, Figure 27. Over the range, $.2 < \theta < .8$ the plot is indeed linear. From the intercept, ΔH_o was calculated to be 47.6 kcal/mole, and α, 21.5 kcal/monolayer mole which compares favorably with those values used to generate the data.

To apply equation 46 to the work function data obtained for the decomposition of the acetylene and ethylene, it is necessary to assume that the total work function can be considered as the sum of the work function of the clean surface plus the additional terms due to the presence of reactants and products. In general, the reactants and products will have different dipole moments; therefore, as the reactions occur, the total work function will change.

The surface reaction experiments were conducted in the following manner. The emitter was first cleaned by flashing, cooled to 4°K, and the field emission current and voltage data for the work function measurements were collected. The emitter was then dosed with gas by warming the source briefly. The dosing was carried out with the field turned off. The emitter was heated to 70-80°K, relying on Type I diffusion to cover the entire emitting area of the tip. A work function vs temperature

plot was obtained by heating the tip to a temperature T for a time interval of 20 seconds in the absence of the field, then cooling to $4^{o}K$ and applying a field. At this time the image was photographed and the work function determined. By always taking work function measurements at $4^{o}K$, field induced reactions which might have occurred at higher temperatures were avoided.

Acetylene

Figures 28 - 32 show the emission pattern changes as the tip covered with acetylene is heated from $100^{o}K$ to $1050^{o}K$ for periods of 20 seconds at each temperature. All photographs were taken at 1×10^{-7} amperes emission current.

Figure 33 shows the corresponding work function vs temperature plots. The work function was evaluated by both single point and Fowler-Nordheim techniques. The initial decrease in work function, as measured by single-point techniques, in the range $75-100^{o}K$ is due to the desorption of physically adsorbed acetylene. The physically adsorbed layer acts as a dielectric layer which, as previously shown, affects only the pre-exponential portion of the F-N equation. This is reflected in the single point measurement since the dielectric layer reduces the current.

The Fowler-Nordheim and single-point calculations of the work function are compared in Figure 34. For temperatures between $100-600^{o}K$, the relationship between the two determinations is given by

$$\Delta\Phi_{F.N.} = 1.05\ \Delta\Phi_{S.P.} - .17 \tag{47}$$

From 100°K to 400°K, the qualitative features of the work function change with temperature are similar for both methods of evaluating the work function. Upon adsorption of acetylene, the work function is lowered by 0.5 ev and it remains unchanged at temperatures up to 300°K. In the interval 300-450°K, the work function increases rapidly. There is a definite change in slope in the curve between 450° and 575°K. Between 575° and 700°K, the curve is nearly linear. The work function reaches a maximum at 725°K, remains constant until 850°K and then decreases.

Preliminary mass spectrometric studies of acetylene on tungsten have indicated that above 100°K, hydrogen is the only desorption product and that the hydrogen evolution is complete by 800°K (29). The increase in work function in the temperature interval 300-800°K is therefore due to a surface reaction and not simply the desorption of acetylene. The simplest model for the decomposition reaction is

$$C_2H_2 \rightarrow 2H + C_2 \tag{48}$$
$$\quad\ ** \qquad\quad * \quad\ *$$

where C_2 represents the carbon residue left on the surface. The total work function is then given by

$$\Delta\tilde{\Phi} = \Delta\Phi^{C_2H_2}_{max.}\ \theta_{C_2H_2} + \Delta\Phi^{C_2}_{max.}\ \theta_{C_2} + \Delta\Phi^{H}_{max.}\ \theta_{H} \tag{49}$$

For the present, assume that the hydrogen produced by the decomposition reaction desorbs at all temperatures so that only C_2H_2 and

C_2 are present on the surface.

Then equation 49 becomes

$$\Delta\bar{\Phi} = \Delta\bar{\Phi}^{C_2H_2}_{max.}\,\theta_{C_2H_2} + \Delta\bar{\Phi}^{C_2}_{max.}\,\theta_{C_2} \qquad (50)$$

and since $\theta_{C_2} + \theta_{C_2H_2} = 1$,

then

$$\theta_{C_2H_2} = (\Delta\bar{\Phi} - \Delta\bar{\Phi}^{C_2}_{max})/(\Delta\bar{\Phi}^{C_2H_2}_{max.} - \Delta\bar{\Phi}^{C_2}_{max.}) \qquad (51)$$

As $\Delta\bar{\Phi}^{C_2}_{max}$ and $\Delta\bar{\Phi}^{C_2H_2}_{max}$ are constant and from the extreme value of the work function plot, i.e., $\Delta\bar{\Phi}^{C_2H_2}_{max} = -0.48$ ev and $\Delta\bar{\Phi}^{C_2}_{max} = 0.48$ ev, the work function is linearly related to the surface coverage of acetylene. Figure 35 shows the work function curve that would have been obtained had the hydrogen produced by the decomposition been desorbed at a rate that was fast compared to the decomposition. In the temperature interval 300-600°K, the measured work function is greater than predicted on this basis and the discrepancy is due to the presence of hydrogen on the surface. Hydrogen raises the work function on a clean tungsten surface (17). The work function vs temperature plot for hydrogen is also shown in Figure 35.

The shape of work function curve can now be related to the surface reactions of acetylene. At temperatures between 100-300°K, acetylene is associatively chemisorbed on the surface; neither the work function nor electron image changes with temperature. In the temperature interval

300-450°K, the work function increase is due to the decomposition of acetylene producing hydrogen and a carbon residue on the surface.

$$\underset{*}{C_2}\underset{*}{H_2} \rightarrow \underset{**}{C_2} + 2\underset{*}{H} \tag{52}$$

In the interval, 450-600°K, the hydrogen desorbs from the surface

$$\underset{*}{C_2}\underset{*}{H_2} \rightarrow \underset{**}{C_2} + 2\underset{*}{H}$$

$$2\underset{*}{H} \rightarrow H_2(g) \tag{53}$$

and above 600°K, the hydrogen desorption is fast so that the only surface species are C_2H_2 and C_2. By 750°K, the decomposition is complete and the work function remains constant until 850°K when it decreases. The decrease is apparently due to a redistribution of carbon which is mobile at these temperatures, and possibly also to a decrease in surface concentration of carbon due to the diffusion of carbon into the bulk of the metal (30).

The dependences of surface concentrations on temperature can be obtained from the work function plot and are shown in Figure 36. The parameter θ should be understood as relating to the extent of the reaction and not as implying that, for θ equals 1, all tungsten surface atoms serve as occupied sites.

Using equation 46 ΔH_o and α are found to be 50 kcal/mole and 23 kcal/mole monolayer from the slope and intercept of Figure 35. Since these values refer to the decomposition reaction,

$$\underset{*}{C_2}\underset{*}{H_2} \rightarrow \underset{**}{C_2} + H_2\,(g)$$

it is necessary to examine more carefully what is included in these terms. For the reaction of equation 53, ΔH is given by

$$\Delta H = \Delta H_o' - \alpha_{C_2H_2}\theta_{C_2H_2} + \alpha_{C_2}\theta_{C_2} \tag{54}$$

where $\Delta H_o'$ is the enthalpy of activation for the dissociation. Since the C_2H_2 species forms a dipole layer positive out, and carbon one negative out, the carbon dipole layer, as a result of the work function effect, will increase the enthalpy of activation for the dissociation. Hence, the $\alpha_{C_2}\theta_{C_2}$ term is positive in equation 54. Substituting for θ_{C_2}, we have

$$\Delta H = \Delta H_o' + \alpha_{C_2} - (\alpha_{C_2H_2} + \alpha_{C_2})\theta_{C_2H_2} \tag{55}$$

It is probable that $\alpha_{C_2H_2}$ equals α_{C_2} since $\Delta\Phi_{max}$ for both species is 0.5 ev. Therefore, $\alpha_{C_2H_2}$ and α_{C_2} are equal to 11.5 kcal/monolayer mole; and $\Delta H_o'$ is 38.5 kcal/mole.

The decomposition of acetylene was also studied on a carbon-tungsten surface. This surface was produced by covering a clean tip with acetylene and heating to 800°K to decompose the acetylene, leaving a carbon residue on the surface. The tip was then cooled to 50°K and redosed. The work function plot, as determined by the single point technique, is shown in Figure 37. The field emission patterns are shown in Figures 38, 39 and 40. The decrease in work function between 100-200°K is possibly due to a surface rearrangement. The plateau between 200°K and 500°K suggests that acetylene is associatively chemisorbed over this temperature interval. The nearly linear increase in work function

between 500-800°K would then be due to the decomposition reaction,

$$C_2H_2 \rightarrow C_2 + 2H$$
$$2H \xrightarrow{\text{fast}} H_2(g) \qquad (56)$$

the desorption of hydrogen being fast. Evaluating $\Delta H_o'$ as before, $\Delta H_o'$ equals 44 kcal/mole assuming the α_{C_2} given previously. This is greater than the value of 39 kcal/mole obtained for the clean surface.

Decomposition of ethylene

Figures 41 - 45 show the emission patterns from tungsten covered with adsorbed ethylene. The experiments were conducted in the same way as those for acetylene.

The change in work function with flash temperature is shown in Figure 46. The decomposition of ethylene is clearly a two step process. At temperatures below 200°K, the work function is constant, indicating that ethylene chemisorption is associative at these temperatures. The following sequence of reactions accounts for the behavior of the work function plot.

1. 200-300°K $\quad {}^{*}C_2H_4 \rightarrow 2H + {}^{*}C_2H_2{}^{*}$
2. 300-450°K $\quad {}^{*}C_2H_2{}^{*} \rightarrow 2H + C_2$
3. 450-700°K $\quad {}^{*}C_2H_2{}^{*} \rightarrow 2H + C_2$

$$2H \xrightarrow{\text{fast}} H_2(g) \qquad (57)$$

The stars, *, represent metal sites and are placed to distinguish between "cis" and "trans" adsorption.

Step 1 is apparently nearly complete by 300°K since the work function change with temperature is tending to zero as 300°K is approached. The acetylenic residues, which must be on radically different sites than acetylene itself would occupy, nevertheless, decompose over nearly the same temperature range as acetylene (300-700°K). The work function goes through a maximum at 500°K instead of just a change in slope, as was the case for acetylene, because of the greater amount of hydrogen on the surface. Both the hydrogen desorption and decomposition reactions are apparently complete by 700°K and the work function remains constant over the interval 725-850°K. Above 850°K, the work function decreases again, probably due to a surface rearrangement or diffusion of carbon into the bulk of the tungsten.

Some of the pattern changes observed can be interpreted in light of the sequence of reactions previously proposed. Between 100-200°K, the pattern changes very little. Above 200°K, the first darkening (indicative of an increase in work function) is in the area of the 111 planes where it was previously proposed that the site density was high. By 275-300°K, the areas around the 110 planes are emitting in a manner somewhat reminiscent of acetylene patterns at those temperatures. The 400°K patterns for both acetylene, Figure 29a, and ethylene, Figure 42f, are very similar which tends to support the proposed reaction

sequence for ethylene. Above 500°K, however, the difference in patterns for the two gases is considerable. This is not too surprising since it has already been proposed that the two gases occupy very different types of sites.

The images for the 800°K and above flashes show the characteristic crystallites that appear for carbon on most metals (3, 30). The rings around the 110 plane are not due to a decrease in work function but to an increase in local field strength on the sharp edged lattice steps. A field ion examination revealed the steps to be in the order of 10-20Å in height (30).

A comparison of the work function as determined by both single point and Fowler-Nordheim techniques is also shown in Figure 46. Below 100°K, physically adsorbed ethylene is present on the surface and behaves as a polarizable, dielectric layer. As was the case for acetylene, the presence of the physically adsorbed layer did not affect the Fowler-Nordheim determination of the work function. Above 425°K, the single point determination yields too low a value for the work function. This result is extremely interesting since the modifications of the Fowler-Nordheim theory to account for polarizability and dielectric properties of an adsorbed layer, as previously discussed, will always lead to a single point technique work function which is too high rather than too low. Metallic adsorbates, which lower the work function, have been known

to enhance the emission current above that expected from the work function change (14) and indeed, if the positive ion core behaved as an attractive square well, the emission current would be given by equation 30. Carbon, however, is an electronegative adsorbate, and, as such it is not clear how it could constitute an attractive potential well.

The 0.5 ev increase in work function for the carbon residue on the tip is in disagreement with Klein, who reported that carbon increases the work function only slightly (31). However, Klein determined the work function by the single point technique and apparently at lower carbon concentrations, and it is therefore likely to be in error.

The comparison of the two methods of determining the work function as shown in Figure 47 yields

$$\Delta\Phi_{F.N.} = 1.10\ \Delta\Phi_{S.P.} - .15 \qquad (58)$$

for temperatures up to 400°K. Above 400°K, it is clear that no simple relationship exists between $\Delta\Phi_{F.N.}$ and $\Delta\Phi_{S.P.}$.

The change in the pre-exponential of the Fowler-Nordheim equation is shown in Figure 48. The decrease in - log A between 75 and 100°K results from the desorption of the physically adsorbed ethylene. This clearly illustrates that the pre-exponential was responsible for the difference between $\Delta\Phi_{F.N.}$ and $\Delta\Phi_{S.P.}$ at this temperature. The pre-exponential starts to decrease as the decomposition of ethylene begins (at 200°K) but does not appear to be sensitive to the sequence of

reaction steps occurring on the surface. It is confirmed from this data that carbon does increase the pre-exponential. The change in the log of the pre-exponent of 0.5 means that the current is three times as great as would be expected from work function changes alone.

The decomposition of ethylene on a tungsten-carbon surface was also studied. The work function data, determined by Fowler-Nordheim evaluations, is shown in Figure 49. The images are shown in Figures 50 and 51. The tungsten-carbon surface was prepared by dosing a clean tungsten surface with ethylene, heating to 1000°K for 30 sec and redosing it 50°K. The work function data indicates that a surface reaction is occurring in the temperature interval 100-300°K in contrast to ethylene on clean tungsten which did not start to dissociate until temperatures in the order of 200°K. The linearity of the work function plot between 350° and 750°K suggests the hydrogen desorption from the surface is fast and the rate limiting step in the dissociation is the decomposition reaction. The following steps are proposed to account for the shape of the curve.

1. 100°-300°K $C_2H_4 \rightarrow C_2H_2 + 2H$
2. 300°-375°K $C_2H_4 \rightarrow C_2H_2 + 2H$
   $2H \rightarrow H_2(g)$
3. 375°-750°K $C_2H_2 \rightarrow C_2 + 2H$
   $2H \xrightarrow{fast} H_2(g)$

The evident early decomposition of ethylene on the carbon-tungsten surface is very interesting when compared to acetylene decomposition which was inhibited by the presence of carbon. This can not be accounted for by the "work function effect" since the decomposition reaction always results in an increase in total work function. Apparently the carbon residue on the surface is still blocking the most favorable sites for ethylene chemisorption so that the adsorbed ethylenic species are in a strained configuration. Too little is known about the state of the surface to speculate further on this point.

DISCUSSION

It is worthwhile to compare the results obtained on tungsten with those obtained on iridium (3). The work function data for hydrogen, acetylene, and ethylene on tungsten and iridium are summarized in Figure 52. It is apparent that the only major difference between the work function plots for the two metals results from the presence of hydrogen on the tungsten surface at temperatures below 450°K. The heat of desorption of hydrogen on tungsten, ΔH°_{o}, equals 35 kcal/mole, and for iridium, 24 kcal/mole (32). As a result, the rate determining step in the dissociation of ethylene on iridium above 300°K is the rupture of C-H bonds and not the desorption of hydrogen from the surface. This is true for tungsten only above 550°K.

The activation enthalpy for the dissociation of acetylene, as determined by equation 46, is nearly the same for both metals, 50 kcal/mole on tungsten and 48 kcal/mole on iridium.

The activation enthalpy for the first step of the dissociation of ethylene on both metals can only be crudely estimated but it appears to be in the order of 20 kcal/mole for both metals since the reaction is nearly complete by 300°K.

Diffusion experiments such as those performed on tungsten were not carried out on iridium; thus, those results can not be compared. It

was established that chemisorbed acetylene and ethylene were not mobile on iridium which agreed with the tungsten results.

Although it was not possible to study the hydrogenation reactions of ethylene in the present apparatus, this work does provide information on the surface species that are likely to contribute to that reaction. The general features of the hydrogenation of ethylene were discussed earlier. In addition, there is reasonable agreement in the literature on the following points:

1. The heat of adsorption of ethylene on tungsten varies from 100 to 20 kcal/mole and on nickel from 60 to 23 kcal/mole (7). The larger value refers to the heat of adsorption on a clean surface and the smaller value is the heat of adsorption on a nearly covered surface.

2. The heat of adsorption of hydrogen varies from 35 to 10 kcal/mole on tungsten (32) and 30 to 15 kcal/mole on nickel (7).

3. The activation energy for the hydrogenation of ethylene on Rh, Ni, Pd, Pt, Co, and Fe is 10.7 kcal/mole (9). For W and Ta it is 2.4 kcal/mole (7).

4. The variation in rate constant, k, with lattice constants (9) is shown in Figure 53. It is interesting that tungsten is 10^4 times less active than rhodium although the activation energy is less on tungsten.

5. Oriented 110 films of nickel are five to ten times more active than non-oriented nickel films (9).

6. When ethylene is admitted to a film, it is rapidly adsorbed. No ethane appears in the gas phase until the surface is saturated with ethylene (21) (approximately 25% of the hydrogen monolayer capacity).

7. If ethylene and hydrogen are admitted separately, the initial rate of hydrogenation depends on the order of addition of reactants (9, 21). The initial rates are ordered as follows:

Hydrogen admitted first > Simultaneous addition > Ethylene admitted first.

At later times, the reaction rates for the different modes of addition become equal.

8. When ethylene and hydrogen are admitted together, the reaction rate may be expressed as (9)

$$\frac{dP_{C_2H_2}}{dt} = kP_{H_2}^{1}P_{C_2H_4}^{0} \qquad (60)$$

9. The reaction of ethylene at very low pressures with pre-adsorbed hydrogen at 194°K is practically instantaneous. The self-hydrogenation of ethylene does not occur at this temperature (7).

10. Acetylene does not hydrogenate on tungsten, but the hydrogenation does take place on face-centered cubic metals (7).

The rate of hydrogenation of acetylene is usually about 10^{-3} that for ethylene hydrogenation.

11. When acetylene undergoes hydrogenation on the face-centered cubic metals, ethylene appears in the gas phase; however, there is no evidence that the adsorption of ethylene itself can occur reversibly (22).

12. Body-centered cubic metals tend to become less active as the hydrogenation reaction proceeds (7). For tungsten, the initial rate is at least ten times faster than the final rate.

13. If acetylene is pre-adsorbed on a metal surface, the hydrogenation reaction of ethylene does not occur (7).

There have been a number of mechanisms proposed for the hydrogenation of ethylene (20, 21, 22). In general, they fall into two basic types, neglecting intermediate steps:

Mechanism I: Ethane is formed by the reaction of chemisorbed ethylene with chemisorbed hydrogen

Mechanism II: Ethane is formed by the reaction of gaseous ethylene with chemisorbed hydrogen.

The normal procedure has been to suggest a series of surface reactions with rate constants for each step of the reaction, make appropriate steady state assumptions, and show that the resulting rate expression has the form of equation 60. Proponents of each of

the many mechanisms have found short range arguments to support their viewpoints, but no mechanism has been proposed that adequately accounts for the hydrogenation reaction in a comprehensive way. Indeed, all treatments of this type have neglected the dependence of activation energy on surface composition and coverage, and it is easy to see from the magnitudes of variation already quoted that such neglect is totally unjustified. It has already been shown that it is rarely possible to determine unambiguously the order of a reaction, n, ν_n, ΔH_o or α.

Flash filament experiments have demonstrated that Type I mechanisms are not important for ethylene hydrogenation reactions. Hansen, et al. (33) determined that, when adsorbed ethylene on iridium is not in equilibrium with the vapor, ethane is not produced in the gas phase regardless of filament temperature. Roberts (34), dosing iridium films at 300°K with ethylene, found that ethane was produced rapidly. Roberts dosing conditions were such that the rate of impact of ethylene with the surface was 10^5 times as great as those in the experiments of Hansen, et al. The conclusion to be reached is that iridium can hydrogenate ethylene in equilibrium experiments, therefore failure to observe ethane in flash filament studies implies that Type I mechanisms can not account for major steps in the reaction.

Both mechanisms I and II are subject to the criticism that they

fail to account for the remarkable consistancy in activation energy for the hydrogenation reaction, regardless of the metal catalyst. In view of the rather large variation in heats of adsorption of hydrogen and ethylene for the different metals it is surprising that the activation energy is constant for hydrogenation.

Mechanism II also fails in view of "fact 6". For both tungsten and iridium, the evidence is that the adsorption of ethylene occurs dissociatively and that hydrogen is a dissociation product. Yet it is observed that no ethane appears in the gas phase until the surface is saturated with ethylene.

Neither mechanism I nor II accounts for the greater activity of 110 oriented nickel films nor the fact that rhodium is 10^4 times as active as tungsten.

On the basis of the field emission evidence, it is possible to suggest a new mechanism that adequately accounts for the hydrogenation reactions of ethylene. The reaction scheme is as follows:

$$
\begin{aligned}
&1.\ C_2H_4\ (g) \rightarrow \overset{*}{C_2H_4}\\
&2.\ \overset{*}{C_2H_4} \rightleftarrows *C_2H_2* + 2\overset{*}{H}\\
&3.\ C_2H_4\ (g) + \overset{*}{C_2H_4} \rightarrow C_2H_6\ (g) + *C_2H_2*\\
&4.\ H_2\ (g) + *C_2H_2* \rightarrow \overset{*}{C_2H_4}\\
&5.\ *C_2H_2* \rightarrow 2\overset{*}{C}H \text{ or } \underset{*}{C_2}\underset{*}{H_2} \text{ or } \underset{**}{C_2} + 2\overset{*}{H}
\end{aligned}
\qquad (61)
$$

As before, the stars, *, represent metal sites and are placed to distinguish between "cis" and "trans" species. The symbol $C_{2}\ H_{2}$ is meant to describe a chemisorbed species differing from the acetylenic residue $*C_2H_2*$. Both species will be described in greater detail later.

Ethylene initially chemisorbs on the surface and dissociates to an acetylenic residue and hydrogen. As a consequence of the variation in activation enthalpy for the dissociation reaction, the addition of more ethylene to the surface results in a quasi- equilibrium with undissociated ethylene existing on the surface when the activation enthalpy become prohibitively high for the dissociation. Then associatively chemisorbed ethylene exists on the surface as a dipole with the positive end away from the surface. The hydrogenation reaction results from the addition of hydrogen from the acidic surface ethylene to the basic gaseous ethylene producing ethane, step 3. The slow step in the hydrogenation process is the production of surface ethylenic species by step 4. The surface becomes poisoned by the irreversible reaction expressed by step 5.

The source of hydrogen for the hydrogenation of the gaseous ethylene is then the surface ethylenic species and not the metal. Referring to Figure 24, when ethylene is chemisorbed "trans", two hydrogen atoms point away from the surface and the other two lie in

a plane parallel to the surface. The former hydrogen pair would then be involved in the hydrogenation reaction. The envisioned activated complex is shown in Figure 54a. The evidence is that ethylene always lowers the work function of a metal (i.e. electrons are withdrawn from the ethylene molecule to the metal). One might expect a weakening of the C-H bond on this basis.

The activated complex for the formation of the ethylenic species from the "cis" acetylenic species is depicted in Figure 54b. The low activation energy of 10.7 kcal/mole for most metals for this step probably results from the acetylenic species being in a strained configuration across the 4.47Å spacing. From this model one would also suspect that the activation energy would be roughly independent of the metal since this step does not involve the making or breaking of surface bonds. This model also accounts for the observed order of the reaction since the rate of production of the "trans" ethylenic species is proportional to the rate of arrival of hydrogen gas at the surface. Therefore

$$\frac{dP_{C_2H_6}}{dt} = kP^1_{H_2} \qquad (62)$$

It is now of interest to inquire as to the fate of the acetylenic residue produced by steps 2 and 3. It is clear, that on tungsten, the acetylenic residue is left on a site where the tungsten-tungsten distance is 4.47Å which undoubtedly puts strain on the carbon-metal

bonds and carbon-carbon bonds. The most favorable tungsten-tungsten distance (calculated from geometric considerations) was found to be 3.4Å. There are two possibilities for the dissociation of the acetylenic residues and these are expressed in step 5. Either the carbon-carbon bond breaks, forming C-H species, or one carbon-metal bond breaks and reforms on one of the 2.74 or 3.16Å spacings available. Either process would be irreversible and would lead to a reduction of sites formerly available for the ethylenic species. For the face-centered cubic metals the metal-metal distance is not as great as tungsten; therefore, the reaction expressed by equation 5 would be slower.

It was found that 110 oriented nickel films were five to ten times as active as non-oriented nickel films. The 110 plane of a face-centered cubic metal is shown in Figure 55. It is very similar to the 112 plane of a body centered cubic metal and contains the greatest density of sites for ethylene adsorption. It is not surprising then that the 110 oriented nickel is more active since the adsorbed ethylene concentration is highest there.

The model proposed accounts for "fact" 7. If hydrogen were pre-adsorbed on the metal, two effects would insure that the initial chemisorption of ethylene would be associative. First, concentration effects would drive the equilibrium of step 2 to the associative species,

and second, the "work function effect" favors associatively chemisorbed ethylene. In addition, the presence of hydrogen may inhibit the reaction expressed by step 5.

The pre-adsorption of acetylene inhibits the hydrogenation reaction because it drastically reduces the number of sites available for ethylene chemisorption. The heat of adsorption of acetylene on metals is higher than that for ethylene, therefore ethylene can not displace adsorbed acetylene. This suggests an experiment which might give support to the proposed hydrogenation mechanism. From the field emission results for the decomposition of acetylene on tungsten, it was determined that hydrogen and acetylene can exist on the surface below temperatures of 450°K. Therefore, if one were to preadsorb both hydrogen and acetylene on a tungsten surface and then admit ethylene, the hydrogenation reaction should not occur on the basis of the proposed mechanism since there are no ethylene species on the surface. If the reaction did occur, it would indicate that the adsorbed hydrogen on the surface was the source of hydrogen for the hydrogenation process.

The observation that gaseous ethylene is produced by the hydrogenation of acetylene on face-centered cubic metals although the chemisorption of ethylene is irreversible has puzzled a number of investigators. (See, for example, references (2) and (22)). In light of the surface diffusion experiments, which revealed that ethylene

did not chemisorb "cis", it is apparent that the ethylene formed from a "cis" acetylenic species (which chemisorbed on the short spacings) will be in a state of high potential energy and desorb.

It would appear that only "point 9" is at variance with the proposed mechanism. Beeck(7) felt that this experimental fact, which was determined only for a nickel catalyst, supported Type II mechanisms. It should be noted however, that ethylene chemisorption on another face-centered cubic metal, iridium, was dissociative even at this low temperature and one would guess that ethylene would dissociatively adsorb on nickel at 194°K also. In addition, pressures in Beeck's apparatus were determined by mercury manometers; it is doubtful that the small amount of ethane formed as predicted by the proposed mechanism could have been detected by Beeck.

The proposed mechanism is further supported by exchange experiments with ethylene and deuterium over nickel catalysts. Turkevich et al. (35) found that, in spite of pretreating the catalyst with deuterium, when ethylene and deuterium were admitted the first ethane evolved was C_2H_6 closely followed by C_2H_5D and to a lesser extent, $C_2H_4D_2$. Later $C_2H_3D_3$, $C_2H_2D_4$, C_2HD_5 and C_2D_6 were observed; the C_2D_6 appeared only after the reaction was 70% complete. In addition, considerable ethylene exchange was observed with C_2H_3D the predominant product at first but $C_2H_2D_2$,

C_2HD_3 and C_2D_4 appeared later in that order. Eventually all species were consumed by the hydrogenation.

The speculation was made that hydrogen added during the hydrogenation reaction must have come from another ethylene molecule, but no hydrogenation mechanism was proposed. The proposed mechanism given in equation 61 accounts for the initial product of C_2H_6. Also, the addition of deuterium to the acetylenic species, step 4 of equation 61, results in an ethylenic species with either two hydrogen atoms, or one hydrogen atom and one deuterium atom, or two deuterium atoms pointing up from the surface. Therefore the appearance C_2H_6, C_2H_5D and $C_2H_4D_2$ can be accounted for with no modifications of the mechanism. To account for the appearance of the higher substituted ethane molecules, it is only necessary to account for the appearance of the substituted ethylene molecules since once these species exist, all the substituted ethane molecules can occur.

Since ethylene chemisorption is irreversible, the exchange of ethylene must not result from a surface reaction between chemisorbed ethylene and deuterium but rather from gaseous ethylene and a deuterium source on the surface. The simplest model is to assume that not all gaseous ethylene collisions with chemisorbed ethylene result in hydrogenation, but that some collisions result in exchange of hydrogen. It is reasonable to suppose that not all collisions result

in the activated complex shown in Figure 54a. It also may be that exchange can occur by a reaction with the hydrogen or deuterium on the surface.

It should be noted that the proposed mechanism may not be applicable to other olefinic hydrogenation reactions. For example, cyclohexene, which can be hydrogenated over these same metal catalysts, most certainly would not hydrogenate by the scheme presented here. Type I mechanisms would be more likely to account for that reaction.

SUMMARY

The chemisorption and surface reactions of acetylene and ethylene on a tungsten surface were studied by field electron emission microscopy techniques. These investigations were conducted in a liquid helium cryostat so that the surface reactions could be studied from 4°K to higher temperatures under ultra-high vacuum conditions.

Acetylene reacted with a clean surface in the following manner:

1. Between 100° and 300°K, acetylene chemisorbed associatively.
2. Between 300° and 450°K, the chemisorbed acetylene decomposed to yield adsorbed hydrogen and a carbon residue.
3. Above 450°K, the adsorbed hydrogen desorbed at a rate comparable to the decomposition reaction.
4. Above 600°K, the desorption of hydrogen was fast compared to the decomposition reaction.
5. The decomposition reaction was complete by 725°K leaving a carbon residue on the surface.

The activation enthalpy for the dissociation reaction was found to be coverage dependent, and given by $\Delta H = 50$ kcal/mole $-23\,\theta$ kcal/mole monolayer.

From the work function data, the relative surface concentrations of the carbon residues, hydrogen, and acetylene were obtained as a

function of temperature.

The decomposition reaction of acetylene on a carbon-tungsten surface was studied and found to differ from those on the clean surface. On the carbon-tungsten surface, acetylene remained in a associative state at temperatures up to 500°K. Between 500° and 800°K, the chemisorbed acetylene decomposed, producing hydrogen,which desorbed rapidly, and a carbon residue. By 800°K, the reaction was complete.

Ethylene reacted with tungsten in the following manner:

1. Between 100° and 200°K, ethylene chemisorbed associatively on the surface.

2. Between 200° and 300°K, ethylene decomposed to yield a acetylenic residue and adsorbed hydrogen.

3. Between 300° and 450°K, the acetylenic residue decomposed to yield adsorbed hydrogen and a carbon residue.

4. Above 450°K, the desorption of the surface hydrogen proceeded at a rate comparable to the dissociation reaction.

5. By 700°, the decomposition reaction was complete, leaving a carbon residue on the surface.

The decomposition of ethylene on a carbon-tungsten surface was also studied. Ethylene dissociated to adsorbed hydrogen and an acetylenic residue in the temperature interval 100° to 300°K. Between 375° and 750°K, the acetylenic residues decomposed to gaseous hydrogen and a carbon residue.

From shadowing experiments, it was confirmed the chemisorbed acetylene and ethylene are immobile. However, at temperatures between 70°K and 100°K, Type I diffusion was observed and offered some interesting insights to the mode of chemisorption of these hydrocarbons. It was deduced that acetylene chemisorbs "cis", with the tungsten and carbon atoms coplaner, on the short 2.74Å and 3.16Å spacings available on a tungsten lattice. Ethylene was found to chemisorb on the long 4.47Å spacings available principally on the 112 and 111 planes of tungsten. It was proposed that ethylene chemisorbed "trans" to accommodate the long spacing. This novel bonding mode was found to account for a number of surface reactions involving ethylene that were not previously understood.

From a knowledge of the surface species of ethylene and acetylene as a function of temperature and the mode of chemisorption of the two gases, a new reaction mechanism for the hydrogenation of ethylene was proposed as follows:

1. $C_2H_4(g) \rightarrow {}^{*}_{*}C_2H_4$
2. ${}^{*}_{*}C_2H_4 \rightarrow {}^{*}_{*}C_2H_2{}^{*}_{*} + 2{}^{*}_{*}H$
3. $C_2H_4(g) + {}^{*}_{*}C_2H_4 \rightarrow C_2H_6(g) + {}^{*}_{*}C_2H_2{}^{*}_{*}$
4. $H_2(g) + {}^{*}_{*}C_2H_2{}^{*}_{*} \rightarrow {}^{*}_{*}C_2H_4{}^{*}_{*}$
5. ${}^{*}_{*}C_2H_2{}^{*}_{*} \rightarrow {}^{*}_{*}C_2{}^{*}_{*} + 2{}^{*}_{*}H$

This mechanism accounts in a comprehensive way for a variety of observations from exchange experiments and volumetric studies of the

reaction.

It is apparent the variation of rate constants of surface reactions can be very dependent on the crystallographic orientation of the surface. The field electron emission microscope should play an increasingly important role in the elucidation of surface processes.

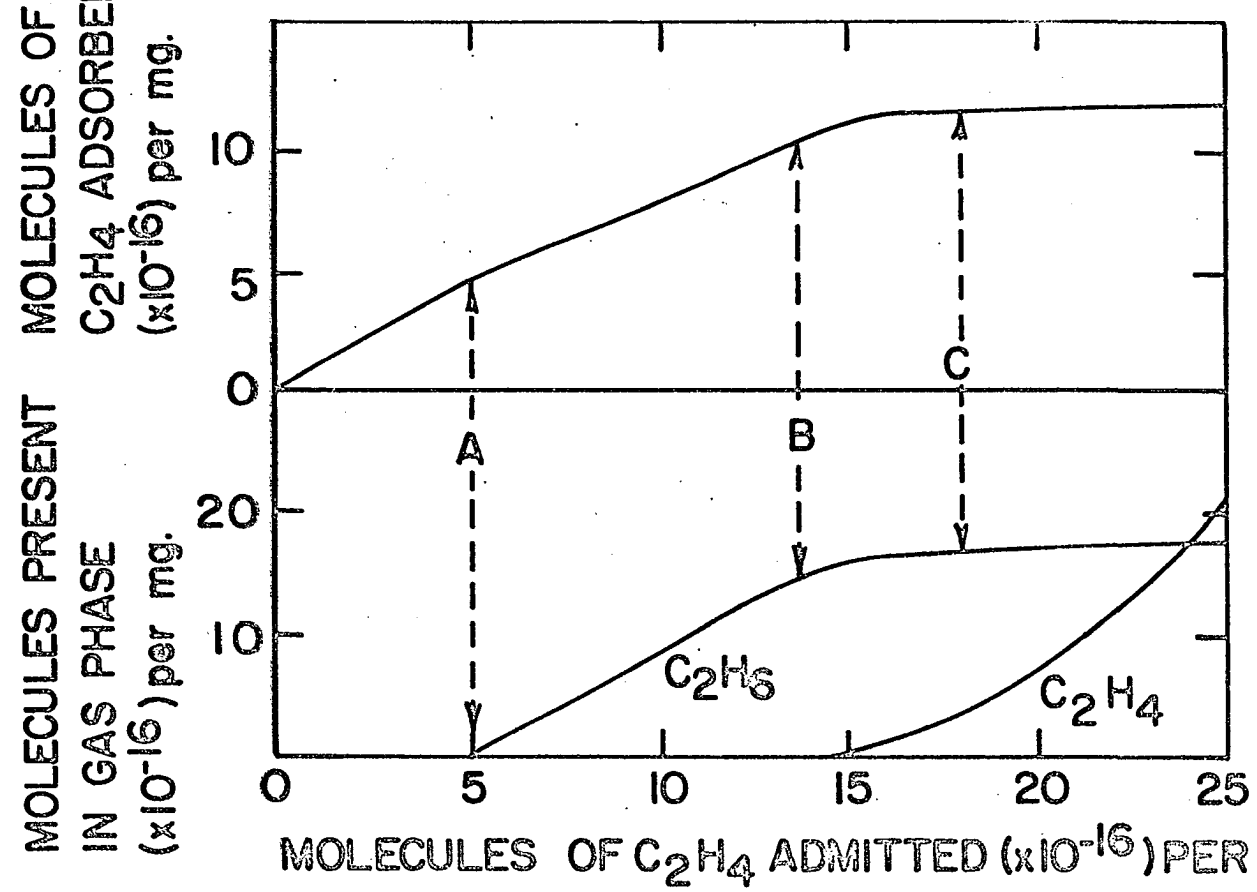

Figure 1. The chemisorption of ethylene on evaporated metal films. (The shape of the curves are common for ethylene chemisorption on nickel and tunsten, the scales relate to nickel.)

Figure 2. Field electron emission microscope. Electrons travel radially to the fluorescent screen producing a magnified image of the tip.

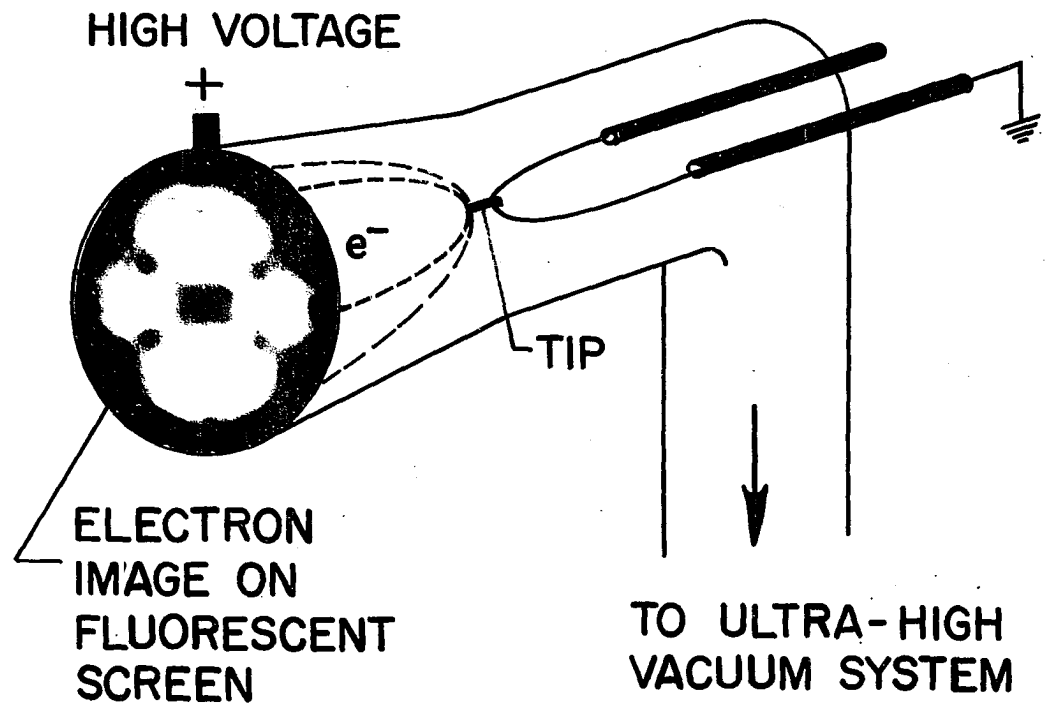
HIGH VOLTAGE
+
e⁻
TIP
ELECTRON
IMAGE ON
FLUORESCENT
SCREEN
TO ULTRA-HIGH
VACUUM SYSTEM

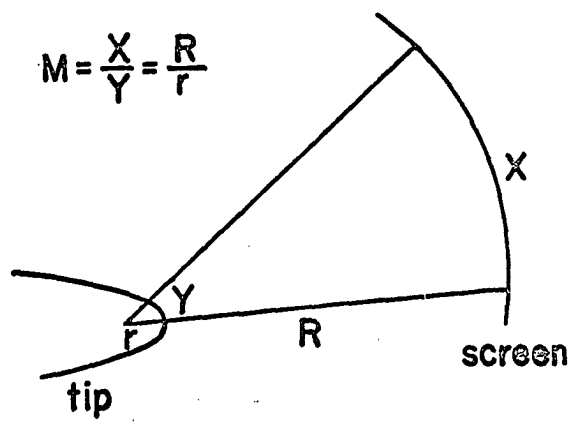

Figure 3. Schematic diagram showing that the magnification, M, is the ratio of the tip to screen distance, R, to tip radius, r.

Figure 4. Field electron image of a clean tungsten tip indexed crystallographically.

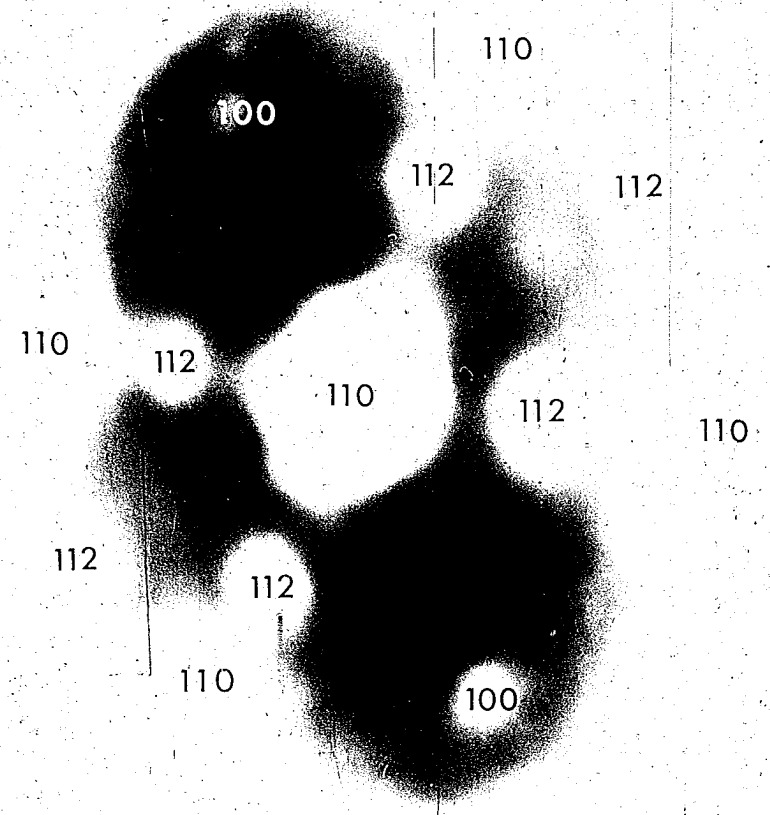
110
100
112
112
110
112
110
112
110
112
112
110
100

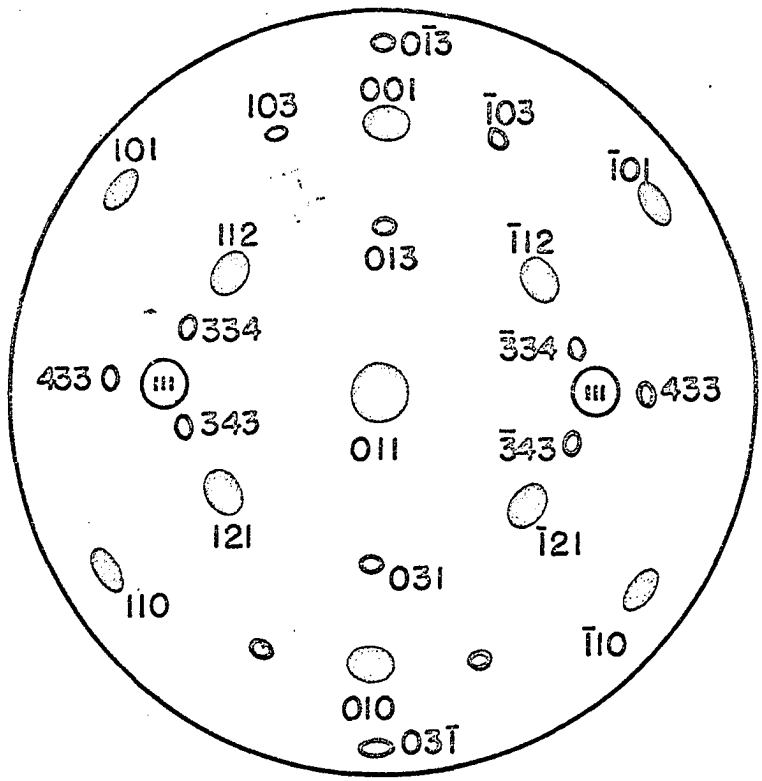

Figure 5. Orthographic projection of a hemispherical cubic crystal oriented with 110 plane in the axis.

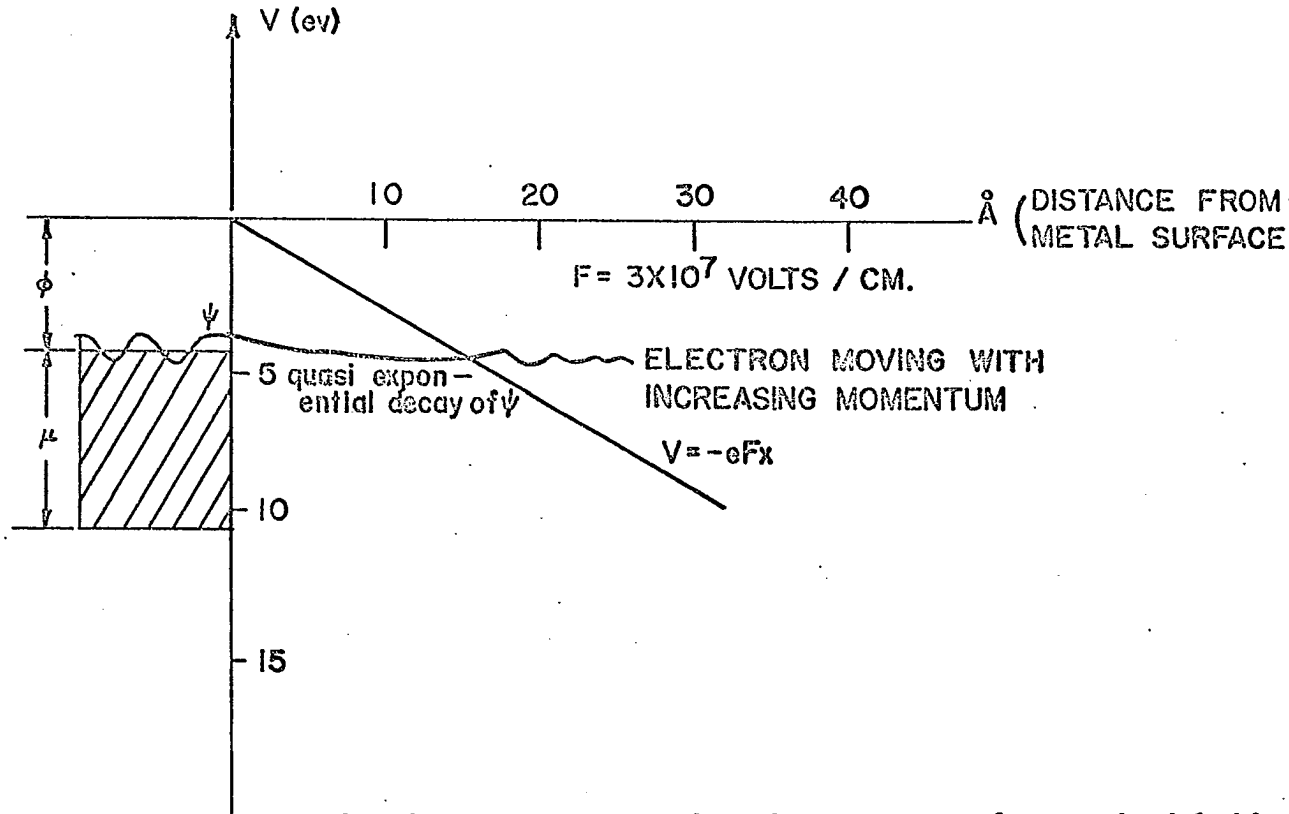

Figure 6. Potential energy diagram for electrons in a metal in the presence of an applied field. The electron wave, ψ, is represented schematically as a standing wave in the potential well, undergoing quasi-exponential decay as the electron penetrates the barrier, and decreasing in wave length as the electron saves the barrier region with increasing momentum.

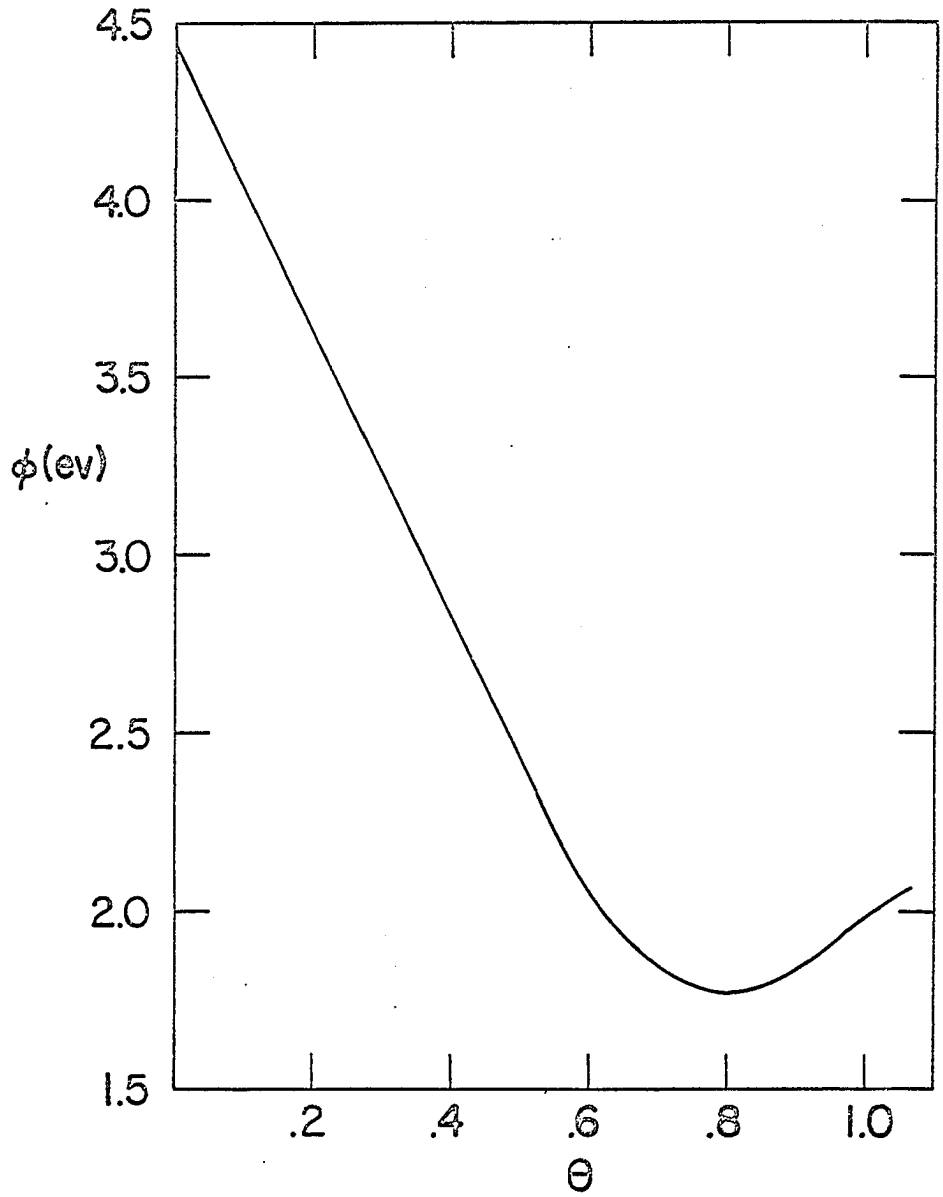

Figure 7. Work function change for the adsorption of potassium on tungsten.

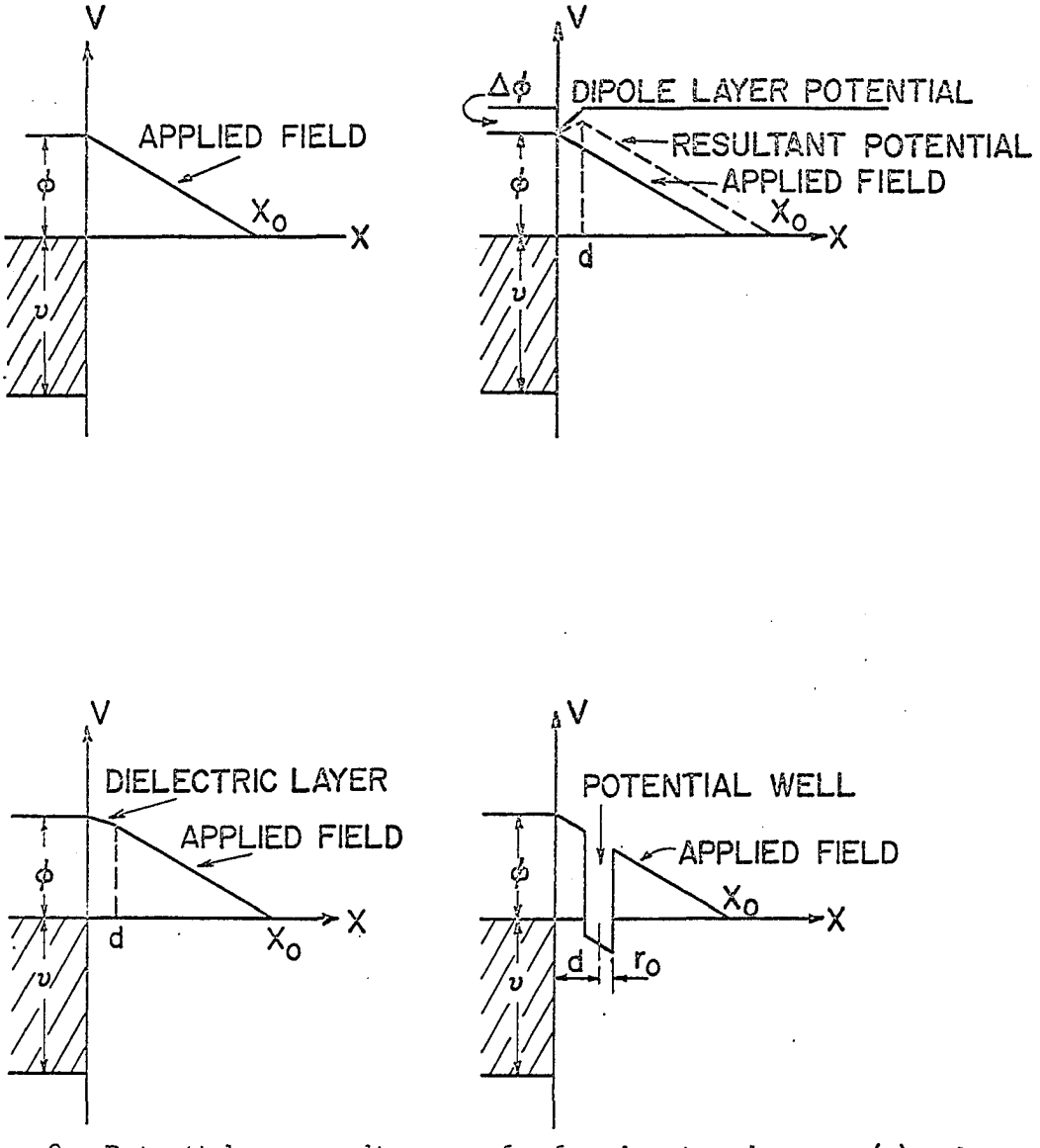

Figure 8. Potential energy diagrams for four barrier shapes: (a), clean surface; (b) adsorption of dipole layer on the surface; (c), adsorption of dielectric layer to surface; (d) addition of deeply attractive potential well.

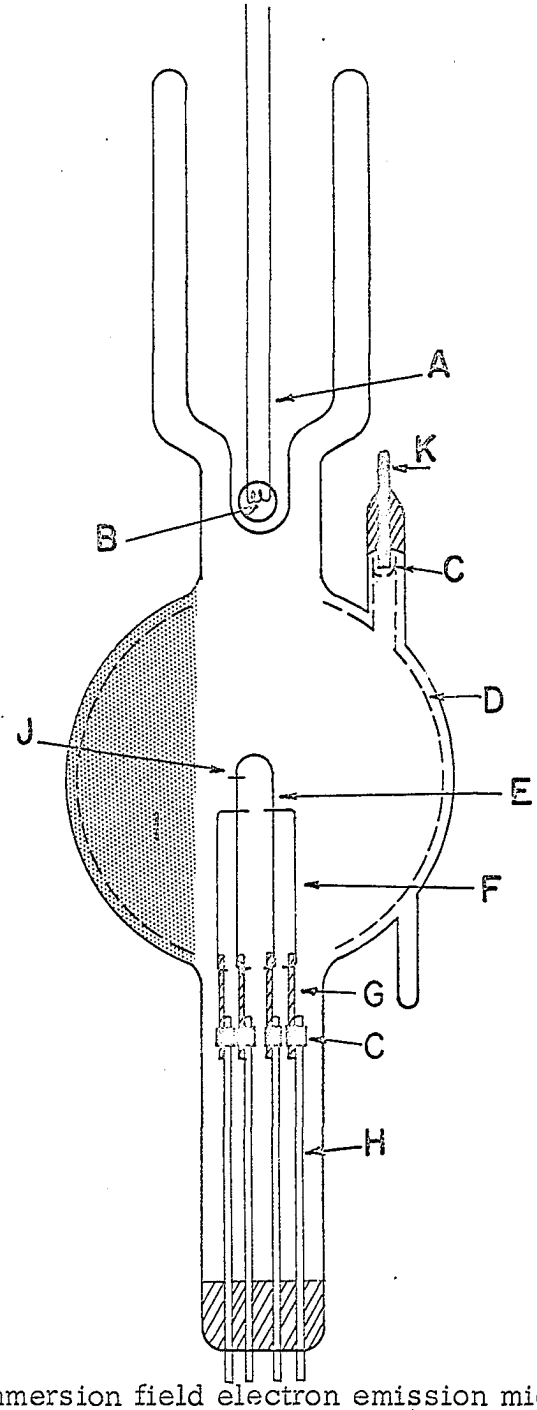

Figure 9. Total immersion field electron emission microscope: A. nichrome heater; B, ball of Sauereisen cement; C, platinum strip intermediates between nichrome and tungsten to tungsten wells; D, tin oxide conductive coating; E, metal filament; F, potential sensing leads; G, nichrome insert; H, tungsten rods; I, phosphor screen; J, tip; K, high voltage lead-in.

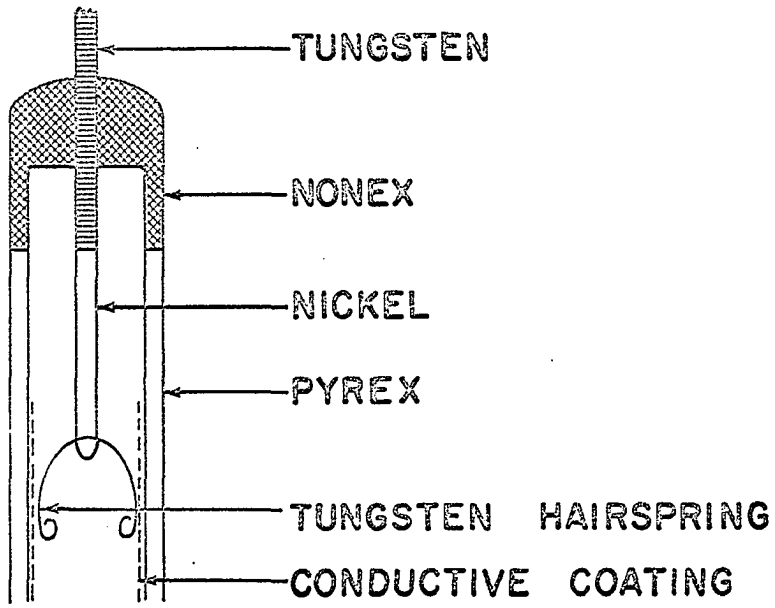

Figure 10. Diagram showing construction of the hairspring contact to the conductive coating.

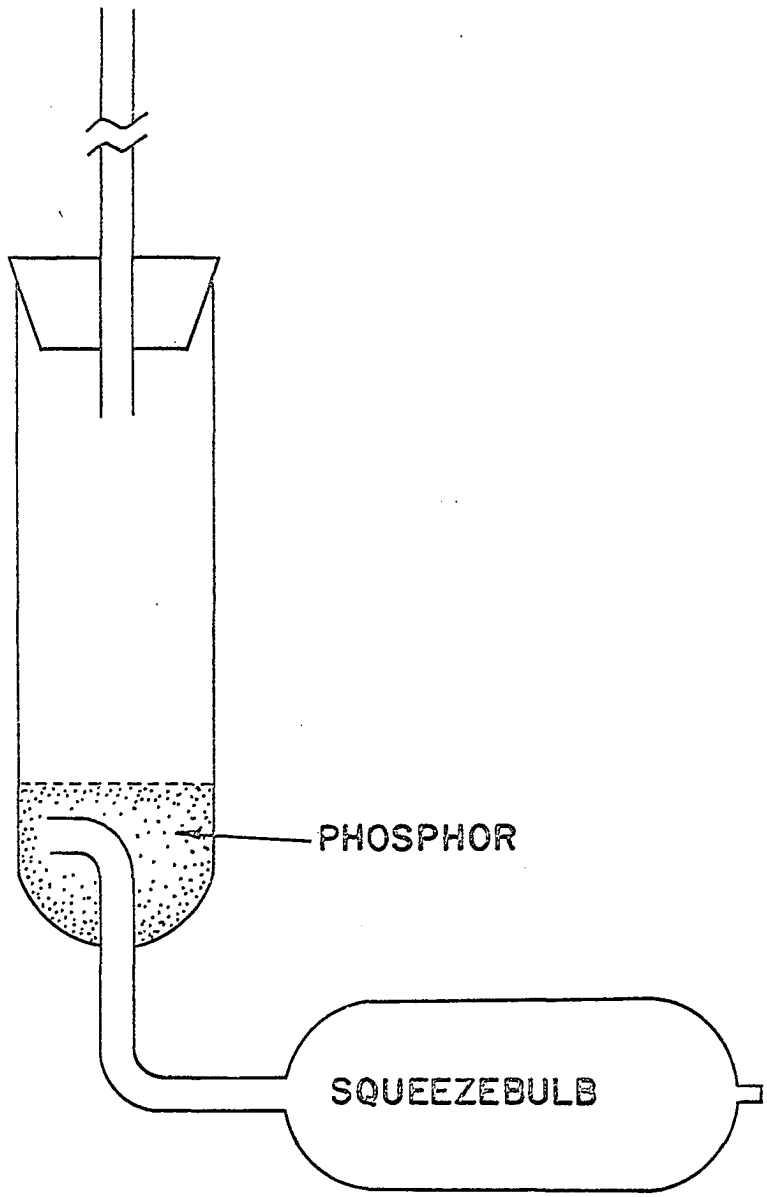

Figure 11. Diagram of the phosphor puffer for screen deposition.

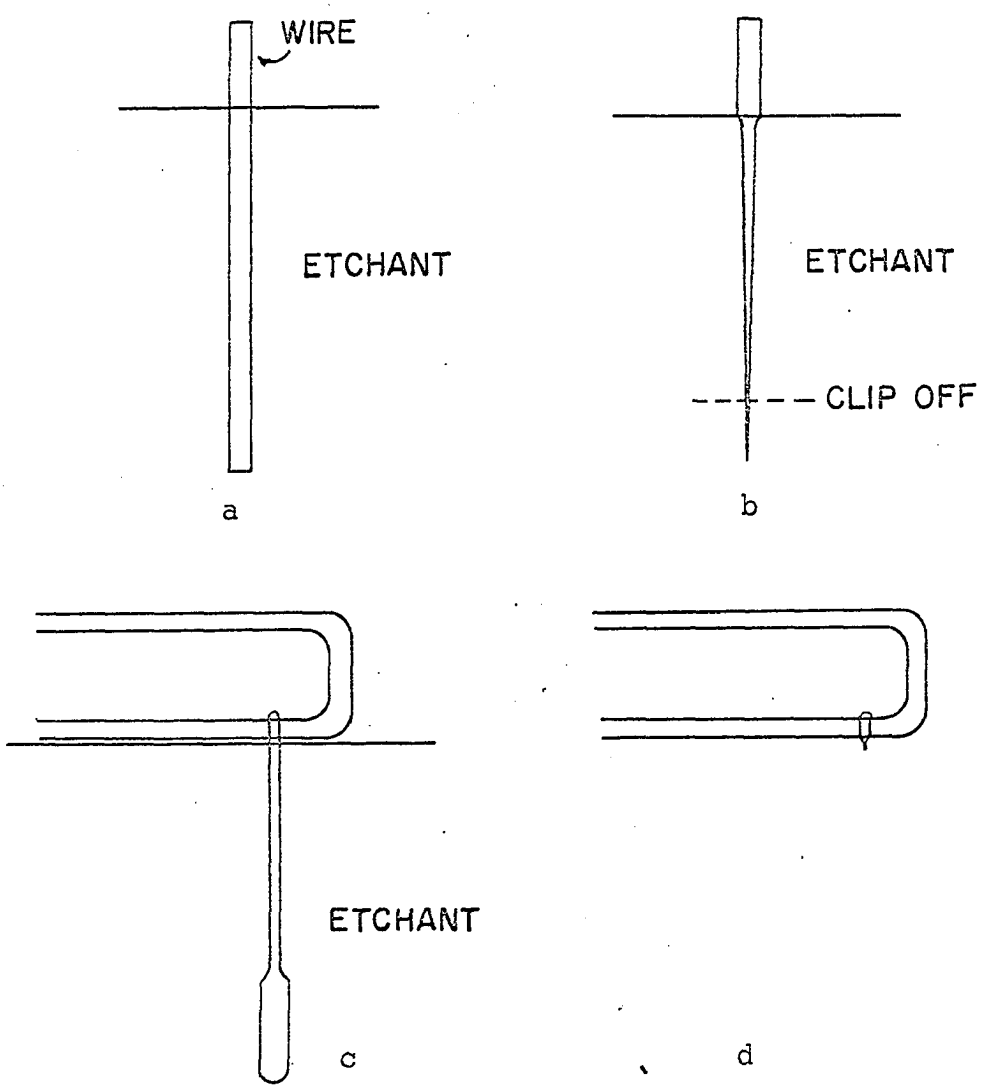

Figure 12. Field emission tip etching procedure. (a), The wire is immersed in the etchant and etched until it is sharply pointed. (b), The sharp end is clipped off and spot-welded to the filament. The assembly is nearly completely immersed so that the tip length will be short, (c). The result is shown in (d) with the actual tip size exaggerated.

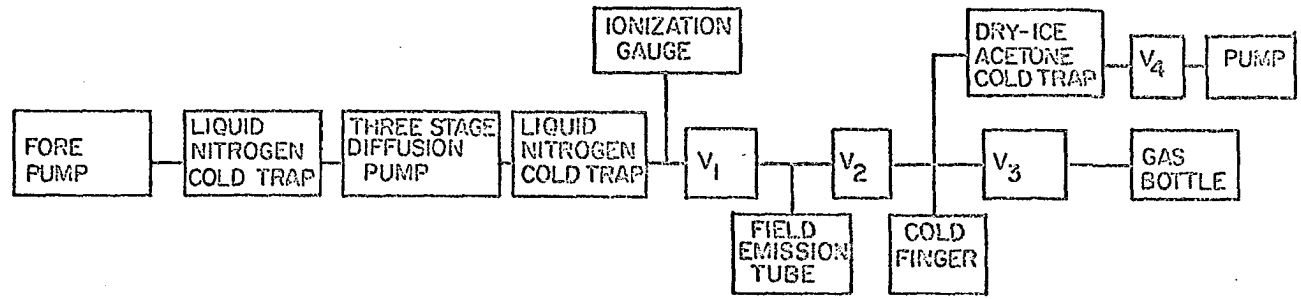

Figure 13. Block diagram of vacuum system. Area between the three stage diffusion pump and value V_2 can be baked to 400°C by a portable oven.

Figure 14. Diagram of cryostat for total immersion tube: A. transfer tube inlet; B, high voltage lead sealed in evacuated glass tube; C, port to pump and pop-off valve; D, stopcock of inner dewar jacket; E, press eal making electrical contact to silvering on inner dewar; F, rubber sleeve; G, windows; H, liquid nitrogen inlet (vent not shown); I, electrical lead-in; J, pipe flange; K, rubber O-ring.

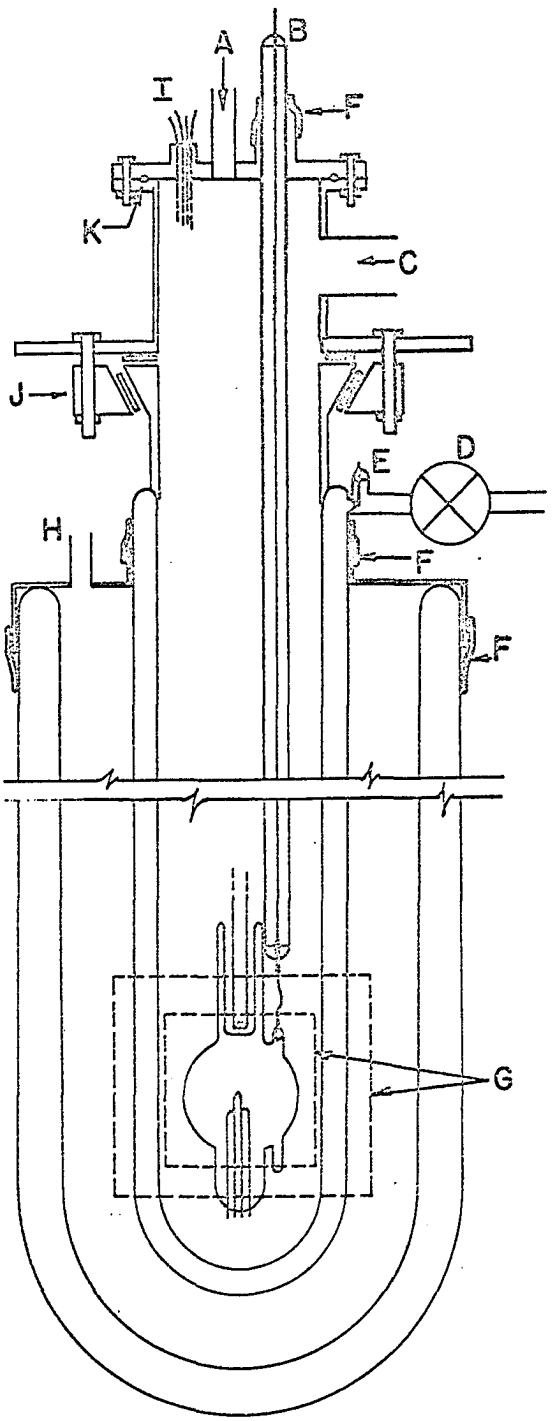
A
B
C
D
E
F
G
H
I
J
K

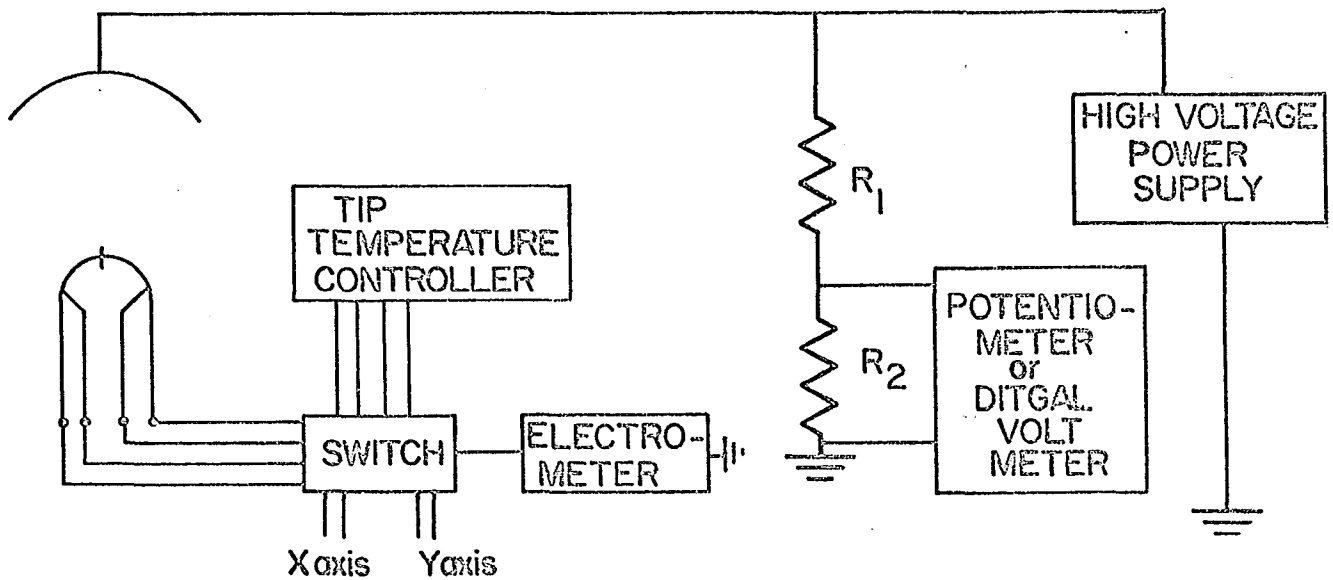

Figure 15. Schematic block diagram of electrical equipment required for field emission studies.

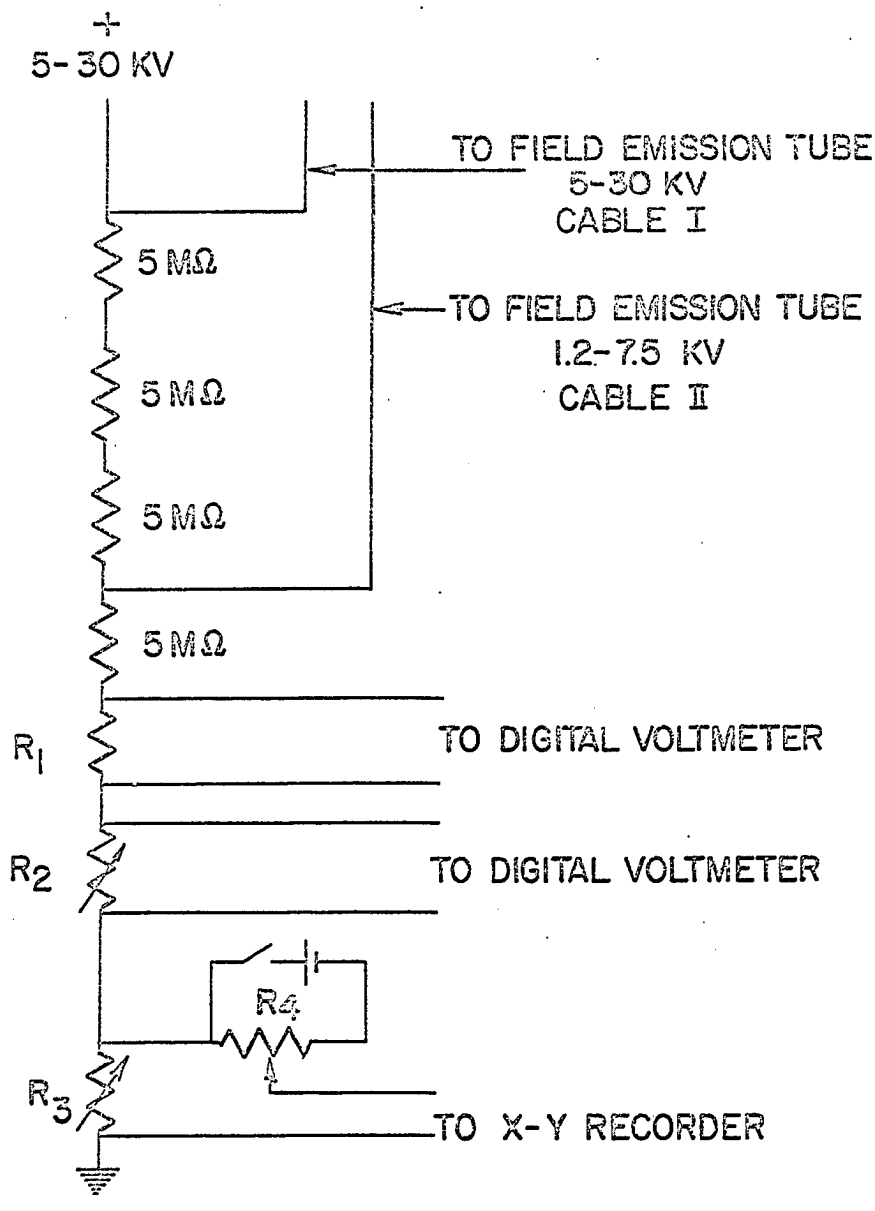

Figure 16. Schematic diagram of the voltage divider used for voltage measurement: R, a 1000 Ω resister; R_2, R_3 and R_4, 1000 Ω helipots.

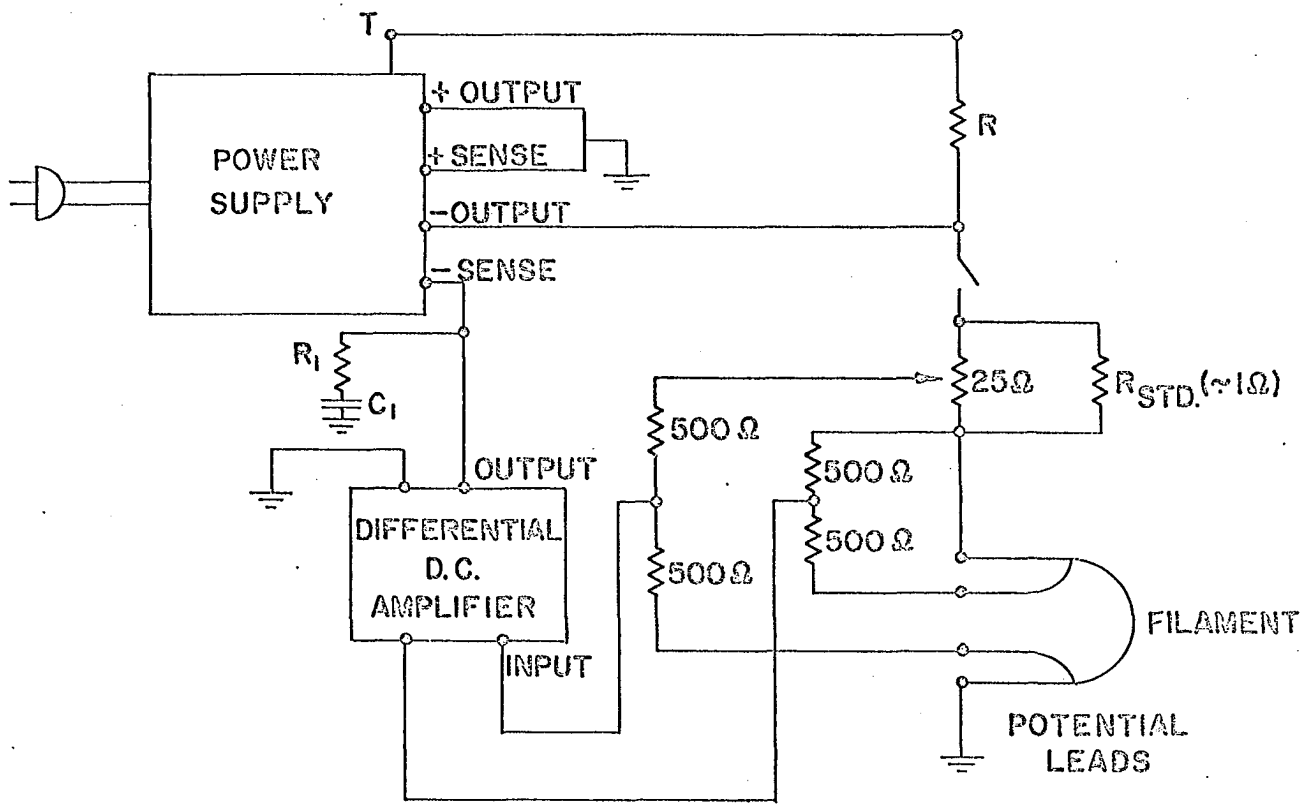

Figure 17. Schematic block diagram of the tip temperature controller: T is the tap-off point in the pre-regulated portion of the power supply; R is adjusted so that, with the output of the dc amplifier open, the current through the bridge is 100 ma; R_1 and C_1 are an anti-hunt circuit, their values depend on the time constant of the tip assembly.

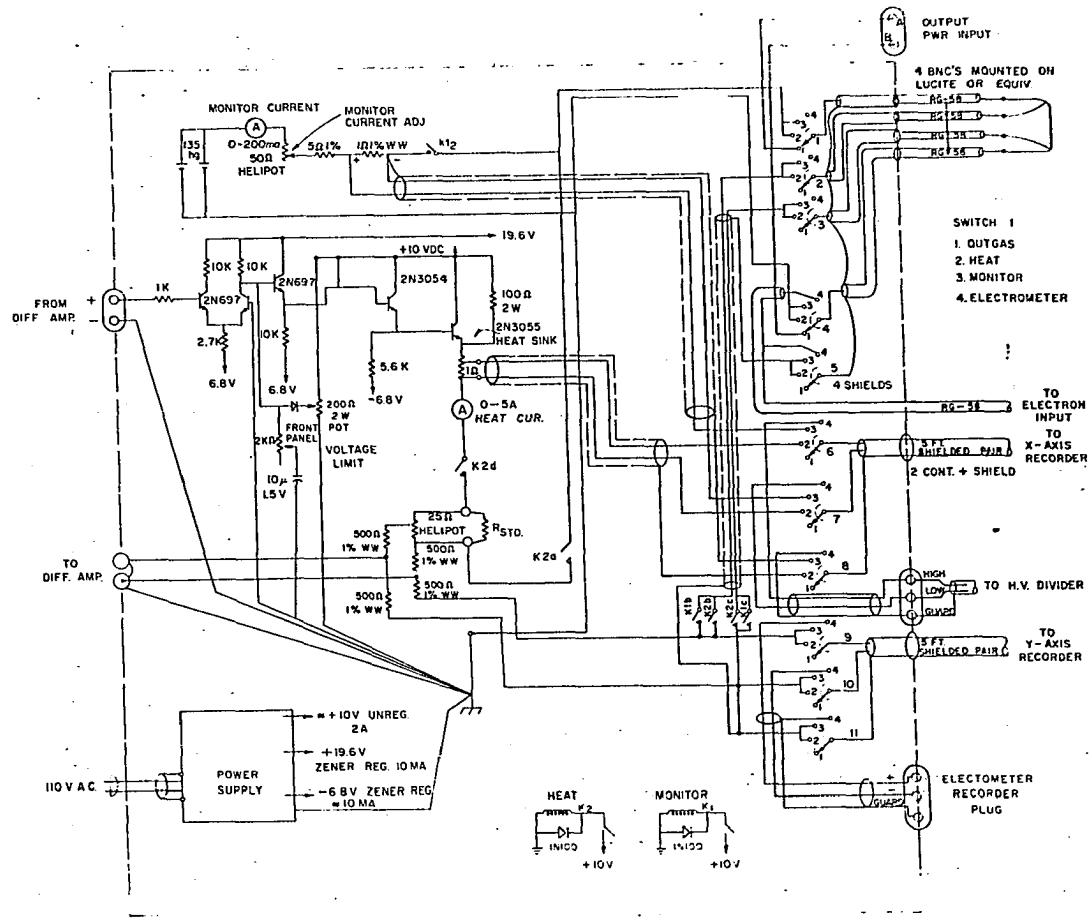

Figure 18. Schematic diagram of the Kelvin double bridge tip temperature controller.

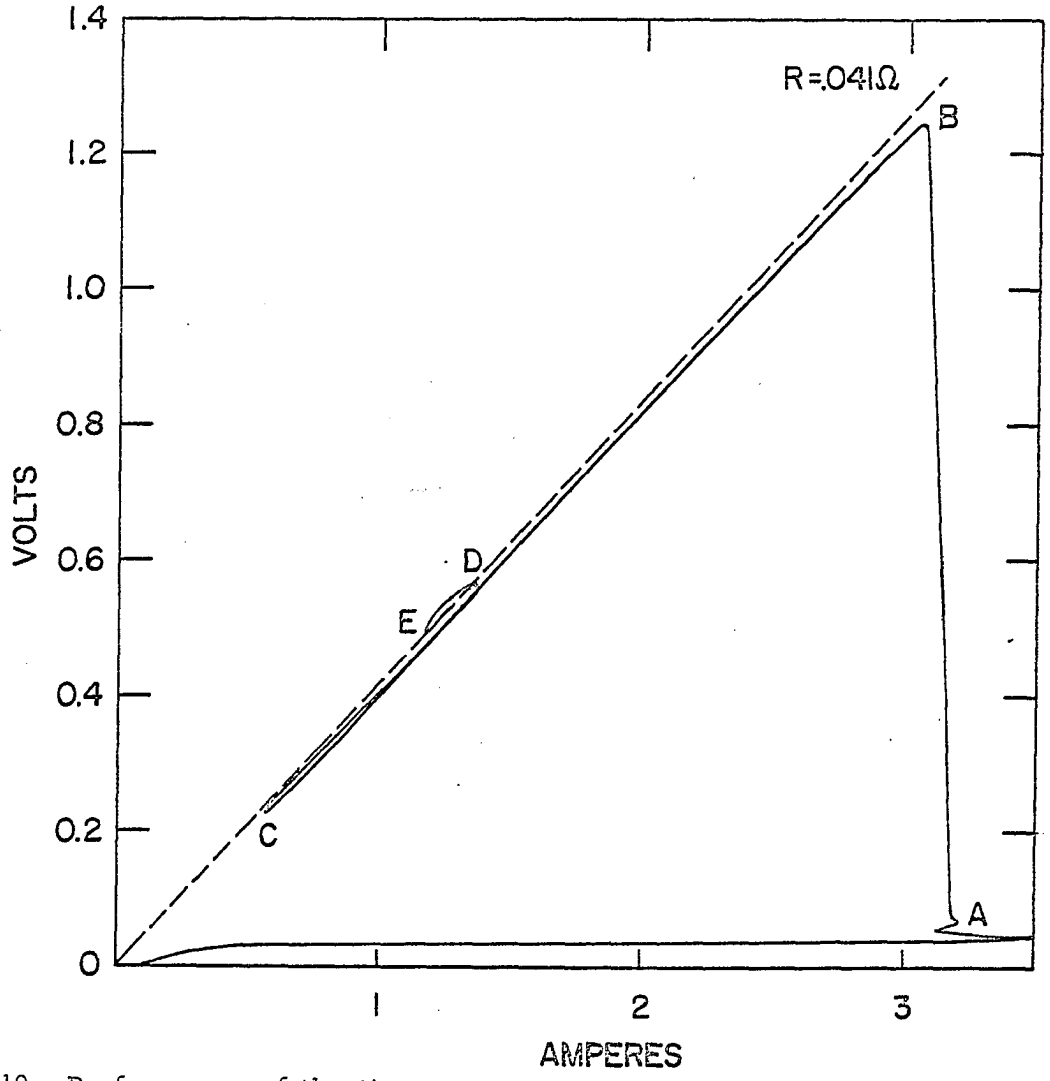

Figure 19. Performance of the tip temperature controller. The dotted line is the line of constant resistance. The time interval between B and C was 0.25 seconds, between C and D, 0.1 seconds, and between D and E 0.05 seconds. The small overshoot between C and D is due to the mechanical inertia of the pen. The time interval between A and B was 5 seconds.

Figure 20. Type I diffusion of acetylene on tungsten.

(a) Clean tungsten.

(b) Emitter has received a dose on the upper half of the tip. The tip temperature is 85°K.

(c) Further migration at 85°K.

(d) The boundary has stopped due to depletion of physically adsorbed gas. The tip temperature is 85°K.

(e) Flashed to 300°K for 20 seconds

(f) Flashed to 450°K for 20 seconds.

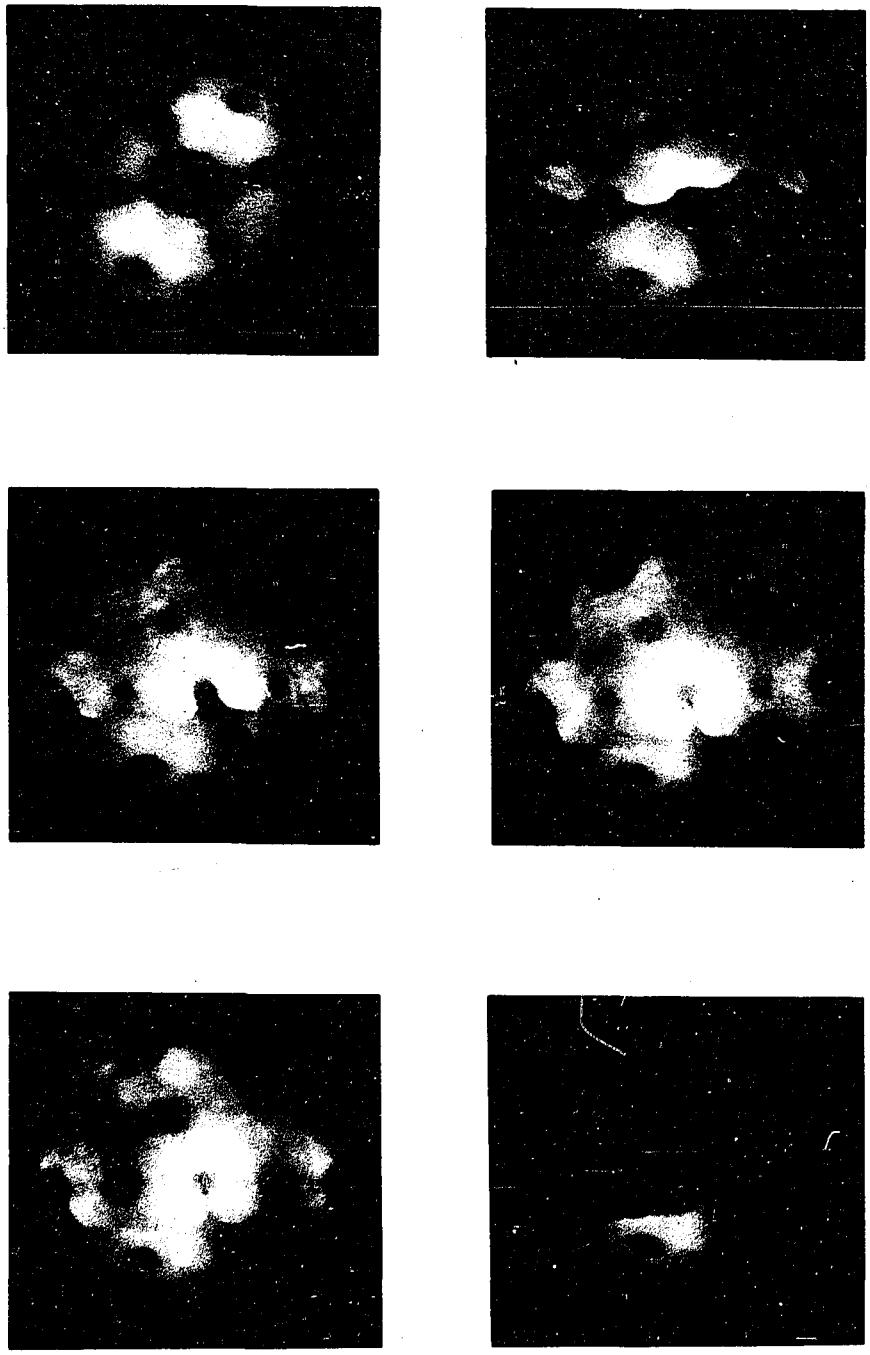

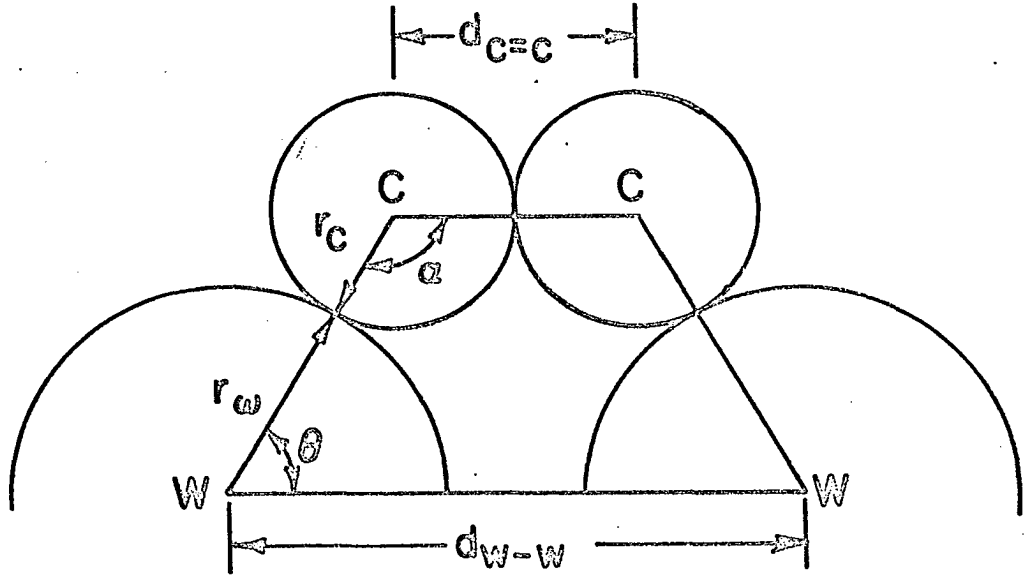

Figure 21. Geometric model for the chemisorption of acetylene on tungsten.

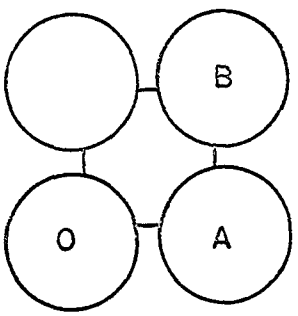

100 PLANE

O-A 3.16 Å

O-B 4.47 Å

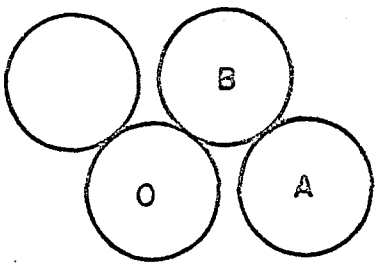

110 PLANE

O-A 3.16 Å

O-B 2.74 Å

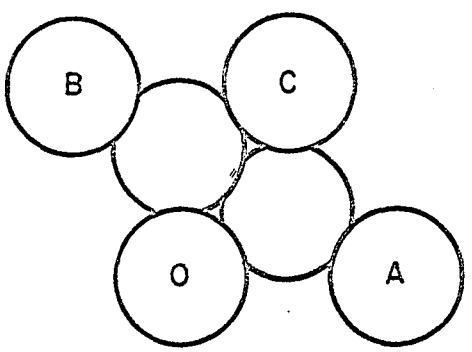

111 PLANE

O-A 4.47 Å

O-B 4.47 Å

O-C 4.47 Å

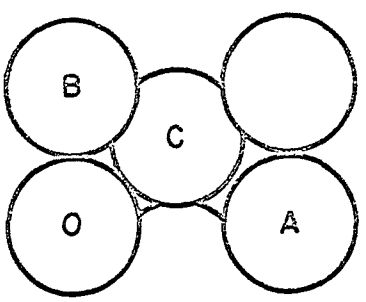

112 PLANE

O-A 4.47 Å

O-B 2.74 Å

O-C 3.16 Å

Figure 22. Diagrams of the prominent planes in field electron images: (a), 100 plane; (b), 110 plane; (c), 111 plane; (d), 112 plane.

Figure 23. Type I diffusion of ethylene on tungsten.

(a) The emitter has received a dose of ethylene on the upper half of the tip.

(b) Tip is heated to 85°K.

(c) Further diffusion at 85°K.

(d) Further diffusion at 85°K.

(e) Further diffusion at 85°K.

(f) The boundary has stopped due to the depletion of physically adsorbed gas.

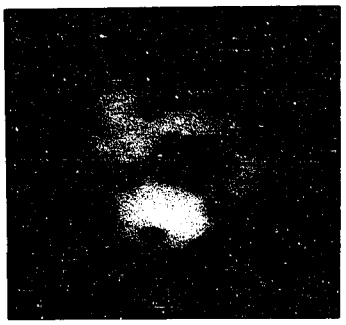

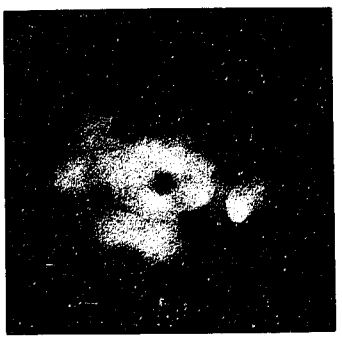

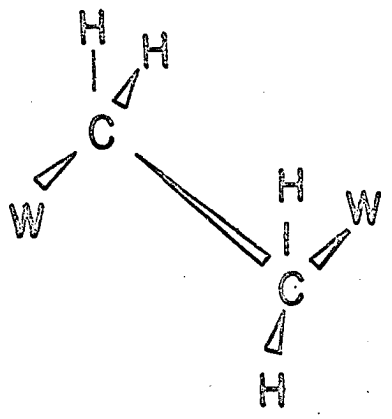

"TRANS" ETHYLENE

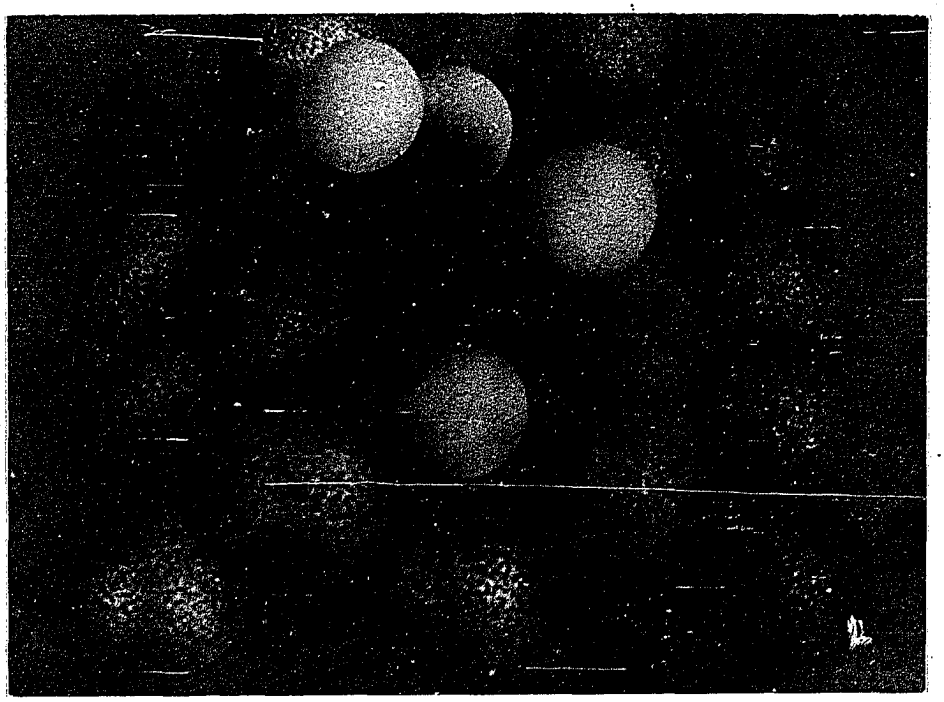

Figure 24. Chemisorption of ethylene "trans" across the 4.47Å spacings on tungsten.

Figure 25. Effect of the variation of enthalpy with surface coverage in the kinetic analysis of surface reactions. (a) Generated θ vs time curves for a 1st order reaction with enthalpy given by $\Delta H = \Delta H_o - \alpha\theta$ where ΔH_o is 30 kcal. Temperature was taken to be 450°K (upper curve α = 20 kcal/monolayer, lower curve α = 0). (b) Kinetic analysis of the α = 0 curves of 16 (a). (Note that 1st order plot is linear.) (c) Kinetic analysis of the α = 20 kcal/monolayer curve. (Note that the 2nd order plot is more nearly linear than the first plot.)

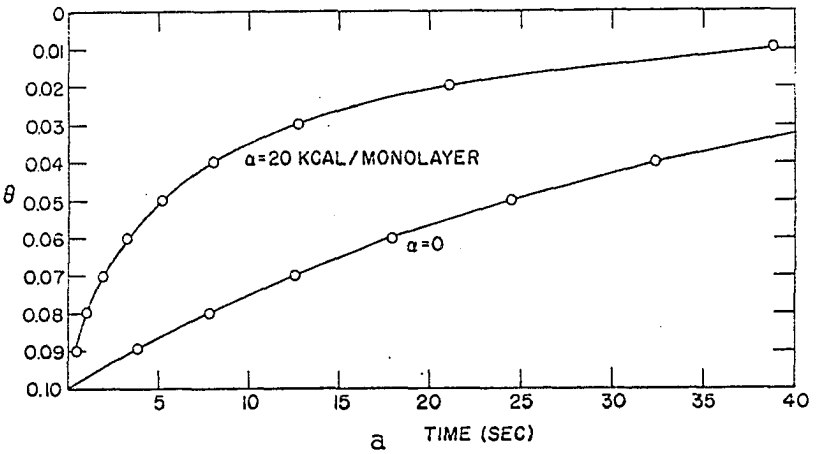
θ
0
0.01
0.02
0.03
0.04
0.05
0.06
0.07
0.08
0.09
0.10
α=20 KCAL/MONOLAYER
α=0
5
10
15
20
25
30
35
40
TIME (SEC)

a

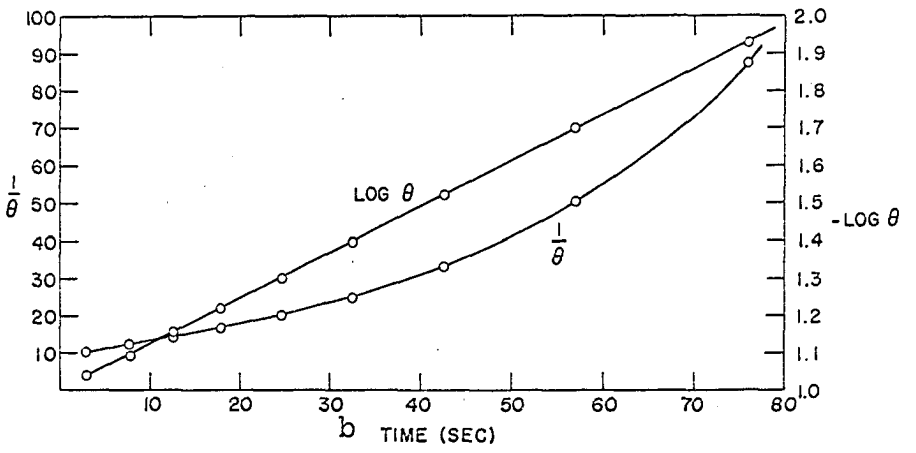
1/θ
100
90
80
70
60
50
40
30
20
10
LOG θ
1/θ
2.0
1.9
1.8
1.7
1.6
1.5
1.4
1.3
1.2
1.1
1.0
-LOG θ
10
20
30
40
50
60
70
80
TIME (SEC)

b

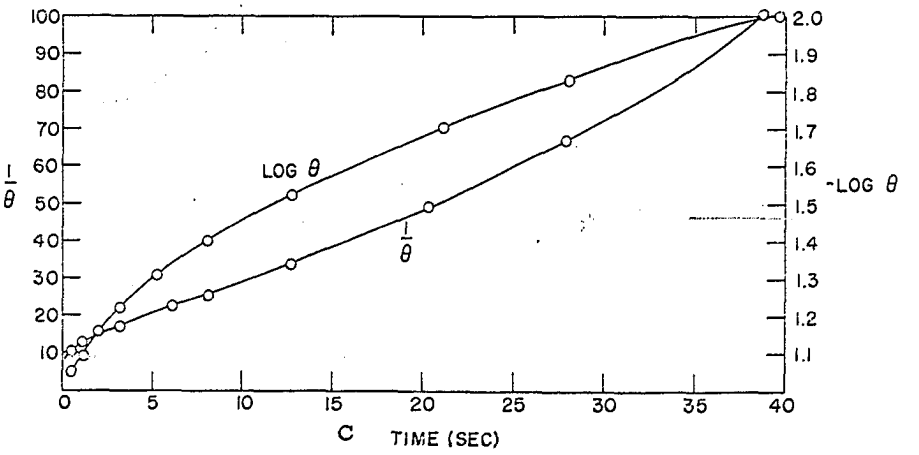
1/θ
100
90
80
70
60
50
40
30
20
10
LOG θ
1/θ
2.0
1.9
1.8
1.7
1.6
1.5
1.4
1.3
1.2
1.1
-LOG θ
0
5
10
15
20
25
30
35
40
TIME (SEC)

c

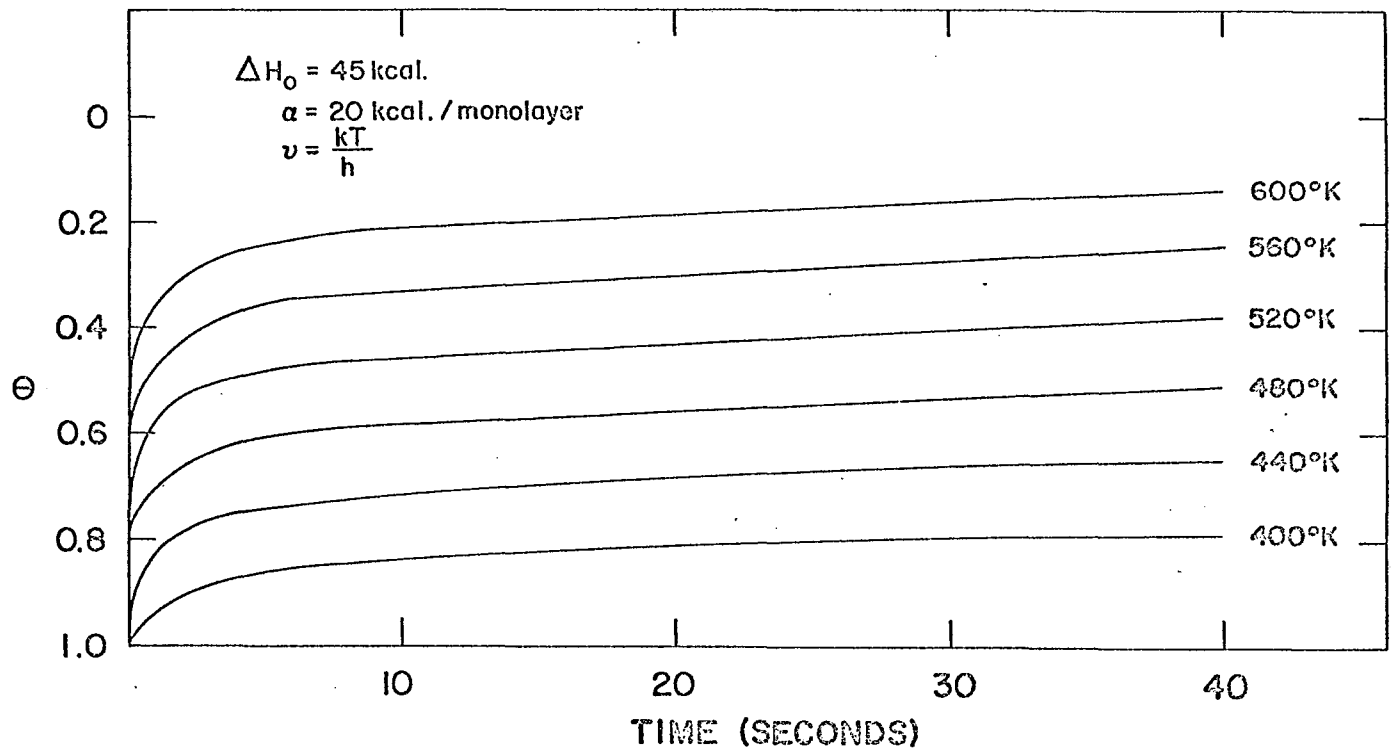

Figure 26. Generated first order desorption isotherms. ΔH_o equals 45 kcal/mole, α equals 20 kcal/monolayer mole, and ν equals kT/h.

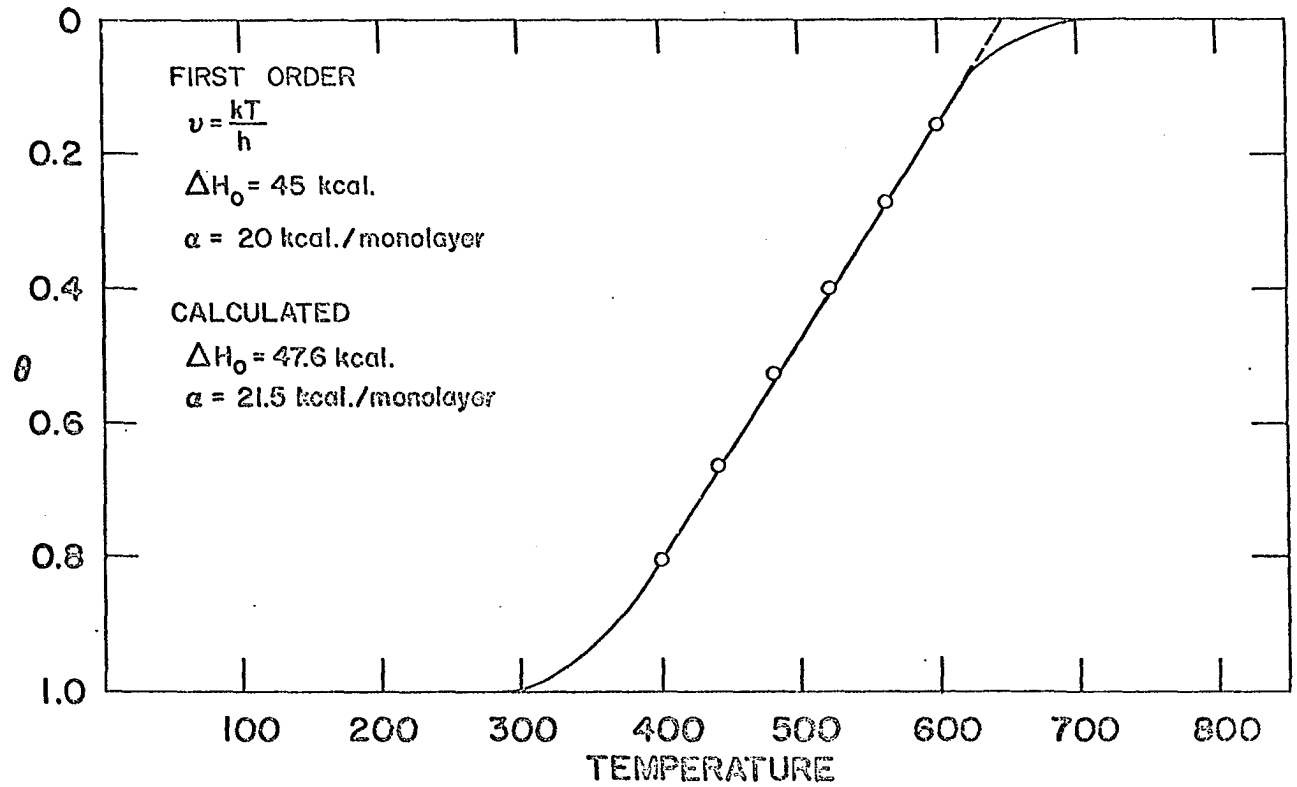

Figure 27. Surface coverage as a function of temperature. These results were obtained from the generated data of Figure 26 for a constant time interval of 30 seconds.

Figure 28. The decomposition of acetylene on clean tungsten. The tip was flashed to the temperature indicated for 20 seconds.

(a) Clean tungsten.
(b) Dosed with acetylene 75°K.
(c) 150°K
(d) 200°K
(e) 250°K
(f) 300°K

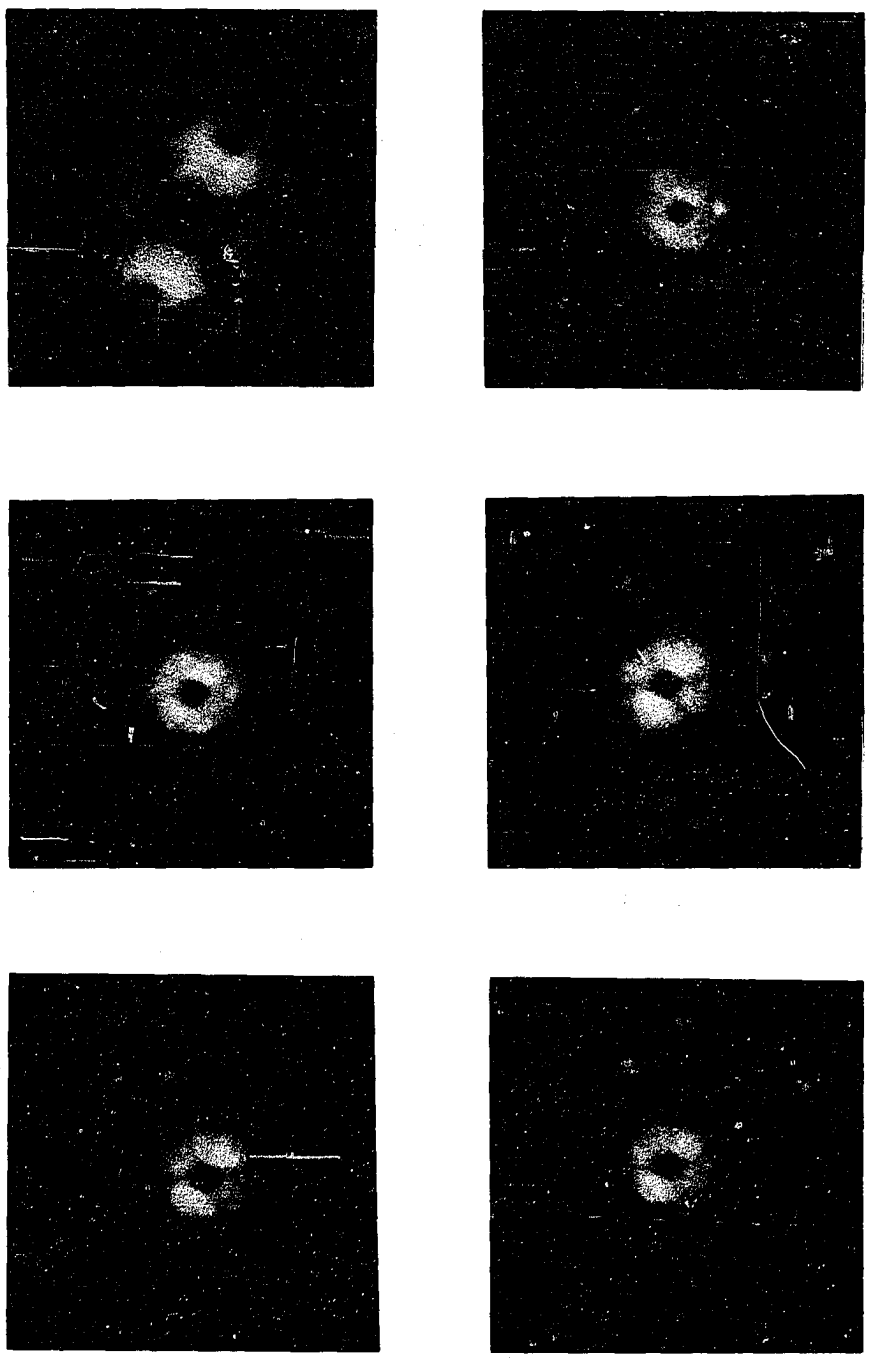

Figure 29. The emitter of Figure 28 flashed to the temperature indicated for 20 seconds.

(a) 400°K
(b) 425°K
(c) 450°K
(d) 475°K
(e) 500°K
(f) 525°K

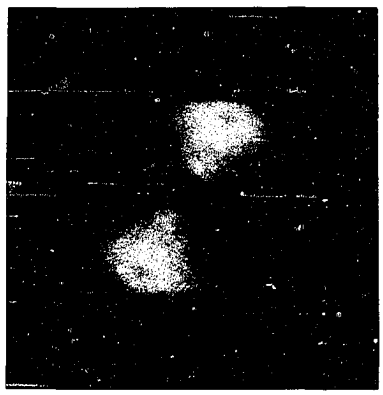

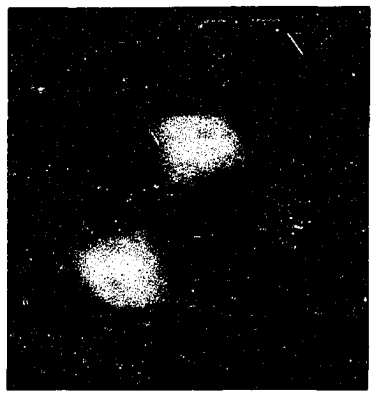

Figure 30. The emitter of Figure 28 flashed to the temperature indicated for 20 seconds.

(a) 525
(b) 550
(c) 575
(d) 600
(e) 625
(f) 650

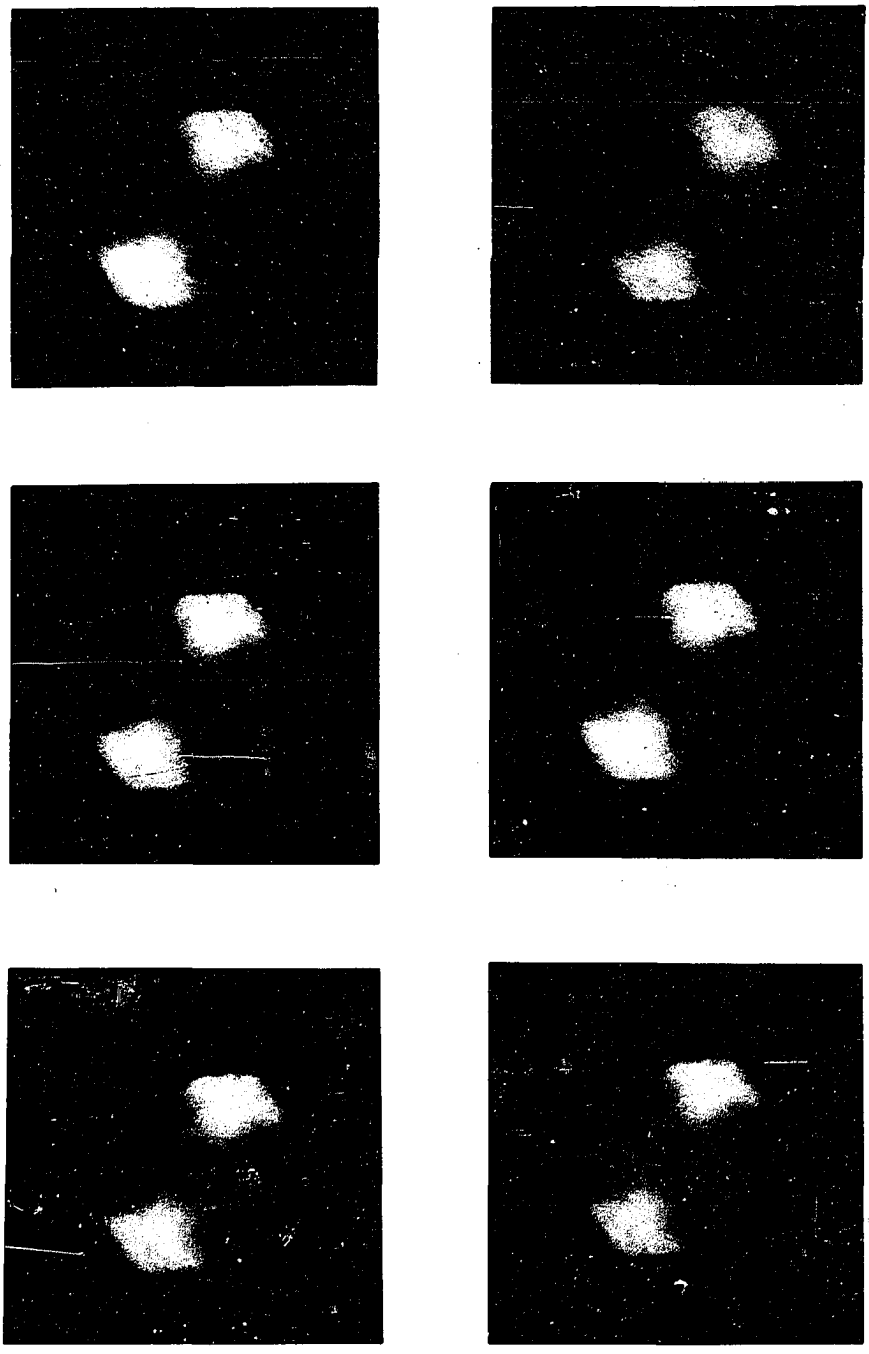

Figure 31. The emitter of Figure 28 flashed to the temperature indicated for 20 seconds.

(a) 675
(b) 700
(c) 725
(d) 750
(e) 800
(f) 850

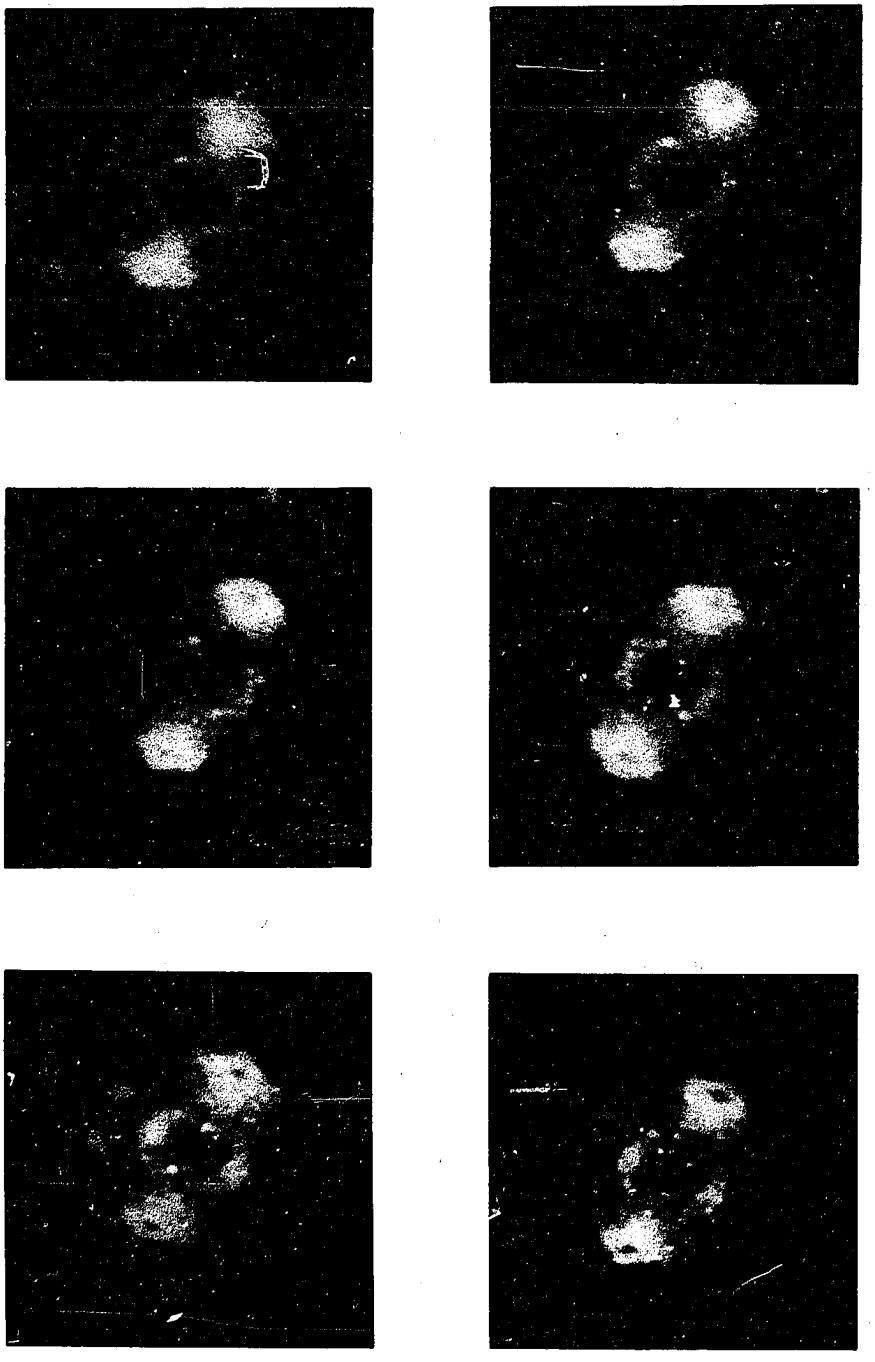

Figure 32. The emitter of Figure 28 flashed to the temperature indicated for 20 seconds.

(a) 900 (b) 950
(c) 1000 (d) 1050

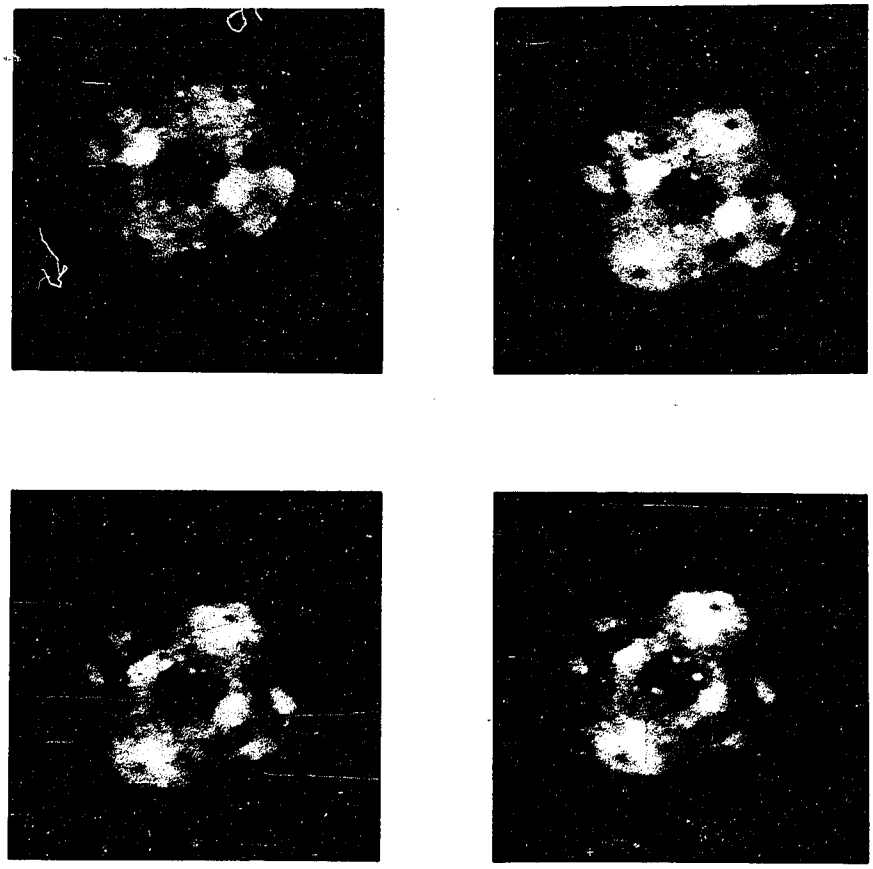

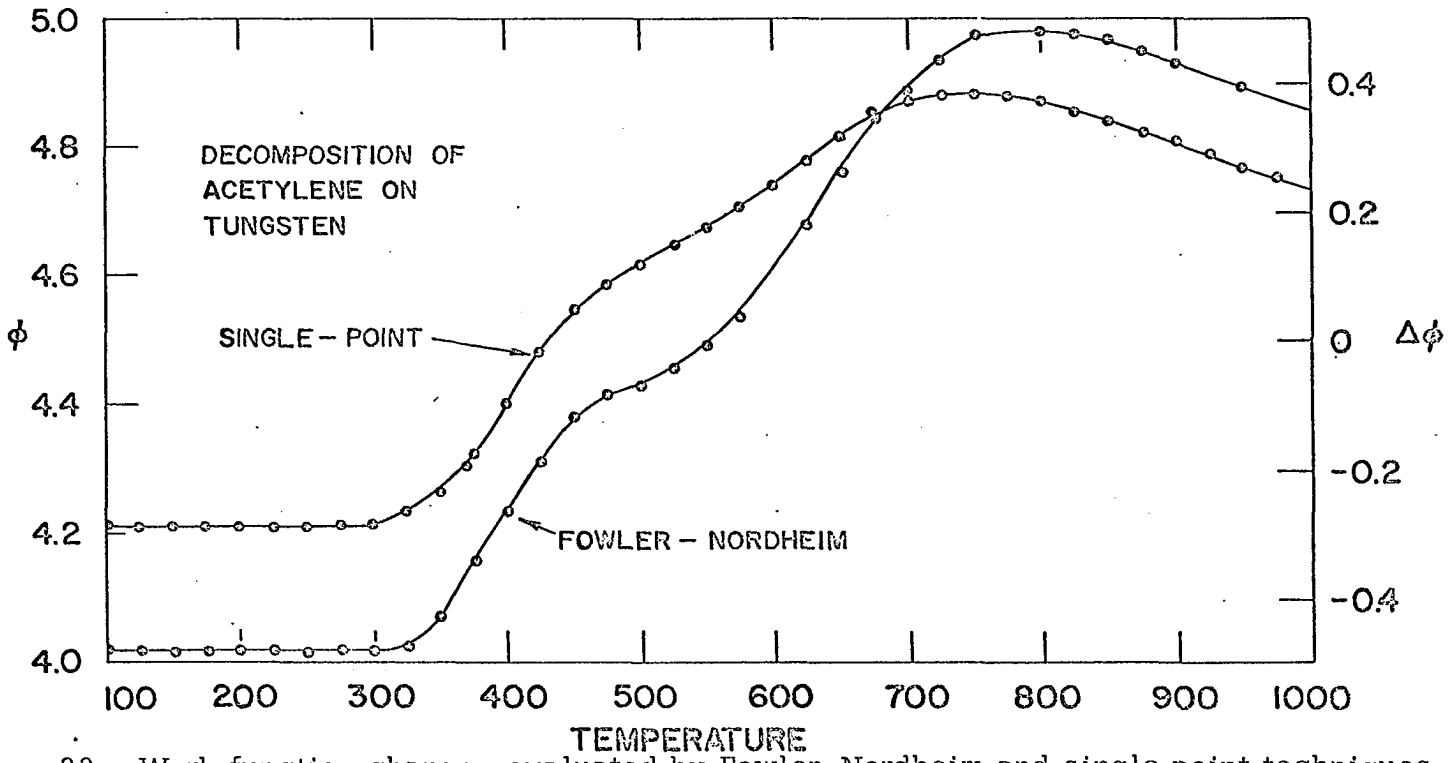

Figure 33. Work function change, evaluated by Fowler-Nordheim and single point techniques, versus heating temperature for an acetylene covered tungsten emitter. The emitter was held at each temperature for 20 seconds. The work function of clean tungsten is 4.51 ev.

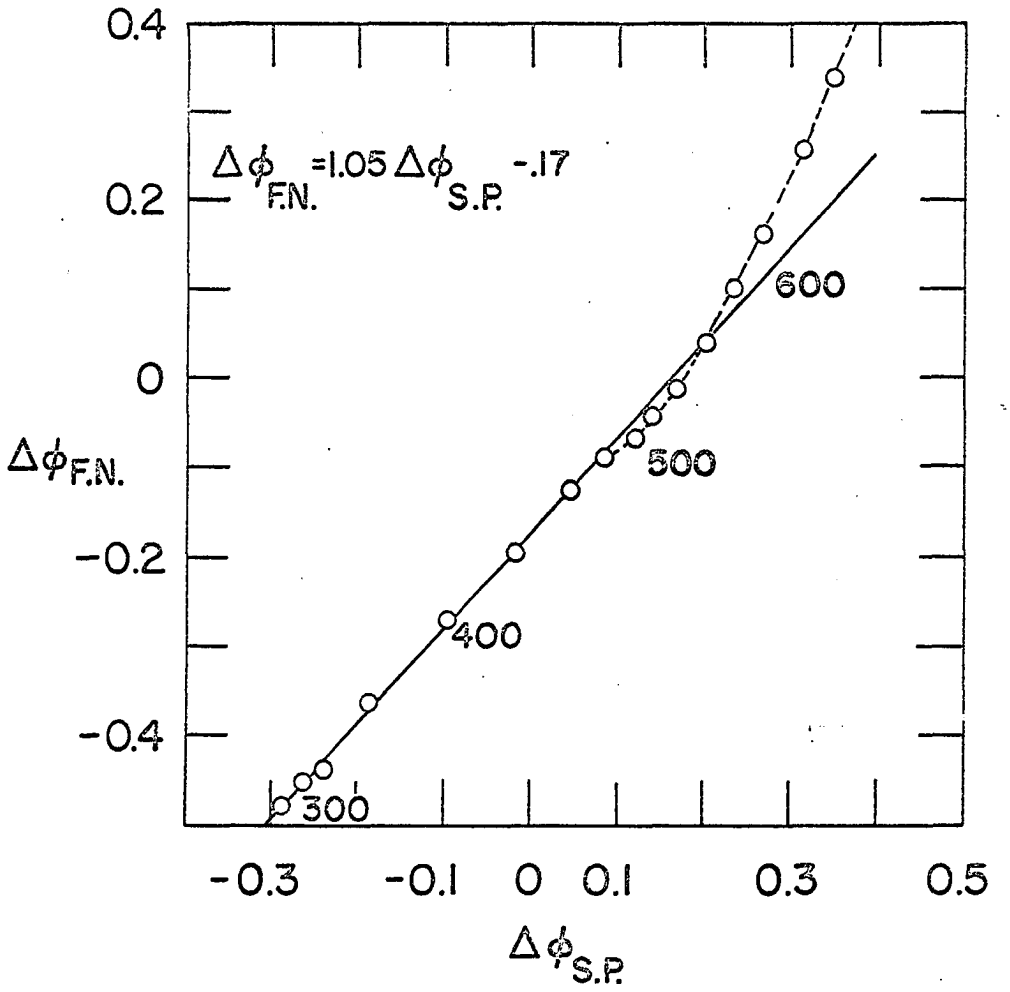

Figure 34. Comparison of the Fowler-Nordheim and single point work function measurements.

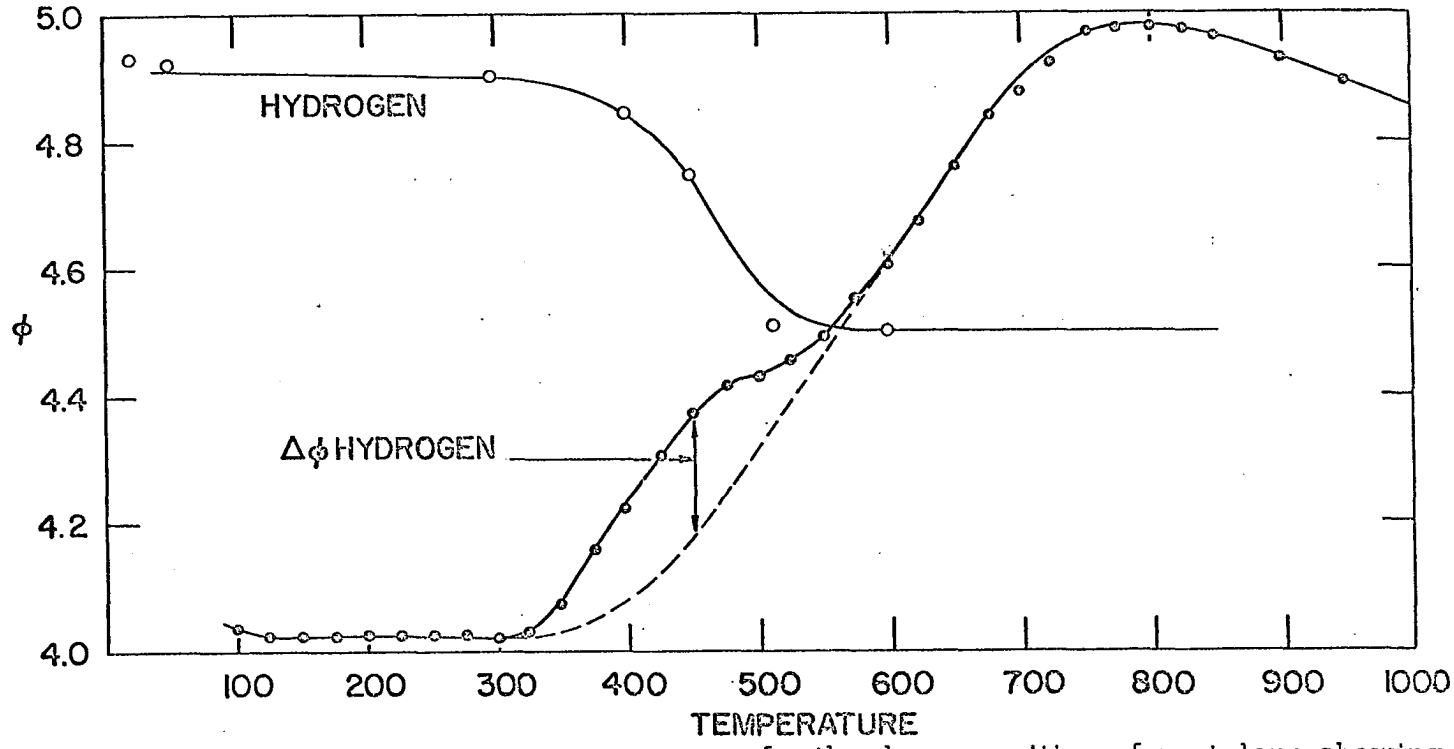

Figure 35. Work function versus temperature curve for the decomposition of acetylene showing the contribution of hydrogen to the measured work function. The dotted line represents work functions due to the acetylene and carbon on the surface.

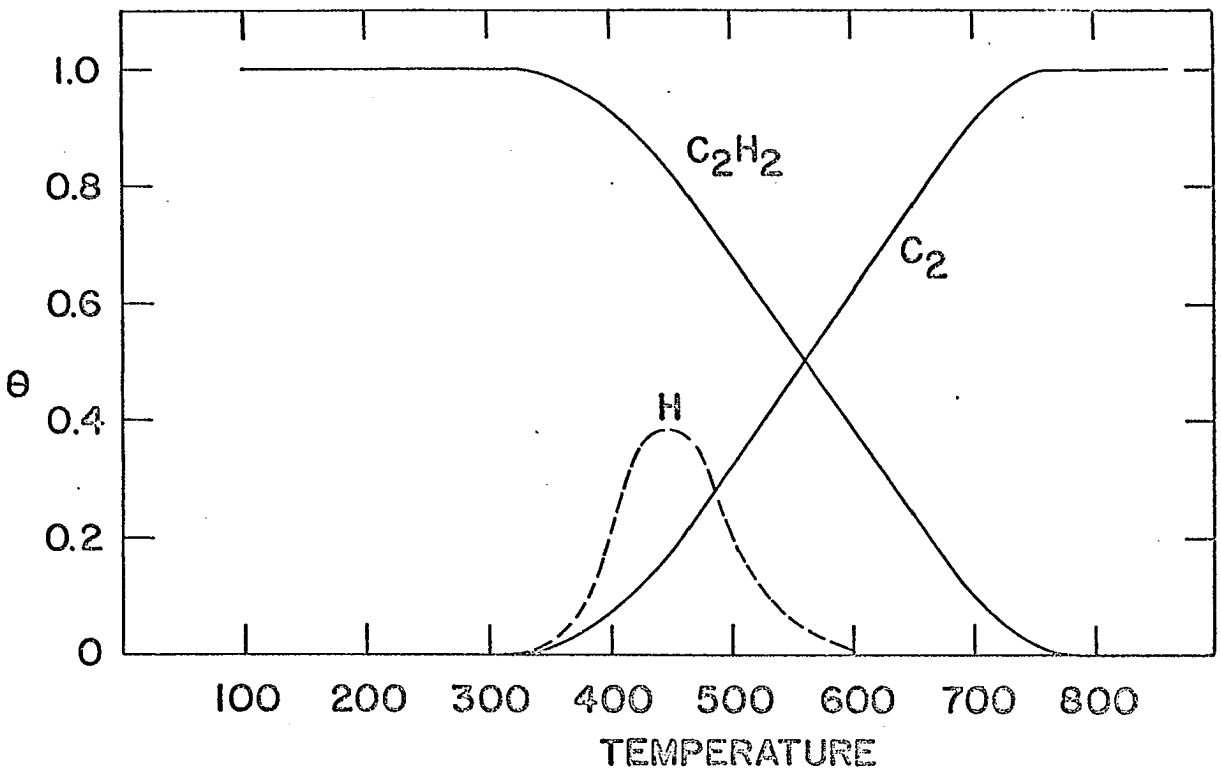

Figure 36. Surface coverages of acetylene, hydrogen, and carbon species as a function of temperature. The parameter θ should be understood as a relative surface coverage, there is no way to relate absolutely the surface coverages of acetylene and carbon to that of hydrogen.

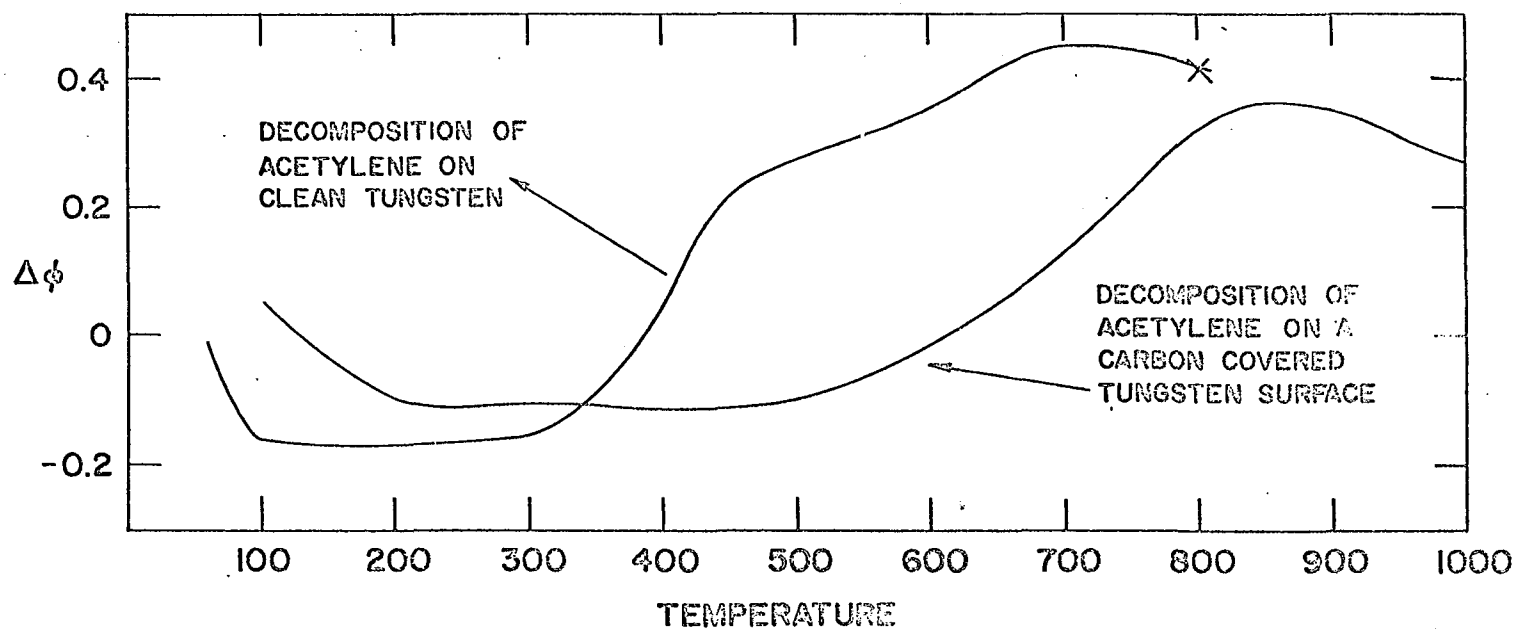

Figure 37. Decomposition of acetylene on a carbon covered tungsten surface as determined by single point techniques. The carbon-tungsten surface was produced by decomposing an acetylene covered emitter at 800°K. The tip was then cooled to 50°K and redosed.

Figure 38. The decomposition of acetylene on a carbon-tungsten surface. The carbon-tungsten surface was produced by decomposing an acetylene covered emitter at 800°K. The tip was cooled to 50°K and redosed. The tip was then flashed to the temperature indicated for 20 seconds.

(a) carbon-tungsten surface
(b) 100°K
(c) 150°K
(d) 200°K
(e) 250°K
(f) 300°K

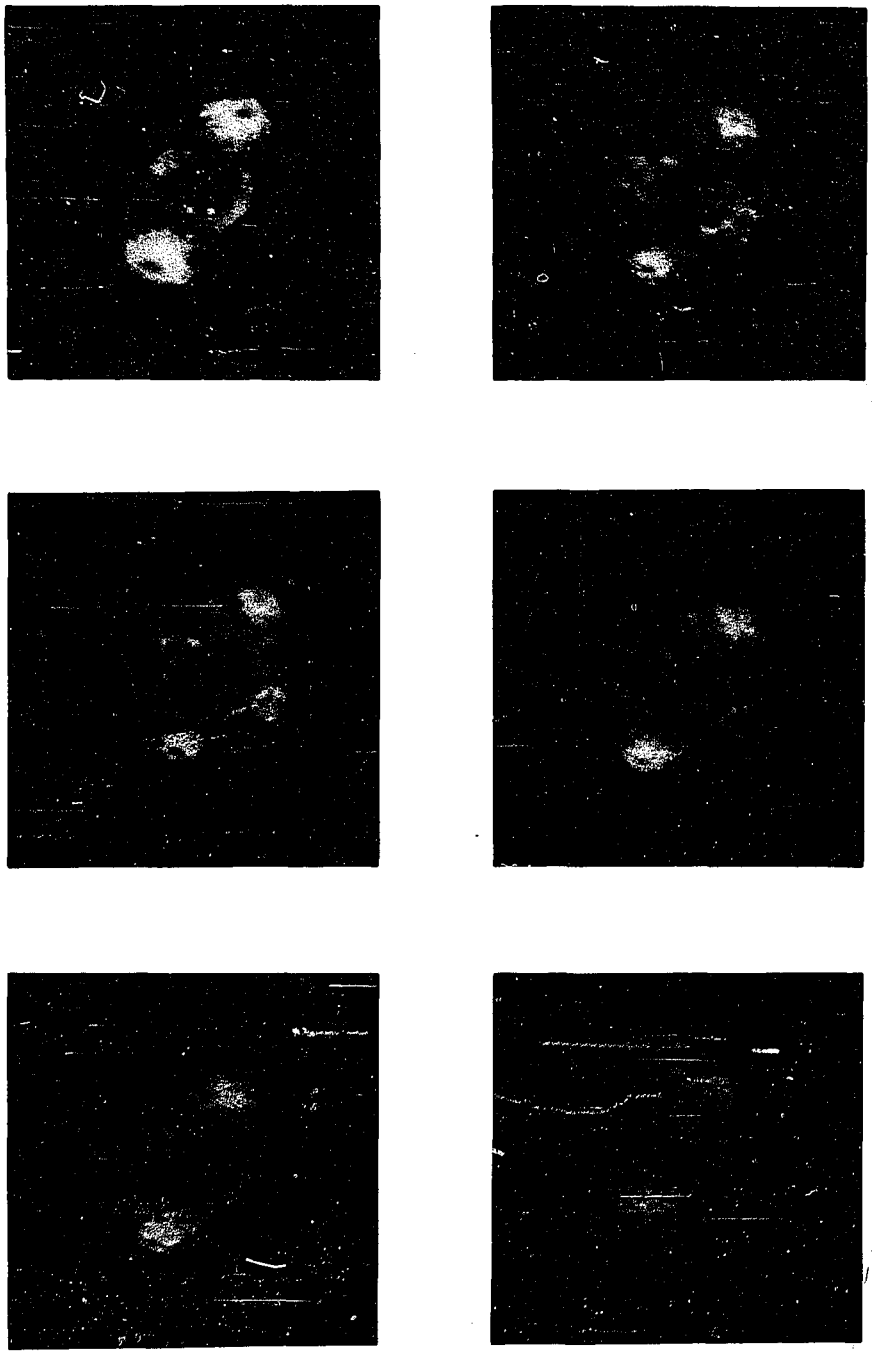

Figure 39. The emitter of Figure 38 flashed to the indicated temperature for 20 seconds.

(a) 350°K
(b) 400°K
(c) 450°K
(d) 500°K
(e) 550°K
(f) 600°K

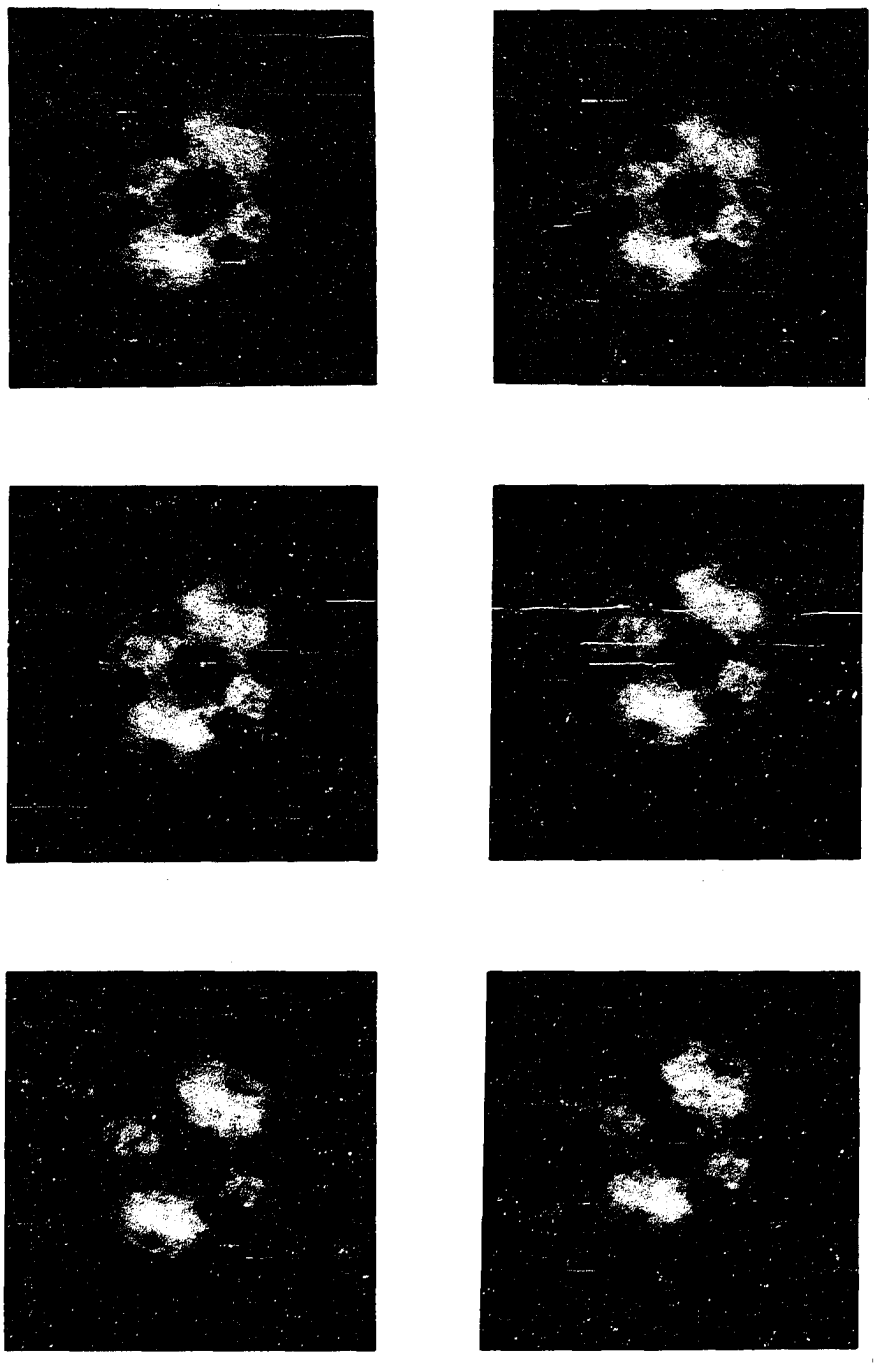

Figure 40. The emitter of Figure 38 flashed to the indicated temperature for 20 seconds.

(a) 650°K
(b) 700°K
(c) 750°K
(d) 800°K
(e) 850°K
(f) 1000°K

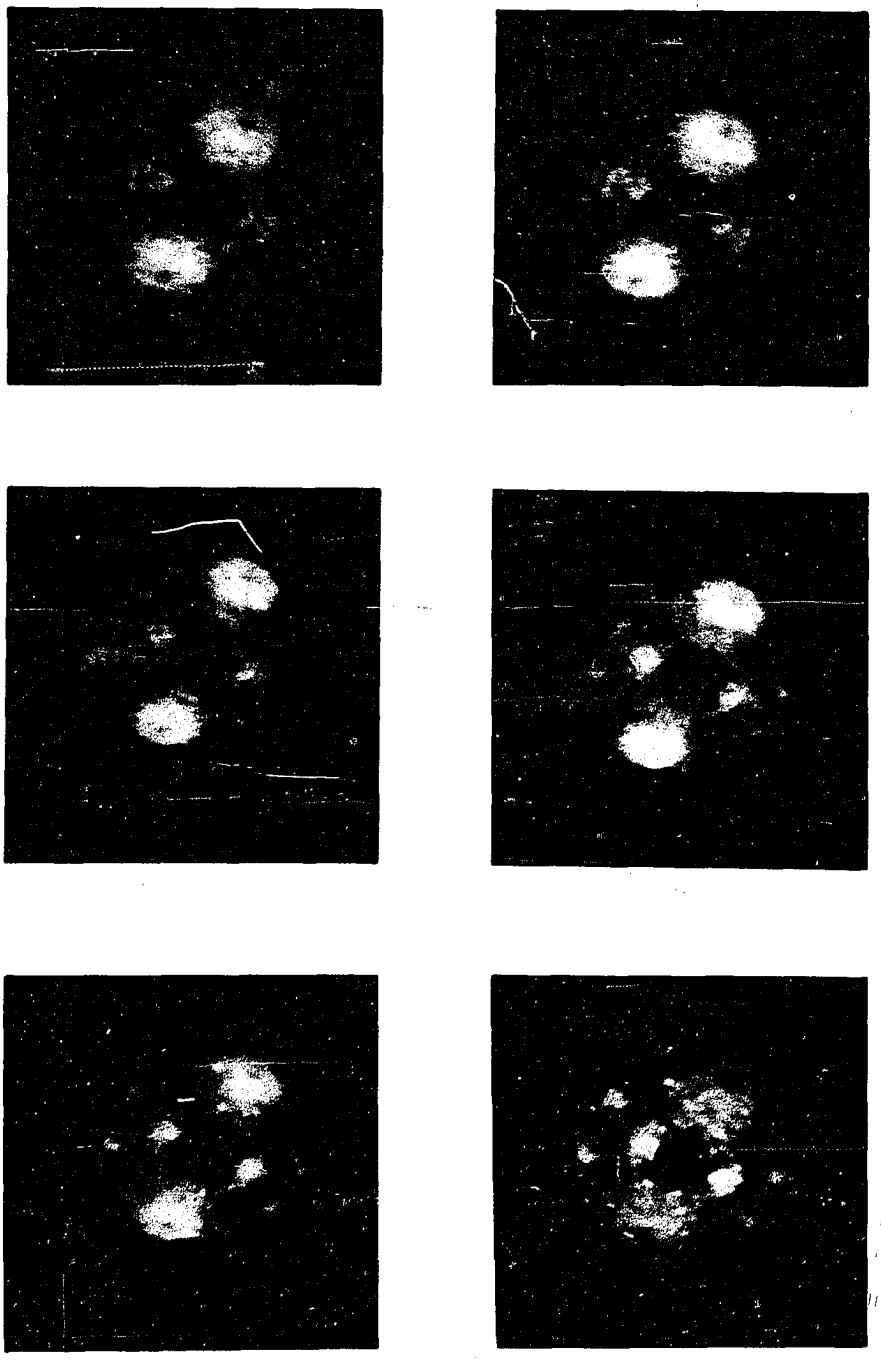

Figure 41. The decomposition of ethylene on clean tungsten. The tip was flashed to the indicated temperature for 20 seconds.

(a) Clean tungsten

(b) Dosed with ethylene, then heated to 100°K

(c) 150°K

(d) 200°K

(e) 225°K

(f) 250°K

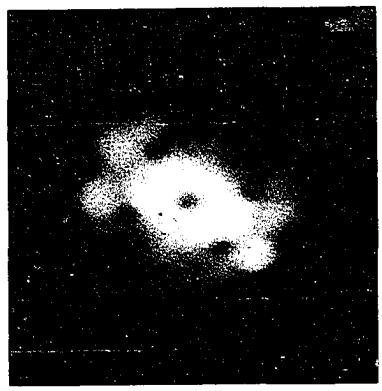

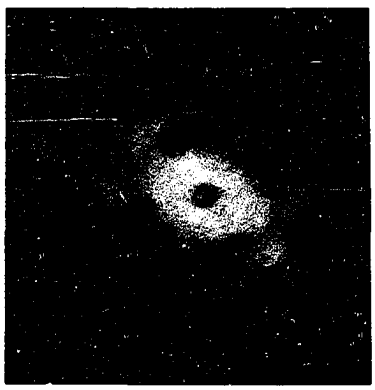

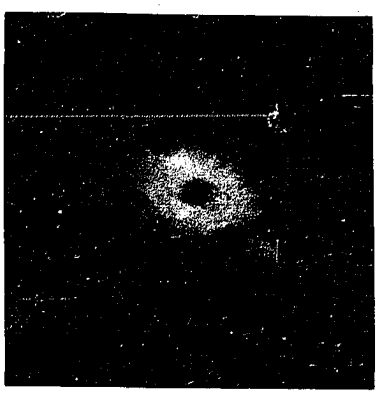

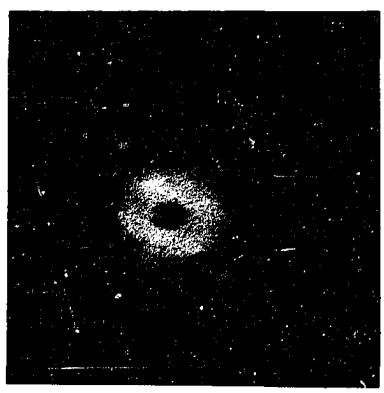

Figure 42. The emitter of Figure 41 heated to the indicated temperature for 20 seconds.

(a) 275°K
(b) 300°K
(c) 325°K
(d) 350°K
(e) 375°K
(f) 400°K

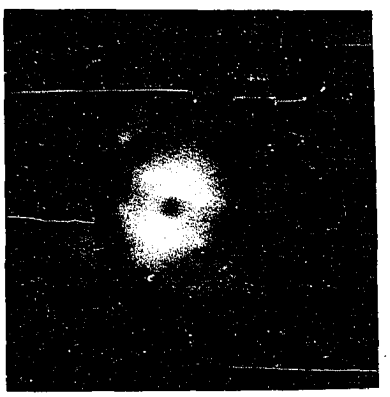

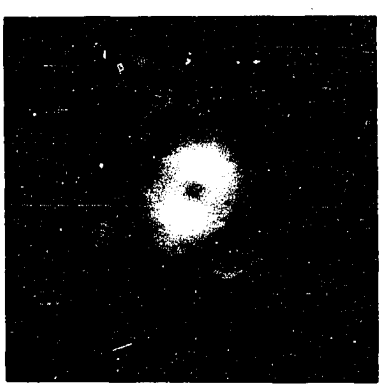
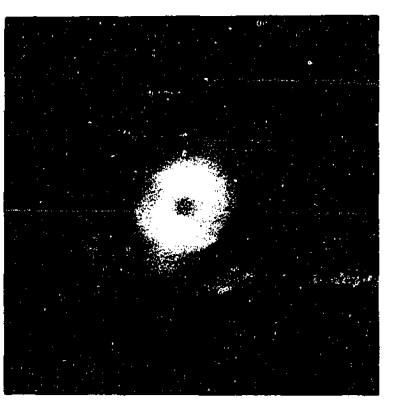

Figure 43. The emitter of Figure 41 heated to the indicated temperature for 20 seconds.

(a) 425°K
(b) 450°K
(c) 475°K
(d) 500°K
(e) 525°K
(f) 550°K

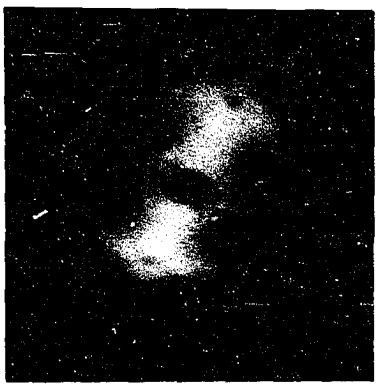
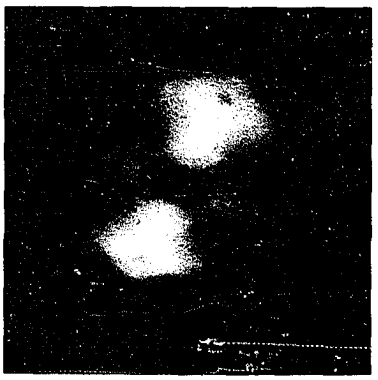
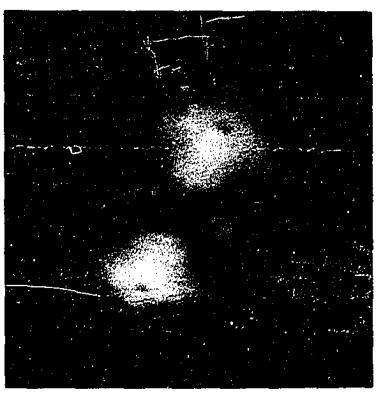
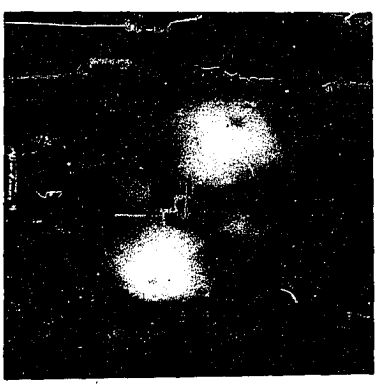
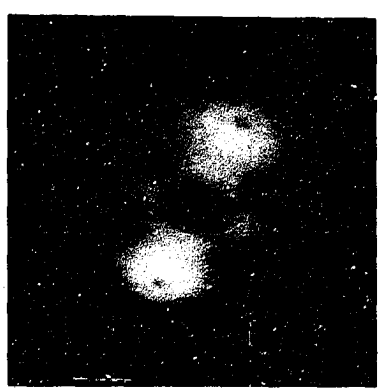


Figure 44. The emitter of Figure 41 heated to the indicated temperature for 20 seconds.

(a) 575°K
(b) 600°K
(c) 625°K
(d) 650°K
(e) 675°K
(f) 700°K

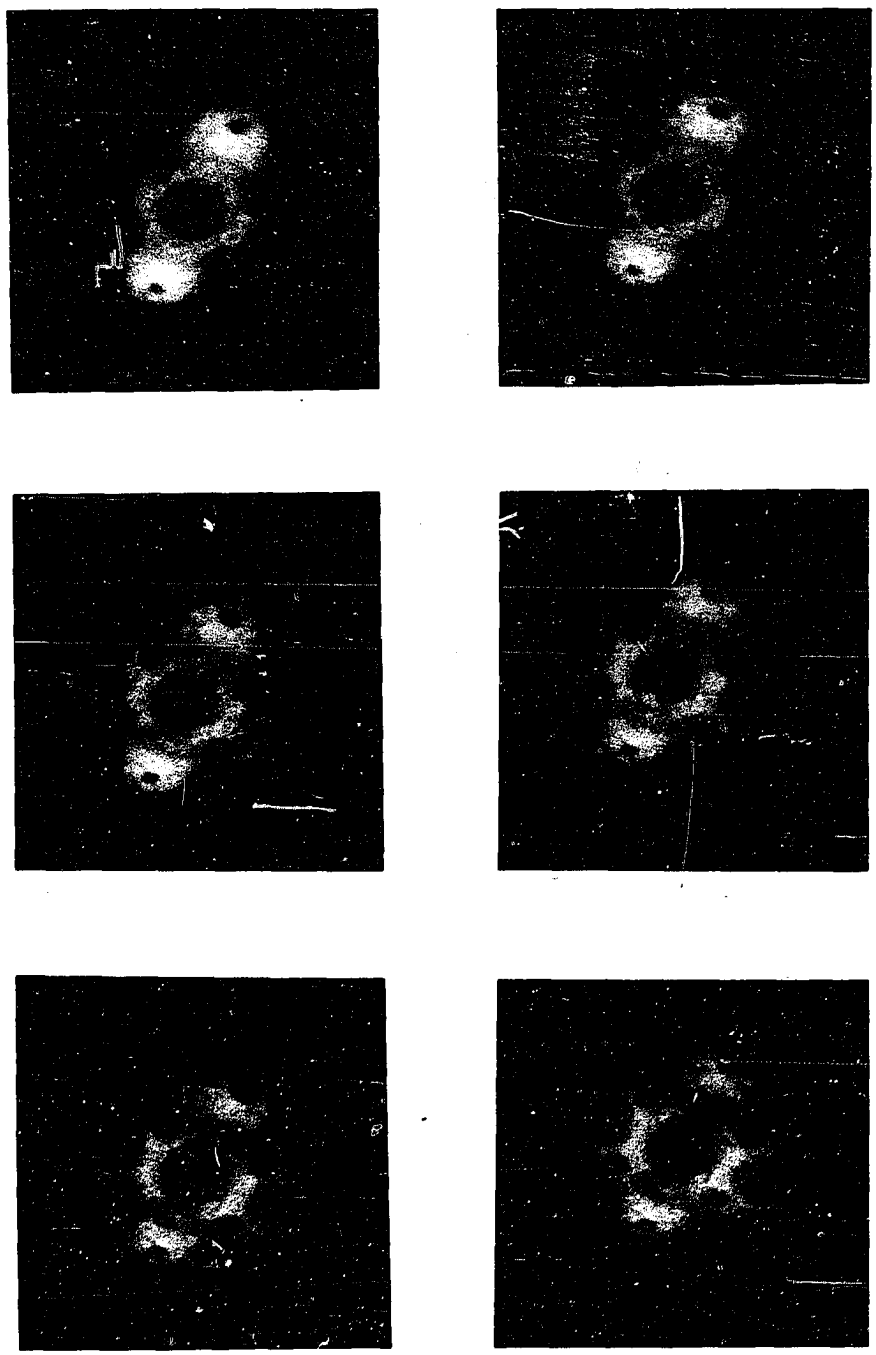

Figure 45. The emitter of Figure 41 heated to the indicated temperature for 20 seconds.

(a) 750°K
(b) 800°K
(c) 900°K
(d) 1000°K
(e) 1100°K
(f) 1200°K




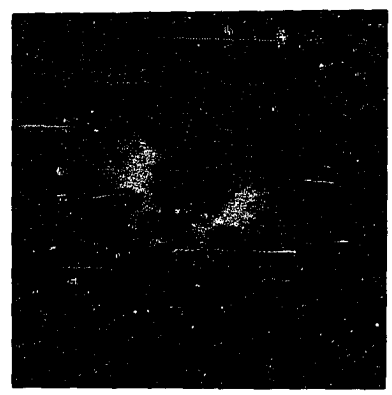
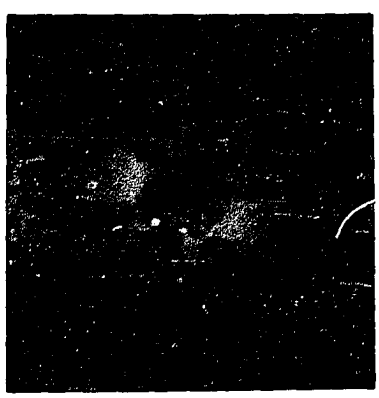
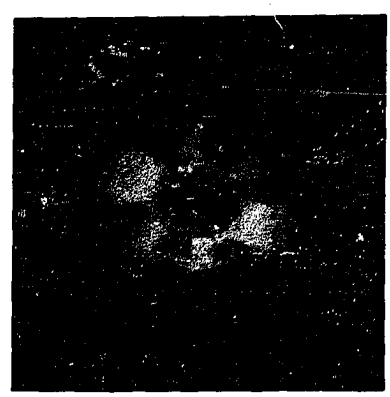

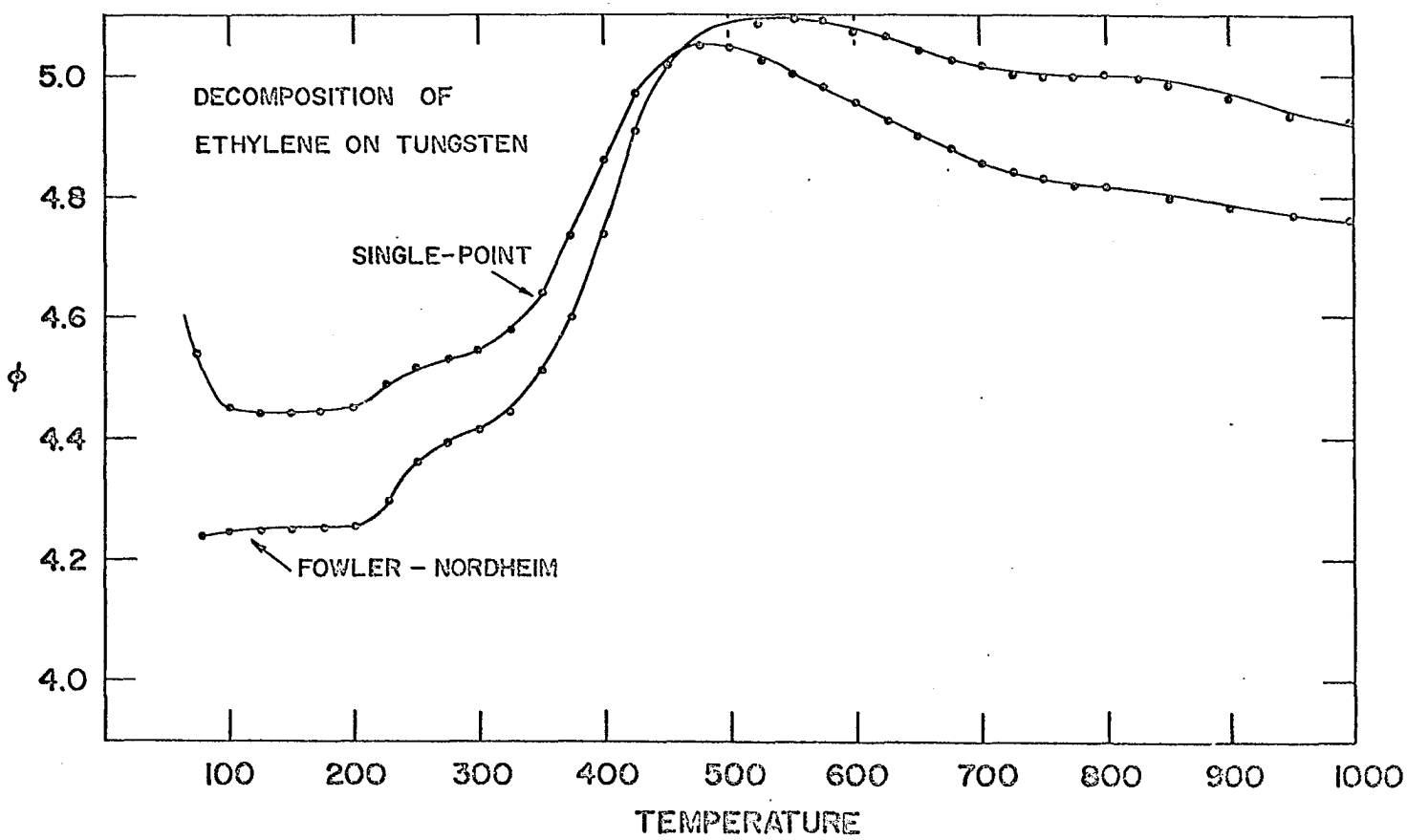

Figure 46. Work function change, evaluated by Fowler-Nordheim and single point techniques, versus temperature for an ethylene covered emitter. The emitter was held at each temperature for 20 seconds. The work function of clean tungsten is 4.51 ev.

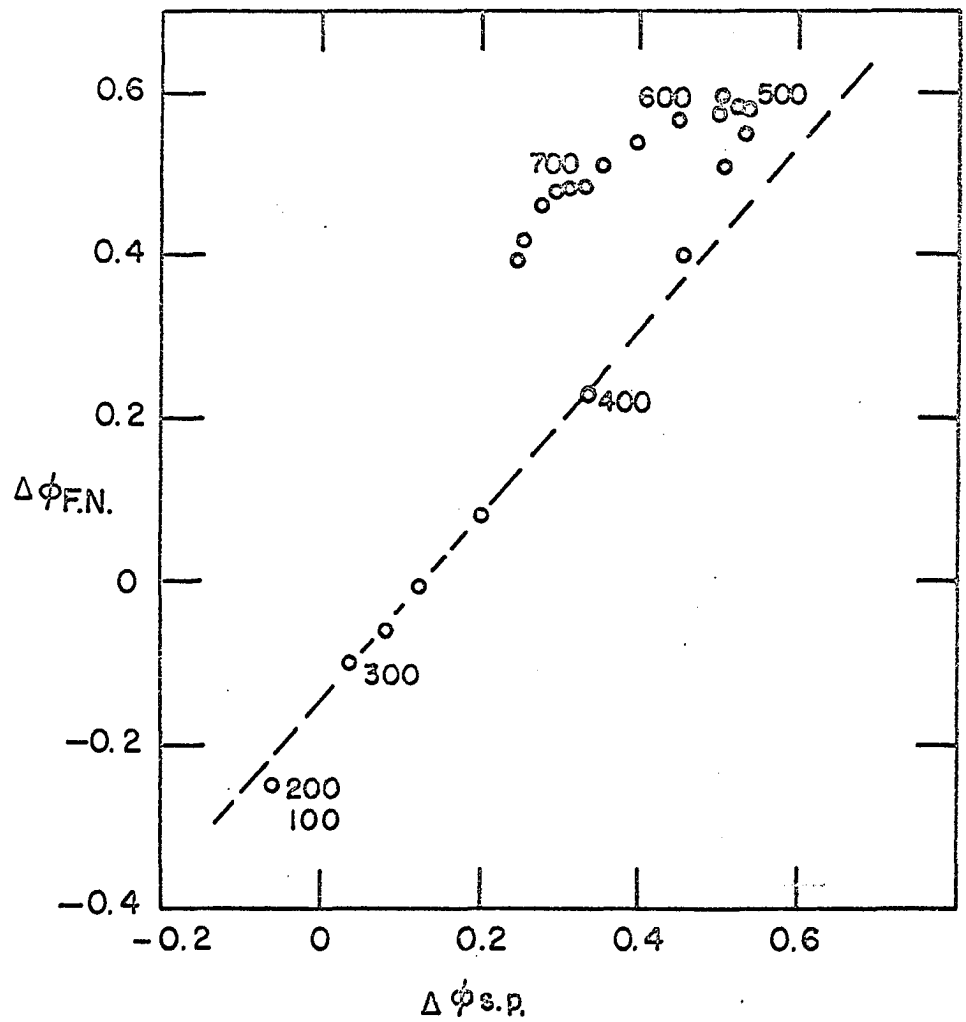

Figure 47. Comparison of the Fowler-Nordheim and single point work function measurements for ethylene on tungsten.

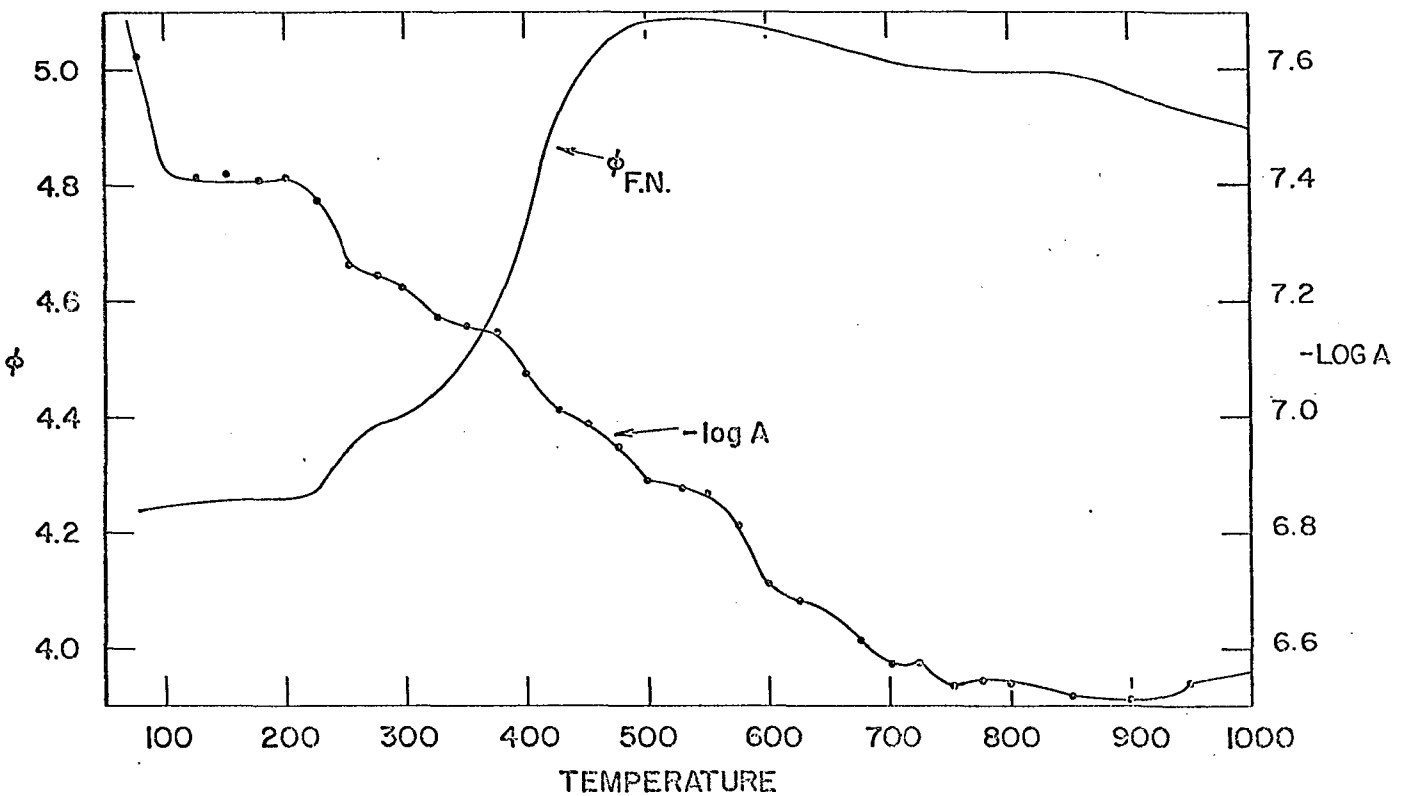

Figure 48. Variation of the logarithm of the pre-exponential of the Fowler-Nordheim equation, - log A, with flash temperature for the decomposition of ethylene on tungsten. The value of -log A for the clean emitter was 7.0.

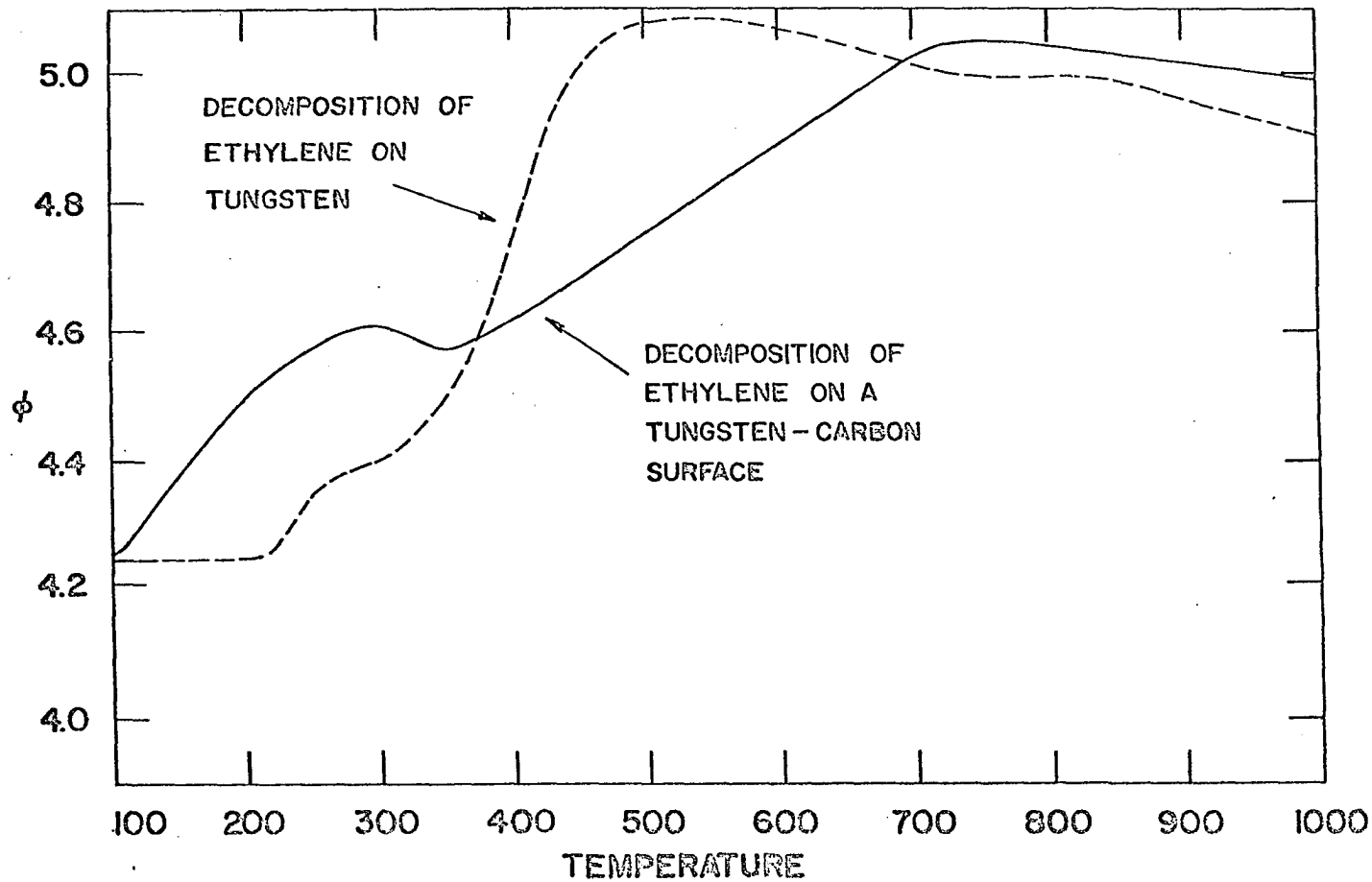

Figure 49. Decomposition of ethylene on a carbon covered tungsten surface as determined by Fowler-Nordheim techniques. The carbon-tungsten surface was produced by decomposing an ethylene covered emitter at 1000°K. The tip was then cooled to 50°K and redosed.

Figure 50. The decomposition of ethylene on a carbon-tungsten surface. The carbon-tungsten surface was produced by decomposing an ethylene covered emitter at 1000°K. The tip was cooled to 50°K and redosed. The tip was then flashed to the temperature indicated for 20 seconds.

(a) carbon-tungsten surface. (b) 100°K
(c) 150°K (d) 200°K
(e) 250°K (f) 300°K

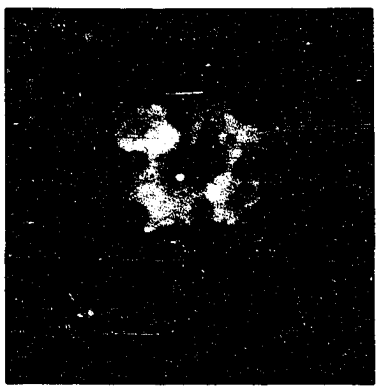

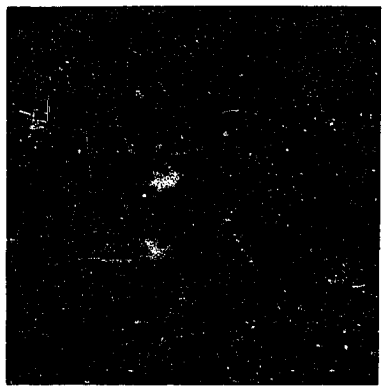

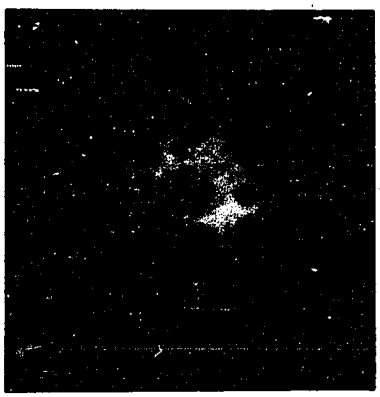

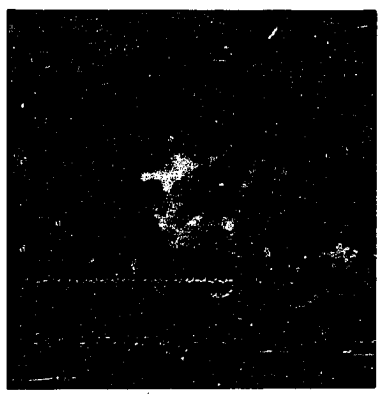

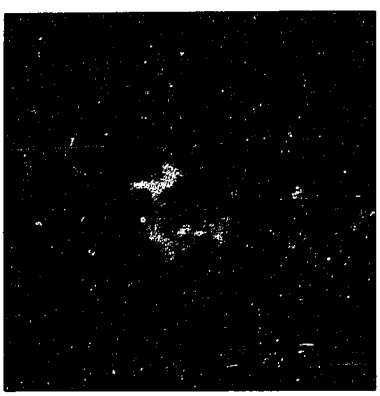

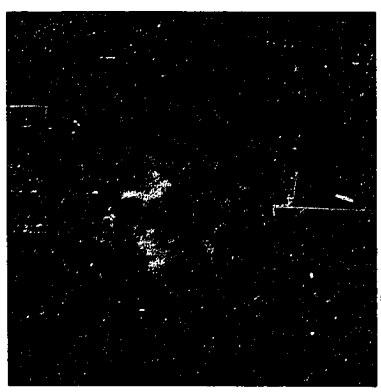

Figure 51. The emitter of Figure 50 was heated to the indicated temperature.

(a) 600°K (b) 700°K
(c) 800°K

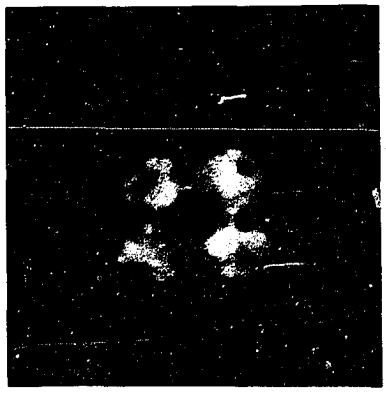

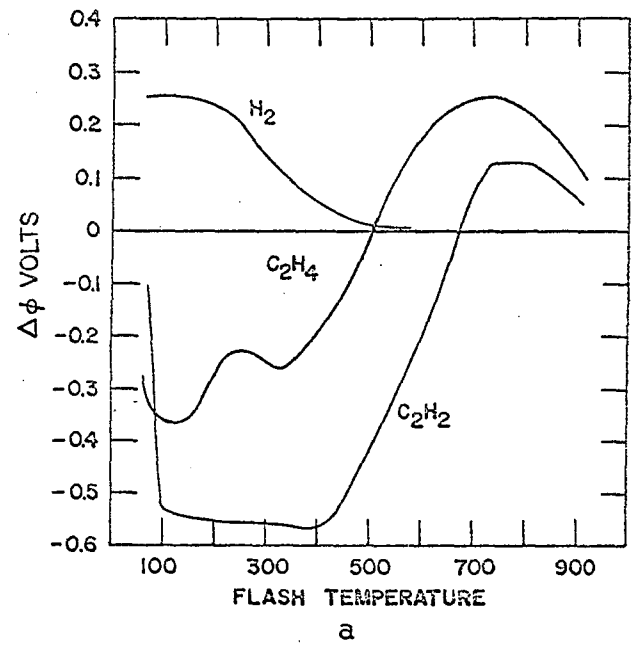

a

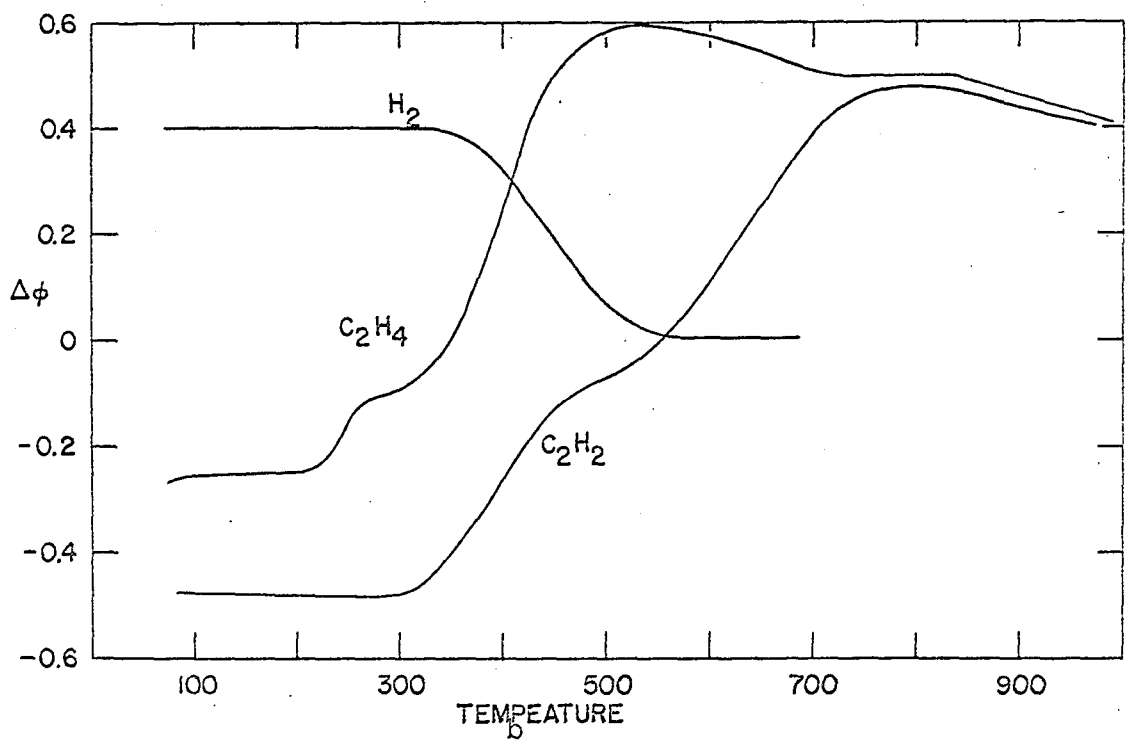

b

Figure 52. Work function versus temperature plots for the surface reactions of hydrogen, acetylene, and ethylene on (a) iridium and (b) tungsten.

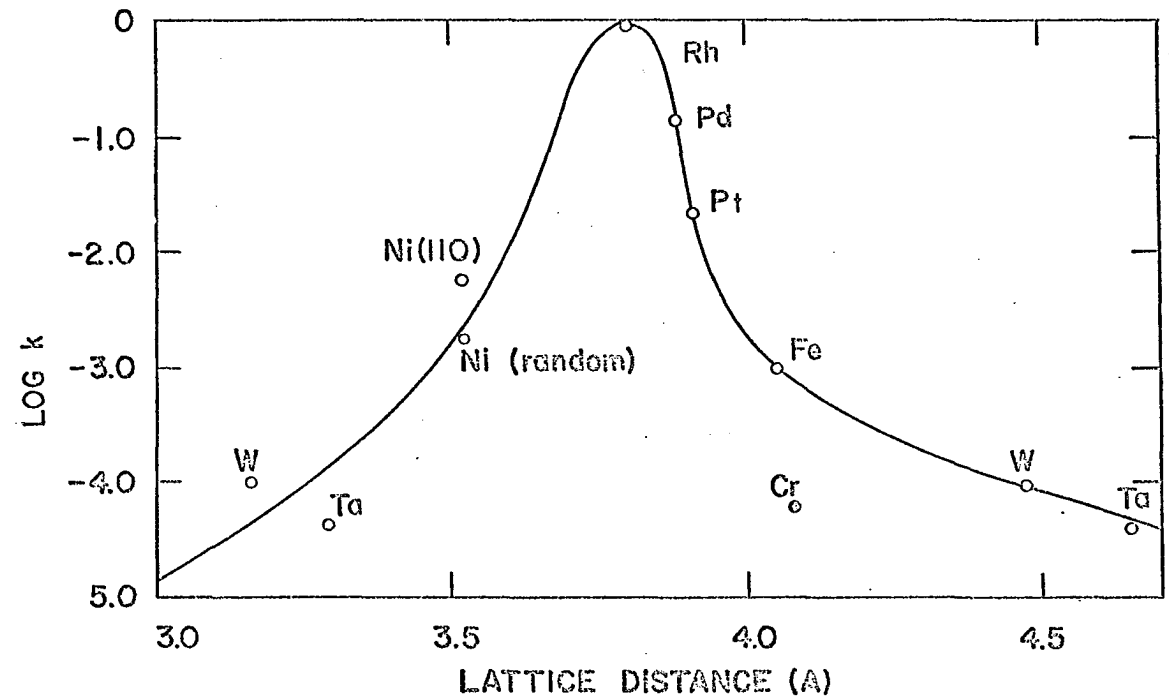

Figure 53. Variation in rate constant, k, with lattice spacings available on various metals for the hydrogenation reactions of ethylene.

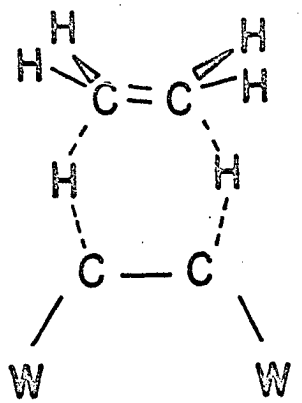

a

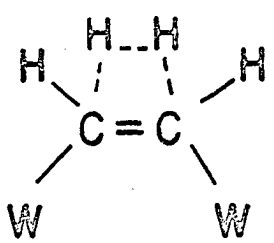

b

Figure 54. (a), Side view of the activated complex for the ethylene hydrogenation reaction. The hydrogen atoms in a plane parallel to the tungsten surface are omitted for clarity. (b), Side view of the activated complex for the formation of surface ethylenic species from acetylenic species and gaseous hydrogen.

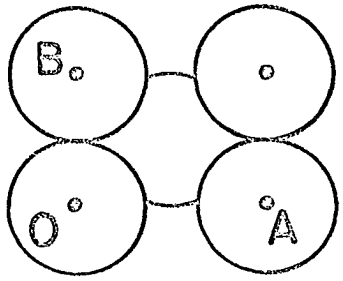

O-A 3.50 Å

O-B 2.47 Å

Figure 55. Diagram of the 110 plane of nickel, a face-centered cubic metal.

Table 1. Density of sites available on various crystallographic planes

Plane	Number of sites per unit surface cell area (Å^{-2})		
	2.74Å	3.16Å	4.47Å
110	0	.2	.1
110	.23	.23	0
111	.05	0	.1
112	.163	.081	.163

Table 2. Optimum and available metal-metal spacings for the chemisorption of acetylene and ethylene

Metal	Optimum site for C_2H_2	Optimum site for C_2H_2	Available site spacings
Nickel	3.33Å	2.87Å	2.47Å, 3.50Å
Tungsten	3.39Å	2.94Å	2.74Å, 3.16Å, 4.47Å

BIBLIOGRAPHY

1. Selwood, P. W., Adsorption and Collective Paramagnetism, New York, New York, Academic Press (1962).

2. Bond, G. C. and Wells, P. G., Advances in Catalysis, 15: 91 (1964).

3. Arthur, J. R., A Study of Surface Reactions by Field Emission Microscopy, unpublished Ph.D. thesis, Ames, Iowa, Library Iowa State University of Science and Technology (1961).

4. Arthur, J. R. and Hansen, R. S., Journal of Chemical Physics, 36: 2062 (1962).

5. Arthur, J. R. and Hansen, R. S., Annals of the New York Academy of Science, 101: 756 (1963).

6. Azuma, K., Journal of the Research Institute for Catalysis, Hokkaido University, Sapparo, Japan, 8: 267 (1960).

7. Beeck, O., Discussions of the Faraday Society, 8: 118 (1960).

8. Trapnell, B. M. W., Transactions of the Faraday Society, 48: 160 (1952).

9. Beeck, O., Review of Modern Physics, 17: 61 (1945).

10. Müller, E. W., Zeitschrift für Physik 106: 541 (1937).

11. Good, R. H. and Müller, E. W., Handbuch der Physik, 21: 176 (1956).

12. Dyke, W. P. and Dolan, W. W., Advances in Electronics and Electron Physics, 8: 89 (1956).

13. Gomer, R., Field Emission and Field Ionization, Cambridge, Massachusetts, Harvard University Press (1961).

14. Gomer, R. and Schmidt, L., Journal of Chemical Physics, 42: 3573 (1965).

15. Ehrlich, G., Advances in Catalysis, 14: 225 (1963).

16. Page, L. and Adams, M. I., Principles of Electricity, 3rd ed., New York, New York, D. Van Nostrand, Inc. (1958).

17. Gomer, R., Wortman, R. and Lundy, R., Journal of Chemical Physics, 26: 1147 (1957).

18. Little, L. H., Sheppard, N. and Yates, D. J. C., Proceedings of the Royal Society, London, A259: 242 (1960).

19. Twigg, G. H. and Rideal, E. K., Transactions of the Faraday Society, 36: 533 (1940).

20. Bond, G. C., Catalysis, 3: 109 (1955).

21. Bond, G. C., Catalysis by Metals, New York, New York, Academic Press Inc. (1962).

22. Eley, D. D., Catalysis, 3: 49 (1955).

23. Guy, R. G. and Shaw, B. L., Advances in Inorganic Chemistry and Radiochemistry, 4: 78 (1962).

24. deBoer, J. H., Advances in Catalysis, 8: 18 (1956).

25. Boudart, M., Journal of the American Chemical Society, 74: 3556 (1952).

26. Gomer, R., Journal of Chemical Physics, 21: 1869 (1953).

27. Trubey, D. K., U.S. Atomic Energy Commission Report ORNL-2750 (Oak Ridge National Laboratory, Oak Ridge, Tennessee) (1959).

28. Hasting, C., Approximations for Digital Computors, Princeton, New Jersey, Princeton University Press (1955).

29. Rye, R. B., Iowa State University of Science and Technology, Ames Laboratory Monthly Report 7/15 - 8/16 (1966).

30. Müller, E. W., Physical Methods of Chemical Analysis, Volume 3, New York, New York, Academic Press, Inc. (1956).

31. Klein, R., Journal of Chemical Physics, 22: 1406 (1954).

32. Mimeault, V. J., Flash Desorption and Isotopic Mixing of Simple Diatomic Gases on Tungsten, Iridium and Rhodium, unpublished Ph.D. thesis, Ames, Iowa, Library, Iowa State University of Science and Technology (1966).

33. Hansen, R. S., Mimeault, V. J., Arthur, J. R., and Rye, R. R., Journal of Physical Chemistry, 70: 2787 (1966).

34. Roberts, R. W., Journal of Physical Chemistry, 67: 2035 (1963).

35. Turkevich, J., Schissler, D. O., and Irsa, A. P., Journal of Physical and Colloid Chemistry, 55: 1078 (1951).

ACKNOWLEDGMENTS

The author is deeply indebted to Professor Robert S. Hansen for his enthusiastic, imaginative, and invariably correct councel.

The author thanks Robert Frost who wrote the computer programs used in this research.

To his wife, Mary, and his two children, Susan and Glen, a special thank you is due for their understanding and encouragement.